PHYSIK–DEPARTMENT

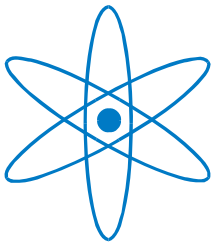

Electrochemical Characterization of Direct Alcohol Fuel Cells using in-situ Differential Electrochemical Mass Spectrometry

Dissertation

von

M. Sc. (Integ) Vineet Rao

TECHNISCHE UNIVERSITÄT

MÜNCHEN

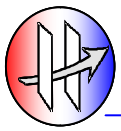

Technische Universität München
Fakultät für Physik
Lehrstuhl für Grenzflächen und Energieumwandlung E19

Electrochemical Characterization of Direct Alcohol Fuel Cells using in-situ Differential Electrochemical Mass Spectrometry

Vineet Rao

Vollständiger Abdruck der von der Fakultät für Physik der Technischen Universität München zur Erlangung des akademischen Grades eines

Doktors der Naturwissenschaften (Dr. rer. nat.)

genehmigten Dissertation.

Vorsitzender: Univ.-Prof. Dr. J. L. van Hemmen

Prüfer der Dissertation:

1. Univ.-Prof. Dr. U. Stimming
2. Univ.-Prof. Dr. J. Barth

Die Dissertation wurde am 15.02.2008 bei der Technischen Universität München eingereicht und durch die Fakultät für Physik am 09.06.2008 angenommen.

Table of contents

Abstract

This study relates to characterization of anode catalysts and anode catalyst layer related issue pertaining to direct alcohol fuel cells. For the case of carbon supported catalysts being used in the anode of direct methanol fuel cell, a saturation behavior for current density is observed at higher catalyst layer thicknesses. A simple catalyst layer model is presented in this work which explains this saturation behavior. The calculations with the presented catalyst layer model indicate that the proton conductivity in the catalyst layer is mostly responsible for the saturation behavior in high thickness and high current regimes. In further experiments PtRu alloy catalysts were prepared and special type of carbons namely sibunit carbons with varying porosity were used as carbon support for metal dispersion. In the membrane electrode assembly form, catalysts with low porosity carbon support were found to be nearly a factor of 3 better in terms of mass activity than Vulcan supported catalyst. Catalyst utilization factor was also found to be almost a factor of 2 higher for low porosity carbons in comparison to standard Vulcan supported catalyst. A possible reason for better results with low porosity carbon support based catalyst is proposed to be a better interaction between the micelle of nafion ionomer, which are normally >40nm in size, with, relatively wider pores of low porosity carbon support, where metal catalyst nanoparticles lie. Faster internal diffusion of reactants and products in wider pores further contribute to better activity.

In-situ fuel cell differential electrochemical mass spectrometry technique was used to investigate the influence of different fuel cell operational parameters on the completeness of the ethanol oxidation reaction (EOR) for acidic and alkaline membrane electrode assemblies (MEA). The CO_2 current efficiency (CCE) for EOR increases with increasing temperature and decreases with increasing ethanol concentration. The CCE increases strongly with increase in electrochemical active area (ECA) of the catalyst layer. The residence time of reactants and intermediate products and electrochemical active area seems to be the determining factors behind the final product distribution for EOR. But still the intrinsic nature of the catalyst remains very important as PtRu catalyst exhibits very low CCE in comparison to Pt and PtSn catalysts. On the other side, the alkaline MEA with Pt as catalyst shows very high CCE for EOR in comparison acidic MEA under similar conditions of temperature, concentration and electrochemical active area in the catalyst layer. This preliminary result indicates that the mechanism of EOR in alkaline medium is quite different in comparison to acidic medium and thus needs further investigation.

Zusammenfassung

Diese Studie befasst sich mit der Charakterisierung von Anodenkatalysatoren und verschiedenen Themen zu Anodenkatalysatorschichten in Direkt-Alkohol-Brennstoffzellen. Falls geträgerte Katalysatoren in der Anode von Direktmethanol Brennstoffzellen verwendet werden, wird ein Sättigungsverhalten für die Stromdichte an den dickeren Katalysatorschichten beobachtet. In dieser Arbeit wird ein einfaches Katalysatorschichtmodell vorgestellt, die dieses Sättigungsverhalten erklären kann. Die Berechnungen mit dem vorgestellten Katalysatorschichtmodell zeigen, dass die Protonleitfähigkeit in der Katalysatorschicht für das Sättigungsverhalten bei dicken Katalysatorschichten und hohen Stromdichten größtenteils verantwortlich ist. In weiterführenden Versuchen wurden PtRu Legierungskatalysatoren hergestellt und eine spezielle Art des Kohlenstoffs namens Sibunit mit unterschiedlicher Porosität als Trägermaterial benutzt. Als Anwendung der Anodenkatalysatoren in Form der Membran-Elektroden-Einheiten konnte festgestellt werden, dass Katalysatoren mit niedriger Porosität des Kohlenstoffträgermaterials, eine um einen Faktor 3 bessere Massenaktivität aufweisen, als Vulkan geträgerte Katalysatoren. Auch der Katalysatornutzungsgrad ist für Katalysatoren mit niedriger Porosität des Kohlenstoffträgermaterials um einen Faktor 2 besser als Vulkan geträgerte Katalysatoren. Als ein möglicher Grund für die besseren Ergebnisse von Katalysatoren mit niedrigerer Porosität des Kohlenstoffträgermaterials wird vorgeschlagen, dass eine bessere Interaktion zwischen den Mizellen des Nafion Ionomers, die normalerweise einen Durchmesser von mehr als 40nm haben, und den relativ großen Poren des Trägermaterials mit niedriger Porosität, in denen die Edelmetall Nanoteilchen sitzen, zu einer höheren Aktivität führt. Schnellere interne Diffusion der Reaktionsprodukte und -edukte in den größeren Poren tragen zu einer weiteren Erhöhung der Aktivität bei.

Um den Einfluss der unterschiedlichen Betriebsparameter einer Brennstoffzelle auf den Reaktionsmechanismus der Ethanoloxidation Reaktion (EOR) für sauere und alkalische Membran-Elektroden-Einheiten (MEE) zu untersuchen, wurde eine In-situ-Technik der differentiellen elektrochemischen Massenspektrometrie verwendet. Die Faradaysche Stromeffizienz der Konvertierung von Ethanol zu CO_2 (CSE) für die EOR, erhöht sich bei Zunahme der Temperatur und verringert sich bei Zunahme der Ethanolkonzentration. Die CSE erhöht sich stark mit Zunahme des elektrochemisch aktiven Oberfläche der Katalysatorschicht. Die Aufenthaltszeit der Reaktionsedukte und der Zwischenprodukte an der elektrochemischen aktiven Oberfläche scheint der bestimmende Faktor der letztendlichen Produktverteilung der

EOR zu sein. Aber auch die intrinsische Natur des Katalysators bleibt ein sehr wichtiger Faktor, da PtRu Katalysatoren im Vergleich zu Pt und PtSn Katalysatoren eine sehr niedrige CSE aufweisen. Andererseits zeigen alkalische MEE mit Pt als Katalysator im Vergleich zu saueren MEE, unter ähnlichen Bedingungen von Temperatur, Konzentration und elektrochemisch aktiven Oberfläche in der Katalysatorschicht, eine sehr hohe CSE für die EOR. Dieses vorläufige Ergebnis zeigt, dass der Reaktionsmechanismus der EOR im alkalischen Medium im Vergleich zum sauren Medium unterschiedlich ist und folglich weitere Untersuchungen benötigt werden.

1. Introduction

1.1 Direct methanol fuel cell

Fuel cells are attractive electrical power sources due to the fact that electrical energy can be produced as long as reactants are supplied to the electrodes (i.e. air or oxygen to cathode and hydrogen or methanol to the anode).This feature makes fuel cells complementary to batteries, as later have to be recharged frequently. In comparison to internal combustion engine fuel cells offers better energy efficiency and environmental compatibility. Thus a considerable need for advanced fuel cells will arise in foreseeable future. Two of the most advanced low temperature fuel cells are the proton exchange membrane fuel cell (PEMFC) and the direct methanol fuel cell (DMFC). Direct methanol fuel cells (DMFCs) using polymer electrolyte membranes are presently being considered candidate power sources for portable power and electric vehicle applications. There have been successful commercialization efforts for DMFCs, especially from companies like Smart Fuel Cells, Samsung, and Toshiba, which have already brought them into the market for portables. Large-scale commercialization potential of DMFCs is obstructed by much higher costs of the DMFC based power supplies, in comparison to batteries. High costs of DMFCs come from expensive Nafion® membranes on the one hand, and high noble metal loadings, necessary to sustain reasonable power densities, on the other hand [1, 2]. The latter are necessitated by sluggish anode and cathode kinetics, which limit the DMFC performance [1, 3]. These issues will be discussed in more detail in the following section. The DMFC directly consumes liquid fuel (methanol), while the PEMFC is fuelled by hydrogen. Operating a fuel cell with liquid fuel is considered to be essential for portable applications because of high energy density of liquid methanol and transport applications for compatibility with the existing petroleum distribution network. The DMFC also has system-related advantages over the PEMFC, making it of interest to fuel cell developers. For instance, the DMFC has no need for a fuel processor (or reformer) to convert a liquid hydrocarbon fuel (gasoline) into a consumable source of hydrogen. This considerably reduces the complexity and cost of the system. The DMFC system does not require the complex humidification and heat management hardware modules used in the PEMFC system: the dilute methanol-water mixtures circulating around the DMFC provide the necessary humidification and heat management. If it can meet the performance required of a commercially viable device, the DMFC system will be potentially more cost effective than the PEMFC. Performance has been a major problem for the DMFC: it typically produces only

one third of the PEMFC's power density. Hence, the DMFC community needs to make great efforts to bring the performance closer to that of the PEMFC, and particularly to extend the maximum operating temperature. The majority of the work has involved developing materials, such as new anode and cathode electrocatalysts and new proton conducting polymers, to improve the efficiency of the membrane electrode assemblies (MEAs) used in the DMFC stack. However, interest in producing low temperature (< 60ºC) ambient-pressure portable DMFC systems has increased recently. This is because the power densities now accessible by state-of-the-art MEAs may be enough for these systems to become competitive with leading secondary battery technologies. This area could thus become a near-term market opportunity for the DMFC, with transport uses being a longer-term goal, if further performance gains can be achieved.

1.1.1 PEMFCs and DMFCs: A comparison

The PEMFC and DMFC have much in common, in particular their MEAs [4]. In fact, possibility of direct use of methanol with out any reformation to hydrogen, helped in efforts toward conception and realization of DMFC. The MEA of a DMFC usually consists of five layers, which include gas, and liquid diffusion layers, and electrocatalyst layers with a polymeric proton conducting acidic membrane in between [5]. The proton conducting membrane acts as an electronic insulator between the electrodes, but allows protons to migrate efficiently from the anode to the cathode. The membrane also functions as a physical barrier to prevent mixing of the reactants. In addition, a soluble form of the membrane material is used to impregnate the electrocatalyst layers to provide proton conductivity within the catalyst layer. While the structures of the MEAs used in the PEMFC and DMFC are similar, the performance of each is very different. A comparison of the performance of the two fuel cells and the factors which limit their efficiencies is shown in Figure 1.1.

The DMFC has a maximum thermodynamic voltage of 1.21 V at 25ºC, defined by its anode and cathode half-cell reactions:

Anode reaction: $CH_3OH + H_2O = CO_2 + 6H^+ + 6e^-$

$U^0_a = 0.02$ V

Cathode reaction: $3/2O_2 + 6H^+ + 6e^- = 3H_2O$

$U^0_c = 1.23$ V

Cell reaction: $CH_3OH + H_2O + 3/2O_2 = CO_2 + 3H_2O$

$\Delta U^0_{cell} = 1.21$ V

In comparison, the PEMFC has a maximum thermodynamic voltage of 1.23 V at 25ºC. In practice, the cell voltage in both fuel cells is much less than this, see Figure 1.1. For example, at a current density of 500 mA cm^{-2}, the cell voltage is typically around 0.75 V for the PEMFC [4] and 0.4 V for the DMFC [6]. Therefore, the power density and efficiency are considerably higher in the PEMFC (61 per cent) than in the DMFC (34 per cent).

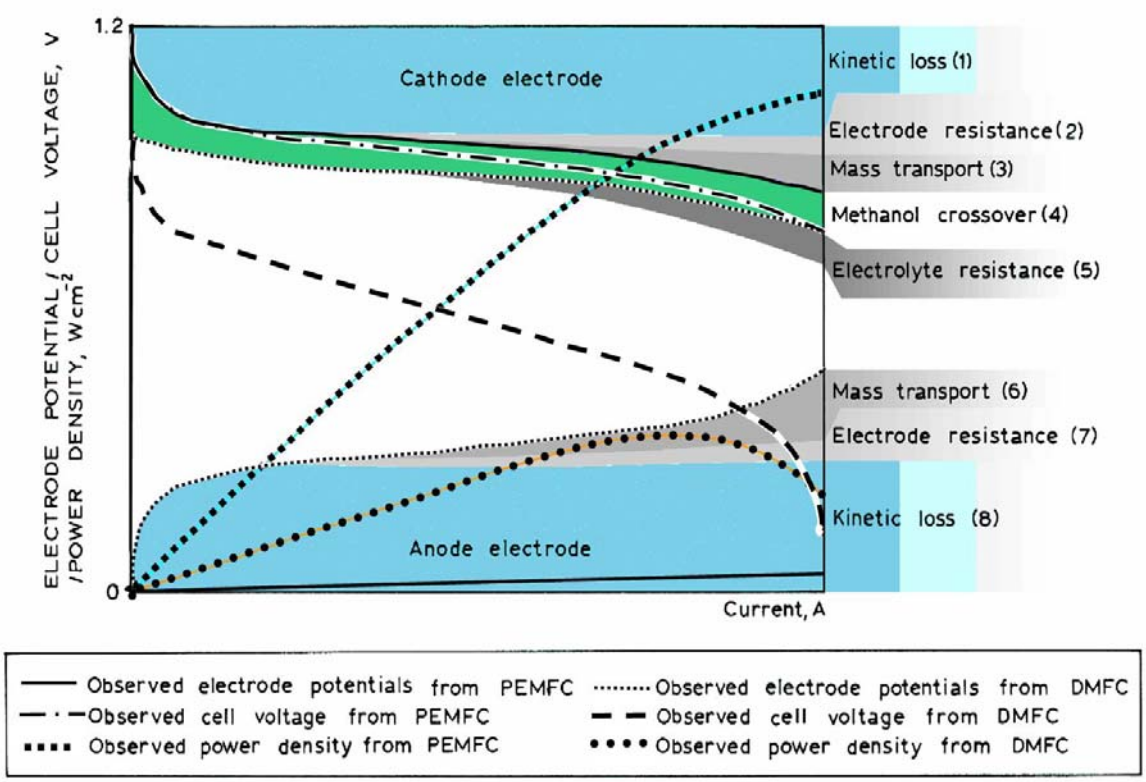

Figure 1.1. The performance losses seen in a typical DMFC MEA operating with dilute methanol and air at 80ºC, compared to those in a PEMFC. The PEMFC is operating with pure hydrogen. A list of factors affecting the efficiencies of both fuel cells is on the right side. Figure taken from ref: [4] .

1.1.2 Kinetic limitations

Both types of fuel cell are limited by the poor electrochemical activity of their cathodes. This reduces the cell voltage of both by up to 0.4 V at 500 mA cm^{-2}. However, unlike the PEMFC (when operated with pure hydrogen), the DMFC *anode* is also limited by poor electrochemical activity (*kinetic loss* (8) in Figure 1.1). This can account for a further loss in cell voltage of more than 0.3 V at 500 mA cm^{-2} (at 90ºC). To increase both the anode and

cathode activities in the DMFC, the electrocatalysts employed are usually unsupported (with high Pt loadings of typically 5 to 10 mg Pt cm^{-2} for each electrode) rather than the carbon-supported electrocatalysts used in the PEMFC. This Pt loading is too high for commercial exploitation of the DMFC (but it does of course dramatically increase the power densities attainable by the MEA). By contrast, typical PEMFC electrodes are carbon-supported electrocatalysts, loaded at 0.2 to 0.5 mg Pt cm^{-2}.

1.1.3 Methanol and water crossover

Another critical effect, which reduces the efficiency of the DMFC, is fuel crossover (*methanol crossover* (4) in Figure 1.1). Methanol and water readily diffuse through all the commercially available polymeric membrane electrolytes (such as Nafion), and significant quantities of methanol and particularly water pass from the anode to the cathode. This reduces the cathode efficiency in two ways.

First, any methanol that comes into contact with the cathode electrocatalyst will reduce the efficiency of the oxygen reduction reaction by a competing electrochemical process – known as the mixed potential effect. Second, the cathode structure becomes waterlogged or flooded, and is no longer an efficient structure for gas diffusion (*mass transport* loss, (3) in Figure 1.1). Both these effects can reduce the cell voltage by a further 0.2 to 0.3 V, particularly when practical air flows are used.

In practice, the effects of methanol crossover can be reduced to a large extent by careful design of the MEA structure or by the application of novel membrane materials [7] or cathode electrocatalyst materials [8], [9]. The use of thick membrane materials, such as Nafion 117 (~ 180 μm), in preference to those used in the PEMFC, such as Nafion 112 (50 μm), is often a sensible choice. Using a thick membrane does increase the cell resistance (*electrolyte resistance* (5) in Figure 1.1), but it is usually easily outweighed by an improved performance as a result of reduced crossover.

A further consequence of the high methanol crossover rates in commercially available materials is that to reduce it, the DMFC anode must be supplied with dilute methanol fuel, typically 0.5 to 1.0 molar concentrations. This presents problems for system design because, in addition to the methanol fuel, large quantities of water must be stored, adding to the size and complexity of the system. It is particularly awkward for applications where space is

limited, such as portable devices. As the methanol concentrations used in the DMFC are low, the anode structure has to be designed to allow both efficient diffusion of the liquid fuel into the electrocatalyst layer and effective removal of the product carbon dioxide (CO_2). Correct design of the anode electrode structure is very important for limiting anode *mass transport* losses ((6) in Figure 1.1).

1.1.4 Anode electrocatalyst limitations

For DMFC one of the major limitations is performance of the anode electrocatalyst layer. Although the electrooxidation of methanol is thermodynamically driven (by the negative Gibbs free energy change, in the fuel cell), in practice, the rate of methanol electrooxidation is severely limited by poor reaction kinetics. To increase the efficiency of the anode reaction, it is necessary to understand the reaction mechanism. Indeed, there has been lot of research aimed at identifying the nature and rate limiting steps of this reaction[10].

Only Pt-based electrocatalysts display the necessary reactivity and stability in the acidic environment of the DMFC. Spectroscopic studies on polycrystalline Pt have shown that methanol is electrosorbed in a complex process analogous to dehydrogenation. Sequential stripping of protons and electrons is believed to take place, leading to the formation of carbon-containing intermediates, such as linearly bonded $–CO_{ads}$ and $–CHO_{ads}$ [11], [12].

Although the vast majority of these studies have been carried out on bulk polycrystalline or single crystal metallic Pt surfaces, it is possible to study the methanol electrosorption process on finely divided electrocatalysts in a single cell. Methanol electrosorption appears to occur spontaneously when the anode and cathode of an MEA are connected externally by an electrical circuit. Hence, when methanol comes into contact with the electrocatalyst, an electric current flows between the two electrodes. This occurs for only a brief period of time until the electrocatalyst becomes poisoned with surface-bound intermediates, such as $–CO_{ads}$. Rest of the details of the mechanism of methanol oxidation will be discussed in the next section. A deep understanding of the various issues related to the anode catalyst layer like diffusional pore structure, internal resistance of the catalyst layer etc. is very important. These properties of the anode electrocatalyst layer play a very important part in the overall activity of the catalyst in real fuel cell environment. Many other morphological and physiochemical properties of the anode electrocatalyst layer will be discussed later in a separate section.

1.2 Electrocatalysis of methanol oxidation

1.2.1 The methanol system

The thermodynamic potential for methanol oxidation to CO_2, lies very close to the equilibrium potential of hydrogen:

$$CH_3OH + H_2O \longrightarrow CO_2 + 6H^+ + 6e^- \qquad U^0 = 0.02 \text{ V}$$

However, compared with hydrogen oxidation, this reaction is by several orders of magnitude slower. As early suggested by Breiter[13], the total oxidation process consists of a pattern of parallel reactions which can, in principle, be formulated as follows:

$$CH_3OH \longrightarrow \text{adsorbed intermediates} \begin{cases} \nearrow CO_{ad} \longrightarrow CO_2 \\ \searrow HCHO, HCOOH \longrightarrow CO_2 \end{cases}$$

Both of these pathways require a catalyst, which should be able to
(a) Dissociate the C-H bond and

(b) Facilitate the reaction of the resulting residue with some O-containing species to form CO_2 (or HCOOH).

On a pure Pt electrode, which is known to be the best catalyst for breaking the C-H bond, complete oxidation takes place via two processes occurring in separate potential regions:

1) The first process, involving adsorption of methanol molecules, requires several neighboring places at the surface. Since methanol is not able to displace adsorbed H atoms, adsorption can only begin at potentials where enough Pt sites become free from H, i.e. near 0.2 V versus RHE for a polycrystalline Pt electrode.

2) The second process requires dissociation of water, which is the oxygen donor of the reaction. On pure Pt electrode, a strong interaction of water with the catalyst surface is only possible at potentials above 0.4-0.45 V versus RHE.

Thus, on a pure Pt catalyst methanol oxidation to CO_2 cannot begin below, say 0.45 V. However, the adsorbate layer does not exhibit a good reactivity below approximately 0.7 V, i.e. a high rate of oxidation at pure Pt occurs at potentials without technological interest.

1.2.2 Methanol adsorption

It was suggested that methanol adsorption takes place in several steps, forming different species due to dissociation of the molecule:

$$CH_3OH \rightarrow x\text{-}CH_2OH + H^+ + e^- \rightarrow x_2\text{-}CHOH + H^+ + e^-$$
$$\rightarrow x_3\text{-}COH + H^+ + e^- \rightarrow x\text{-}CO + H^+ + e^-$$

where x stands for a Pt site [14]. It was suggested that formaldehyde and formic acid could be formed from the intermediates CH_2OH and CHOH, respectively .If a cyclic voltammogram is started after contacting a polycrystalline Pt electrode with a methanol containing solution at a potential of 0.05 V or less, methanol adsorption can be observed as soon as hydrogen coverage decreases to a certain extent. The dissociation process gives rise to a current peak in the H-region (Figure 1.2), which can be observed only during the first potential scan, i.e. when the surface is free from organic residues. The experiment in this figure was performed using the DEMS technique[15] [16]. Briefly, in this technique the electrode is a porous Pt layer on a PTFE membrane, lying on a porous plate at the entrance of a mass spectrometer. This setup allows the entrance of any volatile product in the MS in fractions of a second after being produced. During the experiment in Figure 1.2, recording of mass (m/e = 44) corresponding to CO_2 is given. The recording of mass signals did not show any volatile product from methanol oxidation. Thus the current peak can only be due to faradaic processes occurring during methanol adsorption.

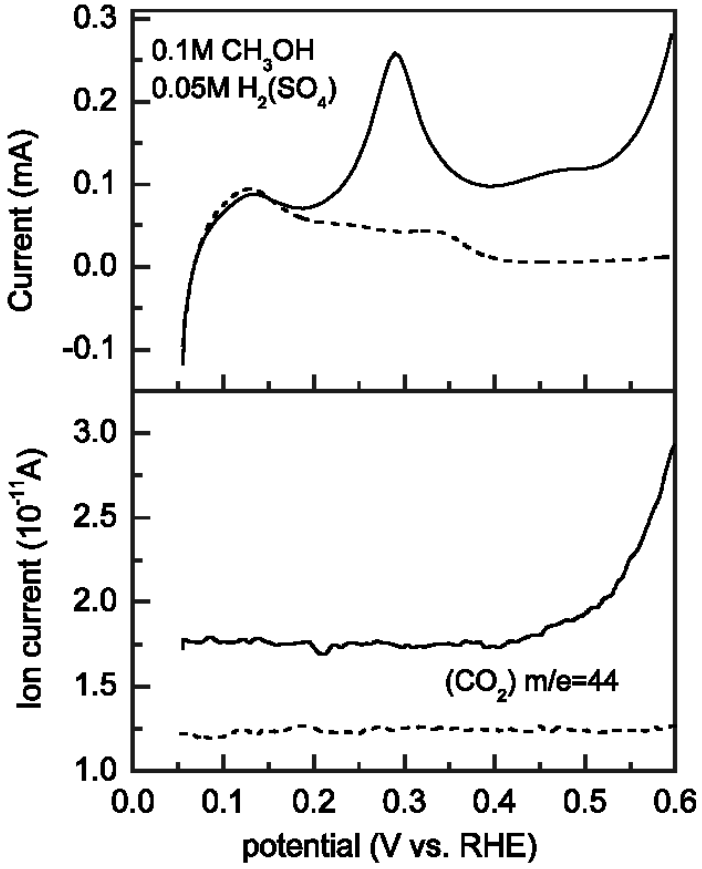

Figure 1.2. First potential scan for a porous polycrystalline Pt electrode in 0.1 M CH_3OH/0.05 M H_2SO_4 solution (upper part) and simultaneously recording of mass intensity for CO_2 production (lower part); 10 mV s^{-1}. Dashed lines: current and MS signals in supporting electrolyte. Figure taken from reference [15].

1.2.3 Methanol oxidation products

The oxidation products of CH_3OH are well known since early 1950. Long-term electrolysis at potentials between 0.5 and 0.6 V versus RHE ,was used and CO_2, HCHO, HCOOH and $HCOOCH_3$ were found [17, 18]. The latter product, methyl formate, originates in a reaction:

$$HCOOH + CH_3OH \longrightarrow HCOOCH_3 + H_2O$$

The yields of oxidation products depend on methanol concentration, temperature, electrode roughness and time of electrolysis [19, 20]. The study of the products of methanol oxidation during a potential scan was the first goal of on-line mass spectrometry, DEMS [21]. In Figure 1.3, the potentiodynamic formation of CO_2 and methyl formate on a Pt electrode was

followed during the potential scan by recording the corresponding ion currents in the MS: (m/e = 44) and (m/e = 60), respectively. No mass signals for HCHO were observed, but a weak ion current for methylal ($CH_2(OCH_3)_2$), indicated its formation via reaction of HCHO with CH_3OH [7]. However, there must be some problem with the volatility of formaldehyde or its hydration product in aqueous solution (gemdiol, $CH_2(OH)_2$), which makes somehow difficult its direct detection using the DEMS technique [22]. These difficulties extend to other modern analytical methods like in situ FTIR as pointed out by Korzeniewski and Childers[23].

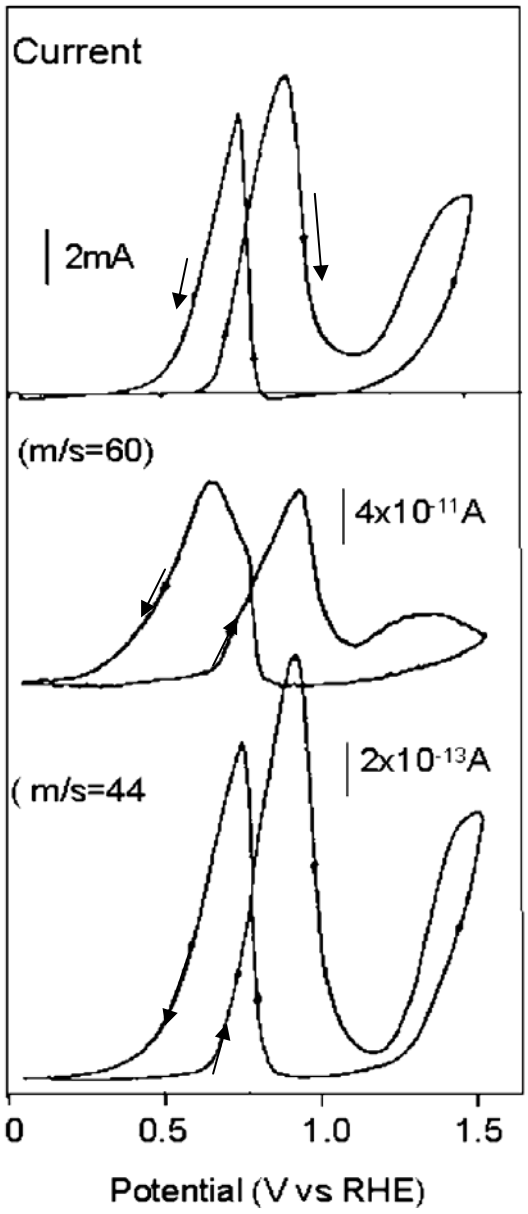

Figure 1.3. DEMS experiment: current and mass signals (ion current) for volatile products during methanol oxidation at porous polycrystalline Pt, surface roughness: ca. 50; 0.1M CH_3OH 1M $HClO_4$; 20 mV s^{-1}. Figure taken from reference [15].

This could be the reason why formaldehyde remained almost disregarded in the methanol fuel cell literature. Korzeniewski and Childers determined formaldehyde yields fluorometrically after applying different constant potentials on a smooth polycrystalline Pt electrode, during 5 min in a micro cell. They report for formaldehyde a yield of 38% under following conditions: 0.25 V versus Ag/AgCl (ca. 0.48 V vs. RHE), 15 mM CH_3OH 0.1 M $HClO_4$. The yield decays at higher potentials [23]. On porous Pt electrodes, Wang et al. found at 0.65 V versus RHE 50% of HCHO, 34% of HCOOH and only 16% of CO_2. It is worth noting that Ota et al. also found relatively high yields of HCHO on platinized Pt electrodes at 0.6 V versus RHE [20].

1.3 Introduction to DEMS

1.3.1 Differential Electrochemical Mass Spectrometry (DEMS) system

Online observation of mass signals from the volatile reaction products offers useful additional information on the reaction taking place at an electrochemical interface. Mass spectroscopy is especially useful for studying fuel cells reactions in simple laboratory cells and also fuel cell systems, at ambient conditions and also at elevated temperature and pressure.

For study of many electrochemical reactions cyclic voltammetry is not enough [24]. More experimental information than just current as a functional of potential, would be very helpful for an analysis. One such additional information is the simultaneous recording of mass signals of volatile reaction intermediates and products. For mass signals also cyclic voltammograms can be resolved even up to 100mV/s[25-27] . Thus, a continuous control of fuel cell reactions as a function of time is possible.

The basic idea of online mass spectroscopy was the suggestion from Bruckenstein [28, 29] to use a porous Teflon membrane as window between electrochemical cell and mass spectrometer. The working electrode of the Bruckenstein cell is porous platinum layer, attached to the membrane on the electrolyte side. The membrane window to the MS was mechanically stabilized by a glass frit. After the connection of the cell to the MS, a large part of the species produced or consumed at the interface is entering the MS through the pores of the membrane, a part of the species being ionized in the ion source of the MS. In the original Bruckenstein device, the mass intensity is showing the integrated intensity of the masses

entered through the window. This is due the fact, that the gas volume in the analysis chamber is not replaced during the recording time. In order to produce a mass signal cyclic voltammogram (MSCV), it is necessary to obtain differential signals as a function of time and herewith as a function of potential like in the current / potential CV. The sensitivity in the form of ion current per mA of electrochemical current must be high and in a linear relation, and as a second condition, the total gas volume has to be emptied in a time near 10^{-2} s or less. Therefore turbo molecular pumps are needed.

Online mass spectroscopy as described above obviously can be applied in all cyclic voltammogram studies, galvanostatic or potentiostatic experiments where ever volatile species are involved. Additional information can be derived by comparing CV and MSCV. MSCV is free of double layer charging and pseudo capacity effects. Only that part of the current by which the respective species is formed or consumed, can give a corresponding mass signal.

1.3.2 FC -DEMS systems with liquid and gas anode feeds

The combined FC –DEMS system were then designed to study the fuel cell reactions in real fuel cell conditions. For portable applications, since the preferable phase of operating Direct Methanol Fuel Cell is liquid, so it is important to study the methanol oxidation intermediates and products in same conditions. The dependence of product distribution on various parameters related to fuel cell operating conditions, MEA preparation, temperature, concentration of methanol, pressure, type of catalyst etc can be studied with the help of FC-DEMS setup, which can provide vital technological inputs for designing better fuel cell systems.

1.4 Characteristics of DMFC anode electrocatalyst

An electrode is quite complex in its structure. For a reaction to occur on the catalyst not only methanol and water need to be present, the catalyst has to be in electric contact with the gas backing layer and in ionic contact with the polymer electrolyte. In order to make better electrode, knowledge about what limits the performance of the electrode is of great importance. With this knowledge about the limitations of the electrode, the morphology can be modified in various ways, to utilize the catalyst as effectively as possible by varying

porosity and morphology of the carbon supports, thickness of catalyst layer and fractions of electron and ion conducting components. Knowledge about the limitations may also lead to new innovative solutions to overcome the limiting processes.

1.4.1 Catalyst morphology

This issue contains several different directions which, however, merge, as far as the objective is concerned: how to extract the best possible performance out of a given amount of noble metals incorporated in a particular catalyst? It can be broken down into catalyst preparation, pretreatment and characterization. Other topics, such as possible catalyst-support interactions and the choice of a suitable carbon support, are also involved. Generally, it is an agreed fact that catalysis by small particles is different from that at smooth electrodes [12, 30, 31]. Especially, Christensen et al. [12] express it very clearly by stating that extrapolation from bulk to particle electrodes is very dangerous. This, again, emphasizes our remarks above, that some rules for the application of single-crystal electrochemistry to technical electrodes have to be established before meaningful conclusions can be drawn.

Several routes of catalyst preparation have been attempted [32] [33-35]. Especially from research for the phosphoric acid fuel cell (PAFC) it is known that stable multi-metal catalysts can be manufactured [36]. It is generally agreed that the preparation has an important influence on catalyst performance. In these studies, the authors found an optimum route, by comparing different ways of catalyst preparation. Colloid systems were proposed as promising precursors for supported fuel cell catalysts consisting of ultra-fine metal particles showing a mean diameter of only 1.79 ± 0.5 nm [37]. Due to the ultra low particle diameter, such systems represent a challenge for comparative studies and their activity needs to be assessed relative to conventional systems in order to be able to judge the progress provided by this novel approach. Catalyst pretreatment (activation) is another factor having great influence on catalyst performance [38]. It was found that heating a PtRu catalyst in air leads to better results than that in hydrogen due to a surface enrichment of Pt in the presence of hydrogen. Thus, surface enrichment; depletion effects have to be taken into account, not only during the activation procedure, but also during the lifetime of the catalyst.

The choice of a suitable carbon support is a factor in addition to those mentioned above, which may affect the performance of supported catalysts. Interactions between the catalyst and the carbon support have been identified which modify the catalyst activity [39-41]. These

interactions are dependent on the nature of the functional groups of the carbon support. For instance, it was found that carbons with lower concentration of acid; base groups [39] and carbons with sulfur- or nitrogen- based functionalities [41] have an enhanced catalytic activity.

1.4.2 Particle size effects

For the development of methanol fuel cells[42-46], many investigations have been made on the catalytic activity of Pt–Ru alloy electrocatalysts which perform as active anodes for methanol and carbon monoxide-containing hydrogen. Among the various factors possibly affecting the catalytic activity of the Pt–Ru alloy catalysts for methanol oxidation, the dependence of the Pt–Ru particle size on the catalytic oxidation of methanol, *e.g*. the 'size effect', is an important factor for recognizing the fundamental catalytic properties of ultrafine alloy particles. The size effect of platinum particles of Pt/C catalysts for the oxidation of CO and methanol has been examined by some research groups[47-51]. Takasu et. al. [52] reported the same for well-homogenized Pt–Ru alloy particles . Ultrafine catalyst metal particles are often more active compared to larger ones probably due to their higher concentration of low-coordinated surface metal atoms. The alloy composition used was Pt50–Ru50, (Pt:Ru = 1:1 mol/mol), since this composition was the most active in the binary alloy catalyst systems.

The specific activity, i_{sp}/A m^{-2} (current density per real surface area), of Cl-free well-homogenized Pt–Ru particles at 25 and 60 °C in aqueous acidic solutions has been found to decrease with a decrease in the size of the Pt–Ru alloy particles, and the mass activity, i_{mass}/A g^{-1} (current density per mass of catalyst metal loaded), showed the same dependency when the size of the alloy particles was < *ca*. 3 nm in diameter. The mass activity shows a peak around 3nm.

1.4.3 Inherent mismatch between nafion micelle and carbon support particles

The catalyst layer has been investigated using scanning and transmission electron microscopy and XRD by Arico[53]. The understanding of the interaction between catalyst and nafion ionomer is important for designing new catalysts and for selecting appropriate carbon supports. This would help in discovering novel methods of dispersion of nafion ionomer into the catalyst layer to maximize the electrochemical reaction area, lateral ionic conductivity and minimization of the diffusion problems for the supply of reactants and removal of reaction

products. A TEM micrograph of a typical catalyst-nafion interface is shown in Figure 1.4.

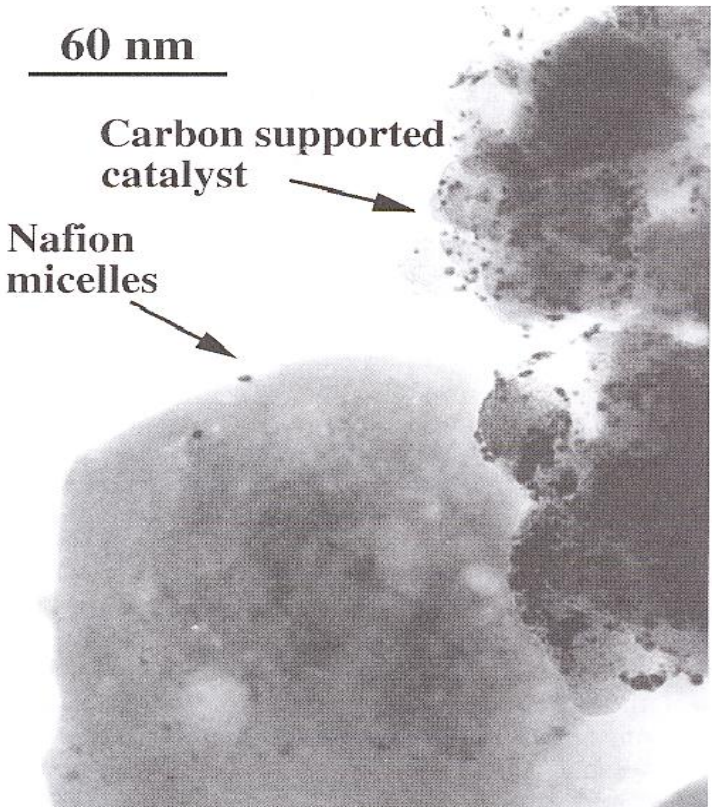

Figure 1.4. TEM micrograph of carbon supported catalyst- nafion micelle interface. Figure taken from reference [53].

A nafion micelle or agglomerate of about 200nm is clearly visible on left side, whereas metal particles of about 2nm size are observed on the edges of the carbon agglomerates. This appears to account for physical overlapping between nafion and catalyst particles with no chemical interaction. This can be explained on the basis of significant difference in size between a nafion micelle (about 200nm) and primary carbon particles (about 30 nm). Moreover the pores formed by carbon agglomerates are not accessible to big nafion micelle.

So on this basis two main problems are recognized: 1) No close interaction occurs between nafion and catalyst phase due to their different particle dimensions. 2) The absence of a significant interconnected network of nafion particles inside the catalyst layer suggests that some limitation for ionic transport could occur in composite electrodes. The first problem has also been pointed out by Uchida et. al.[54] for solid polymer electrolyte fuel cells. Accordingly catalyst preparation procedures addressed to locate metal particles on the outer

carbon surface have been shown to enhance the cell performance significantly.

1.4.4 Introduction to sibunit carbons as catalyst support

In DMFCs, methanol is electrooxidized at the anode to CO_2, resulting in an electric current. Electrocatalysts having higher activity for methanol oxidation are critically needed to achieve an enhanced DMFC performance. Since up to now only platinum is known to have the ability to activate and break C-H bonds in the temperature range of DMFCs (from 25 to 130°C), all presently available anode catalysts contain significant amounts of Pt [1, 3, 30, 32, 55, 56]. Because of the high costs and low availability of Pt, there have been considerable efforts to extract maximum performance from minimum amount of this noble metal. Introduction of the catalysts dispersed on electrically conducting and high surface area carbon materials [1, 3, 57, 58] was a significant step forward, which resulted in finer dispersion of the metal catalyst and thus higher electrochemically active surface area. Different carbons have been tested as catalyst supports for fuel cell applications. Carbons with high specific surface areas (like Ketjenblack) are beneficial in terms of providing high dispersion of the active component, other conditions being equal. On the other hand, utilization of high surface area carbons as supports for fuel cell electrocatalysts may result in ohmic and mass transport limitations. Hence, Vulcan carbons with specific surface areas around 250 m^2g^{-1} are often used as a reasonable compromise. However, to our knowledge, optimal properties of Vulcan carbons for either PEMFC (polymer electrolyte fuel cell), or DMFC applications have not been verified experimentally.

Many research groups have recently made efforts to unravel the influence of carbon support properties on the activity of fuel cell electrocatalysts. Uchida et. al. [54, 59] have found that metal nanoparticles residing in carbon pores below 40 nm in diameter, have no access to Nafion® ionomer and thus do not contribute to the electrochemical activity. This decreases the extent of catalyst utilization denoted as a ratio of the electrochemically accessible surface area of metal nanoparticles to their total surface area. In order to improve the extent of metal-ionomer interaction, Uchida et al. [54, 59] experimented with specific surface areas of acetylene black carbons. He reported on a decreased internal resistance of the catalyst layer and an improved PEMFC performance relative to conventional carbon supported catalysts, because of better Nafion®- catalyst contact. Electrocatalysts consisting of platinum particles supported on graphite nanofibers (GNF) were prepared by Bessel et al. [60], who reported a four-fold improvement of mass activities for methanol electrooxidation

in sulphuric acid electrolyte. Lukehart's group [61-63] prepared a PtRu/herringbone GNF nanocomposite using a single-source molecular precursor as a metal source, and performance of a DMFC with this nanocomposite as the anode catalyst was enhanced by 50% relative to that recorded for an unsupported PtRu anode catalyst. More recently nanotubes (single walled and multiple walled) [64-67], graphitic carbon nanofibres (GCNF), nanocoils, and many other proprietary carbons have been investigated to find an optimum carbon support for fuel cell applications [63]. Carbon nanocoils, as reported in Refs. [68-71], provide at least two times higher activity for methanol oxidation in comparison to Vulcan XC-72. The authors tentatively attributed the enhancement to higher crystallinity (and hence lower Ohmic resistance), higher surface area and appropriate porosity of these carbon materials. Takasu et al. studied the influence of specific surface area of carbon supports on the size and extent of alloying of metal catalyst particles [72].

Carbon materials affect many vital properties of supported metal catalysts, in particular: (i) metal particle size, morphology and size distribution; (ii) extent of alloying in bimetallic catalysts; (iii) stability of supported metal nanoparticles towards particle growth and agglomeration; (iv) electrocatalytic activity e.g. due to metal-support interactions; (v) degree of catalyst utilization; (vi) mass transport in the catalytic layer; (vii) electronic conductivity of the catalyst layer and thus its Ohmic resistance, etc. Hence, we believe that optimization of carbon support is of *crucial importance* for the development of PEMFCs and DMFCs. On the other hand, versatile influence of carbon supports on electrocatalytic properties and hence fuel cell performance, makes it difficult to understand its physical origin and puts a hurdle on catalyst optimization. Thus, one and the same property of carbon may be advantageous at the stage of catalyst preparation, but detrimental at the stage of fuel cell operation. For example, carbon materials with high specific surface area (which usually originates from high contribution of micro- and mesopores) allows better metal dispersion at the catalyst preparation step, but may lead to Ohmic and mass transport limitations during fuel cell operation. That's why, despite considerable efforts, it is still not completely clear which carbon properties are beneficial for fuel cell applications. In this study we introduce an approach to systematically investigate the effect of carbon support porosity and specific surface area on the PtRu anode performance by decoupling between the influence of support on (i) the catalyst preparation and hence metal dispersion, and (ii) its operation in a DMFC.

1.4.5 Investigating the effect of carbon support porosity on catalytic activity

In this work we explore a possibility to use carbons of Sibunit family as supports for preparing catalysts for low temperature fuel cells. These carbon materials are prepared through pyrolysis of natural gases on carbon black surfaces followed by activation to achieve desired values of the surface area and pore volume [73]. Pyrolysis leads to formation of dense graphite-like deposits, and in the course of the activation step, the carbon black component is removed first. Hence, the pore size distribution in the final Sibunit sample roughly reproduces the particle size distribution in the carbon black precursor. Thus, varying the type of the gas source, the template (carbon black), and the manner and duration of the activation, allows production of meso- or macroporous carbon materials with surface areas from 1-50 (non-activated) to 50-500 m^2g^{-1} (activated) and pore volume up to 1 cm^3g^{-1}. This gives a unique opportunity to vary the specific area of carbon supports, keeping their chemical nature essentially intact. Other advantages of carbons of the Sibunit family are: (i) purity, (ii) high electrical conductivity and (iii) uniform morphology of primary carbon globules (contrary to carbon blacks, in particular Vulcan [74]).

The idea introduced in this work is to widely vary the specific surface area of the carbon support (from a few meters per gram to a few hundreds meters per gram), keeping the size and structure of the active PtRu component possibly constant. Electrocatalytic activity of PtRu nanoparticles has been found to be strongly influenced by the metal dispersion. Takasu et al [52] have found that mass specific activity of PtRu nanoparticles in methanol oxidation (measured in H_2SO_4 electrolyte at 60°C) passes through a maximum at ca 3 nm and decreases markedly, as the particle size decreases. Keeping this in mind, in this work we aimed at keeping the size of PtRu particles close to 3 nm. However, the latter is hard to attain, if metal loading is kept constant, while specific surface area of carbon supports is varied in a wide range. Indeed, metal dispersion is known to decrease, if either (i) the specific surface area of a carbon support is reduced at a constant metal loading [72] or (ii) the amount of metal is raised at a constant support surface area [52, 75]. Hence, Guerin et al. [76] reported that the average particle size of commercial Johnson Matthey Pt catalysts supported on Vulcan XC-72R increased from ca. 1 nm to ca. 6.5 nm, when the metal loading was raised from 10% to 78%. CO stripping voltammograms presented by the authors suggest that significant part of nanoparticles in high loading catalysts is agglomerated. In this work, in order to keep the particle size around 3 nm, we varied the amount of metal (PtRu) per unit mass of a carbon support. Thus, for the low surface area carbon supports (Sib_P2677 with 22 m^2g^{-1} and Sib_19P with 70 m^2g^{-1}) metal percentage was set at 10%, while for high surface area carbon

supports (Sib_20P with 292 m^2g^{-1} and Sib_619P with 415 m^2g^{-1}), it was increased to 20%. The catalyst supported Sib_176K with 6 m^2g^{-1} specific surface area, contained only 1%PtRu. Thickness of the catalyst layer is another parameter, which plays an important role in the overall performance of a fuel cell. It affects ohmic resistance, current and potential distribution and mass transport in the electrocatalyst layer [77-79]. Thus, differences in the intrinsic catalytic activities of two DMFC anode catalysts incorporated in MEAs with significantly different thicknesses of the catalyst layer may be overshadowed by the influence of mass transport. Therefore, in order to make a meaningful comparison between different catalysts, we kept the anode catalyst layer thickness constant by fixing the amount of catalyst powder (metal + carbon) per cm^2 of the electrode geometrical area constant. We believe that the approach introduced in this work offers a means of unveiling the influence of carbon support on the catalyst operation in an anode of a DMFC and will ultimately allow designing an optimum carbon support for fuel cell applications.

1.5 Ethanol electrocatalysis

Direct oxidation fuel cells (DOFCs) have recently attracted major attention, as an alternative to hydrogen fuel cells, mainly due to easier fuel storage and handling. The organic liquids used for DOFCs are much simpler to handle than gaseous hydrogen and also in many cases do not require any new distribution infrastructure. The most investigated type of DOFC is direct methanol fuel cell, DMFC. The methanol has better kinetics of oxidation on the platinum based catalysts in low temperature range than all other aliphatic alcohols and is also known to oxidize completely to CO_2. This leads to better performance of DMFCs. But some disadvantages of methanol are its toxicity and relatively low boiling point. Also most of the methanol today requires natural gas as the base material, which contributes to the CO_2 emissions. Because of these shortcomings ethanol, the next alcohol is considered to be an option because of being less toxic, high in energy content (ethanol: 8kWh/kg methanol: 6kWh/kg) and its availability from renewable resources. However the kinetics of ethanol oxidation to CO_2 is much slower in comparison to methanol, as it requires not only activation of C-H bond but also the scission of a C-C bond. So in experimental conditions ethanol electro oxidation is accompanied by the formation of several unwanted intermediates or byproducts like acetaldehyde and acetic acid. The efficiency of ethanol oxidation can be improved by development of catalysts exhibiting faster kinetics and higher selectivity towards CO_2 and the optimizing the oxidation conditions.

1.5.1 Acidic medium

Various research groups have made efforts to gain mechanistic understanding of the ethanol oxidation reaction (EOR). The reaction is known to follow a complex multistep mechanism, involving a number of adsorbed reaction intermediates and byproducts resulting from incomplete ethanol oxidation.[80] The major adsorbed intermediates were identified as adsorbed CO and R_{ads} and R-C_{ads} hydrocarbon residues, whereas acetaldehyde and acetic acid have been detected as the main byproducts using differential electrochemical mass spectrometry (DEMS)[81], infrared spectroscopy[82] or chromatography[83]. Wang et al. studied the relative product distribution for the EOR in a polymer electrolyte fuel cell operating with ethanol as the anode feed using on-line mass spectrometry in the temperature range between 150 and 190 °C and water: ethanol molar ratios between 5 and 2 [84]. They reported acetaldehyde as the main reaction product, whereas CO_2 only a minor product, without much differences in the product selectivities on Pt-Ru and Pt-black catalysts. Using chromatographic techniques, Hitmi et al. found that at low ethanol concentrations the main product is acetic acid, whereas acetaldehyde is major product at high concentration (>0.1 M) during ethanol oxidation on polycrystalline Pt at 10 °C. Arico et al. investigated the electrochemical oxidation of ethanol in a liquid-feed solid polymer electrolyte fuel cell operating at 145 °C and 1 M ethanol and 2mg/cm^2 60% PtRu/C anode catalyst and reported high selectivity toward CO_2 formation (95%) under these conditions[85]. Fujiwara et al. studied ethanol oxidation on electrodeposited Pt and PtRu electrodes by model electrochemical cell DEMS for selectivity between CO_2 and acetaldehyde and reported that Ru addition helps in formation of more CO_2 and less acetaldehyde[81].

Camara et. al. on the polycrystalline Pt electrode, investigated the effects of ethanol concentration on the yields of CO_2, acetic acid and acetaldehyde as electro oxidation products using FTIR. They found acetic acid as major product at low ethanol concentrations, and CO_2 being produced to a minor extent. With increasing ethanol concentrations, the pathway producing acetaldehyde becomes dominant [86]. H. Wang et al studied the product distribution for EOR systematically as a function of temperature and concentration in a model DEMS for supported platinum catalyst (Pt/C)[87].Very low CO_2 formation was reported for EOR in their working conditions. They investigated Pt/C,Pt_3Sn/C and PtRu/C catalysts for EOR and reported that the addition of Sn and Ru increases the faradaic activity with out any increase in the CO_2 current efficiency which was reported to be 1% in all cases[88]. Lamy's

group at University of Poitiers has published many papers about the PtSn based catalyst for EOR[89-91]. Sn is proposed to activate and adsorb water at lower potential than Pt, leading to higher activity[92, 93]. They studied the product distribution of EOR in a fuel cell with HPLC and reported 20% CO_2 formation for Pt/C catalyst, which reduced to around 7% in case of Pt-Sn and Pt-Sn-Ru based catalyst. The last two catalysts were reported to favor acetic acid as the final product[94].

However, as we discussed above the results about the mechanism of ethanol oxidation varies widely depending on several parameters like oxidation in model electrochemical cell or in a real fuel cell MEA, temperature, concentration etc. Also most of systematic studies about the ethanol oxidation were done in model electrode (single crystal or thin layer electrode in electrochemical cells), which may not directly apply to real fuel cell conditions. It is our attempt in this research work to illustrate the mechanism of ethanol oxidation in real fuel cell conditions by investigating systematically the effect of various parameters like temperature, concentration, potential, catalyst layer thickness, active area in a catalyst layer, intrinsic nature of the catalyst on the CO_2 current efficiency for EOR using an in-situ technique namely fuel cell DEMS. We propose that the C-C bond cleavage rate is not only affected by the intrinsic nature of catalyst, but also similarly or even more strongly affected by the several earlier mentioned oxidation conditions.

1.5.2 Alkaline medium

Acidic proton exchange membranes (PEM) have been used in fuel cells because of their high proton conductivity and mechanical stability. Furthermore; these membrane materials are rather easily available as they are widely used in chlor-alkali electrolysis, which also helped their adoption into fuel cells. By adding the ionomer in the catalyst layer, which provided the necessary proton conductivity, the reaction interface is extended from the catalyst-membrane interface into the catalyst layer. This made the membrane electrode assembly more efficient with respect to current and power density. The completely solid phase membrane electrode assembly, without the need of any liquid electrolyte, is highly desirable as it avoids heavy corrosion problems with in the whole fuel cell system. However, despite the all above mentioned advantages, the acidic membranes are highly disadvantageous with regard to the kinetics of almost all major fuel cell processes. In particular the oxidation of any organic fuel e.g. methanol in DMFC, is kinetically much slower in acidic media than in alkaline medium. The overpotential losses are comparatively smaller, and the poisoning effect of carbonyl

species and CO which are generally stable residues of the electro oxidation process of every organic molecule, are comparatively weaker, in alkaline media. These advantages associated with alkaline medium membranes offers good incentives for their use in fuel cells. Until recently, the unavailability of proper solid alkaline membranes, which are stable under fuel cell conditions, precluded their extensive use; however, recent progress in the field of solid polymeric anion exchange membranes, has provided impetus to the application of these membranes in fuel cells. Several groups have carried out tests on these solid polymeric anion exchange membrane fuel cells[95-98]. Solid alkaline fuel cells are also attractive as they can give reasonable power output with non-noble metal catalysts because of the improved kinetics in alkaline medium and the increased stability of the non-noble metals at higher pH values.

Methanol is, to date, the most preferred liquid fuel for fuel cells because of facile kinetics in comparison to other alcohols. Some disadvantages of methanol are its toxicity and its relatively low boiling point. Ethanol, the next alcohol is considered to be an option as it is less toxic, has high energy content, and is more easily available from renewable resources. The oxidation of ethanol to CO_2 however is much slower in comparison to methanol, as it requires the scission of a C-C bond. The ethanol electro-oxidation follows a multi-step process during which several intermediates like acetaldehyde and acetic acid get formed which tends to leave the fuel cell as undesired byproducts. One possible way to achieve more complete and faster oxidation of ethanol is to employ alkaline media and to find suitable catalysts for alkaline medium. This requires detailed understanding of the mechanism of ethanol oxidation reaction (EOR) in alkaline media. But the mechanism of ethanol oxidation reaction has been studied mostly in acid medium, either liquid electrolyte or solid proton exchange membranes. EOR mechanism in alkaline medium is difficult to investigate because the main product CO_2 is highly soluble in aqueous alkaline electrolytes, due to formation of carbonates and bicarbonates, which renders it difficult to observe with techniques such as e.g. FTIR or model DEMS. It is however important to gain more understanding of the ethanol oxidation reaction in alkaline medium, especially since the kinetics of ethanol oxidation is expected to be faster in alkaline medium than acidic medium. Thus in this study it is our endeavor to shed light on the product distribution of the ethanol electro oxidation reaction in alkaline media membrane electrode assemblies. In this investigation we applied the DEMS technique to study the mechanism of ethanol oxidation reaction in alkaline medium membrane electrode assemblies (MEAs).

2. Experimental

2.1 Membrane electrode assembly

Vulcan supported catalyst 40%Pt/Vulcan from E-Tek and Alfa Aesar is utilized as the cathode catalyst. The metal catalyst loading in case of cathode is kept high at around 4mg/cm^2. For first part of this work, homemade PtRu (1:1) catalysts supported on Sibunit carbons and on Vulcan XC-72, as well as commercial 20%PtRu(1:1)/Vulcan XC-72 catalyst from E-Tek, were used for the preparation of the anode. For ethanol oxidation studies different catalysts like supported and unsupported Pt catalysts, 20%PtRu/C and 20%PtSn/C were used for preparing anode of the MEA. In order to make a MEA, a suspension of the catalyst powder, Nafion® solution (Dupont), and isopropanol were treated in an ultrasonicator. The ink was sprayed onto porous carbon backing layers (Toray paper from E-TEK, TGPH 060, no wet proofing), held at 110 ^{0}C. The 1.2 cm^2 patches of the Toray paper comprising sprayed catalyst layers were then cut and hot pressed with the Nafion® 117 membrane in between at 140^{0}C for 5 minutes at a pressure of 826 N.cm^{-2}.

2.2 Experimental setup

The fuel cell consisted of two stainless steel plates with integrated serpentine medium distribution channels. Six threaded studs and nuts held the two plates together. The fuel cell can be operated in both modes half-cell and full cell. Generally during the investigation of anode it is used as a half-cell. Cathode with high Pt loading (4mg/cm^2) and continuous hydrogen flow works as counter and reference both. Potential of the cathode is assumed to be same as of the reversible hydrogen electrode (RHE). All potential are reported in reference to this.

The anode flow system comprised of a tank filled with alcohol solution and a tank filled with water. These tanks are connected via heated tubes with the three-way valve at the fuel cell inlet. The alcohol solution and the Millipore water are always deaerated with argon. A dosing pump between the cell outlet and exit tank controls the flow of alcohol solution and water through the cell. To avoid the gas bubble formation due to the large gas production and low

solubility of CO_2 at elevated temperature, the anode flow system is pressurized at 3 bars overpressure. The cathode overpressure is kept at 1 bar to limit the crossover of H_2 to anode side. The permeation of alcohol to the cathode side does not affect the potential of the cathode (which is reference electrode also).

At the outlet channel of the anode compartment, the DEMS sensor is positioned .It consists of a cylindrical detection volume with a diameter of 7 mm and a height of 2 mm through which the anode outlet flow passes (Figure. 2.2). This volume is separated from the vacuum system of the mass spectrometer by a Microporous Teflon membrane (Schleicher & Schuell, TE30) with a pore size of 0.02 micrometer and a thickness of 110 micrometer. The membrane is supported by a Teflon disc of 2 mm in diameter, with holes. A Balzer Prisma QMS 200 mass spectrometer and a potentiostat designed by AGEF are used together with computerized data acquisition system to record the experimental data.

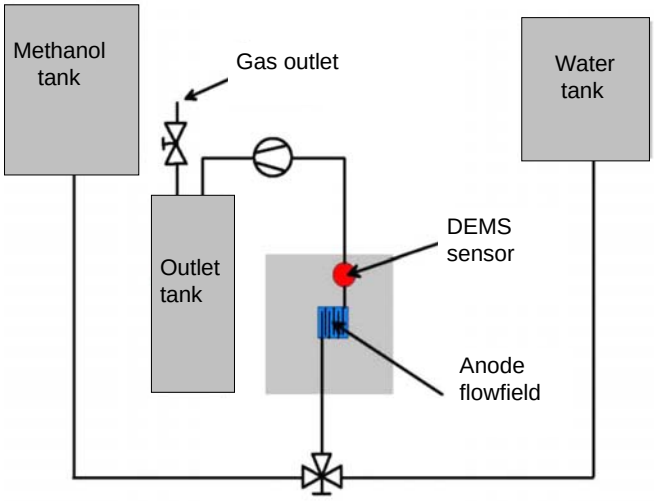

Figure 2.1. Schematics of the fuel cell DEMS setup.

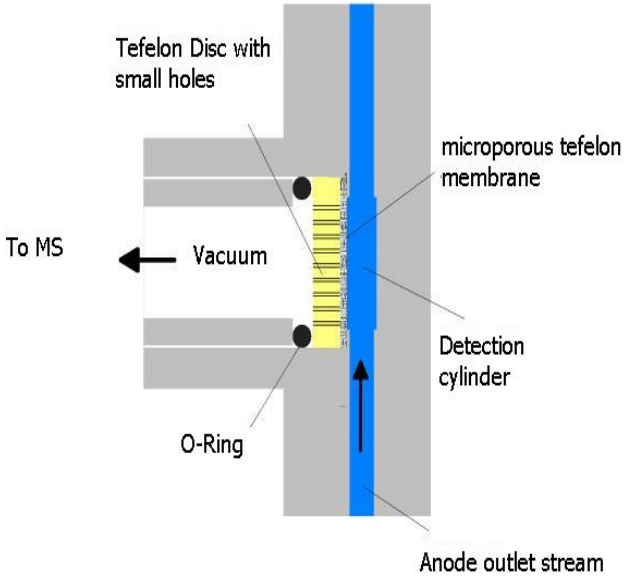

Figure 2.2. Design of MS sensor.

2.3 Calibration of FC-DEMS system

2.3.1 CO stripping for calibration and related problems

The calibration of the Model DEMS systems is done by electrochemical oxidation of a monolayer of CO on the catalyst sites, and simultaneously recording the faradaic current and the mass 44 (CO_2) signal .The calibration constant is defined as:

Calibration Constant $K_F^* = 2*Q_{ms}\backslash Q_f$

Q_{ms} : integrated MS ion current charge under CO oxidation peak calculated from a MSCV.

Q_f : integrated faradaic current charge under CO oxidation peak calculated from CV.

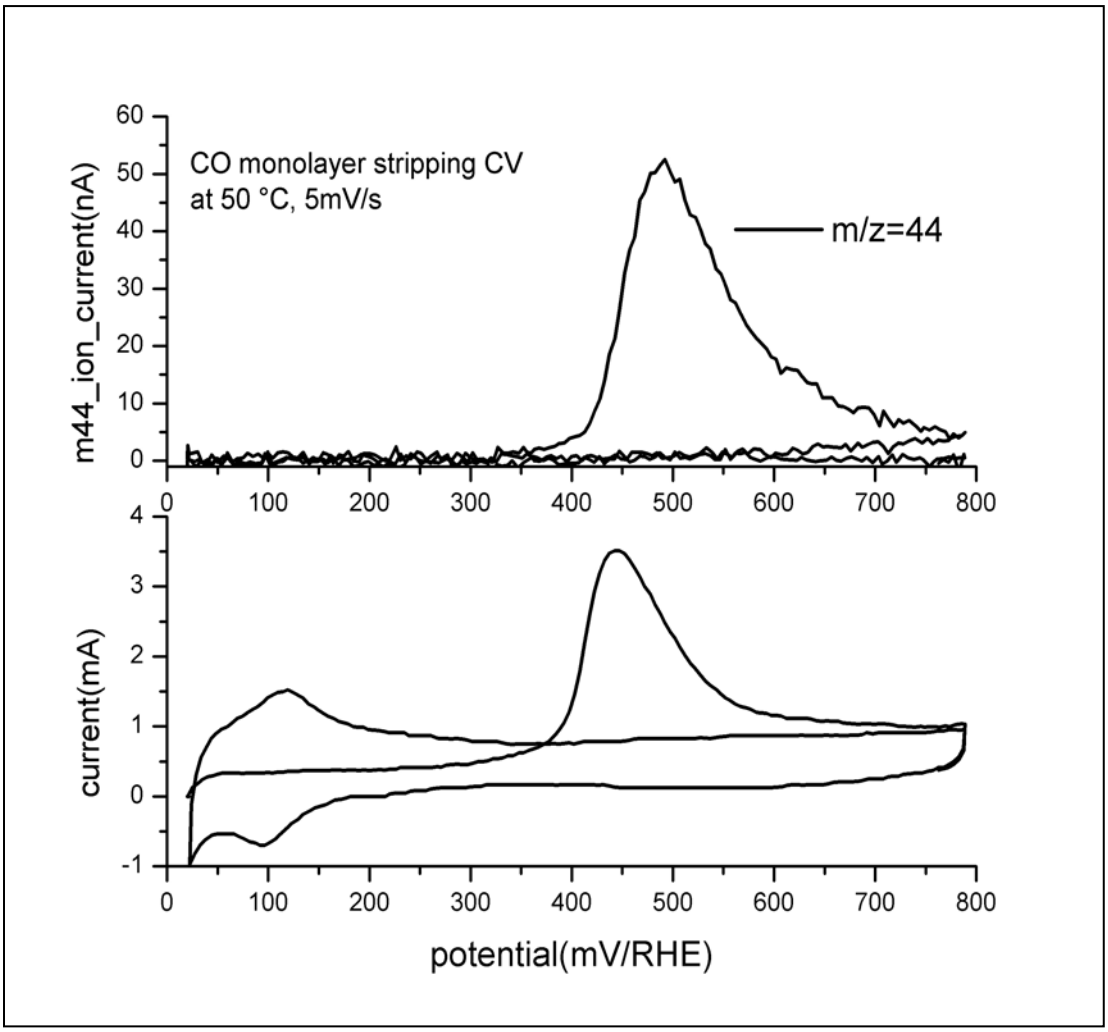

Figure 2.3. This figure shows the typical CV and MSCV.

But in context of our Fuel Cell DEMS setup, there are three main problems.

Double layer charging

Integrated faradaic charge under a CO stripping peak contains some double layer charge. It is a general problem with CO monolayer oxidation as calibration method. Model system and fuel cell DEMS setup both will face this. Amount of double layer charge depends on the composition of catalyst. For example: pure platinum catalyst have only 20% extra charge because of double layer but a PtRu(1:1) catalyst have around 50% double layer charge[99].

Crossed-over H_2 oxidation current interference in Faradaic Current

This problem is typical to our kind of setup with gaseous H_2 at cathode, which works a counter and reference electrode both. H_2 diffuses through Nafion membrane separating cathode and anode, at a rate of 10^{-10} mol per cm^2 per second per atm. This much H_2 can give rise to anodic currents between 0.25-1mA, which results from the oxidation of crossed-over H_2 at the anode side. This current might seem to be small but it is non–negligible in case of low faradaic current processes like CO monolayer stripping and CO bulk oxidation. This H_2 oxidation current results in unsymmetrical distortion of the CO stripping CV. The graphs shown below correspond to the CO monolayer oxidation on the 40wt% Pt/C Johnson Matthey catalyst. The point to note in the graphs shown below is that the H_2 oxidation current picks up only when some Pt sites becomes free after the oxidative removal of adsorbed CO. As is clearly visible from the m/z = 2 signal vs. time during CO stripping. The H_2 ion current dip down at the starting of the CO oxidation and then afterwards diffused H_2 oxidation current also get added to the real CO oxidation current. From such unsymmetrically distorted CV, it is ambiguous to calculate the stripping faradaic charge. In model DEMS systems since there is no such extra H_2 oxidation current (because of H_2 diffusing from cathode to anode), this method of calibration works fine but surely not in our fuel cell-DEMS system.

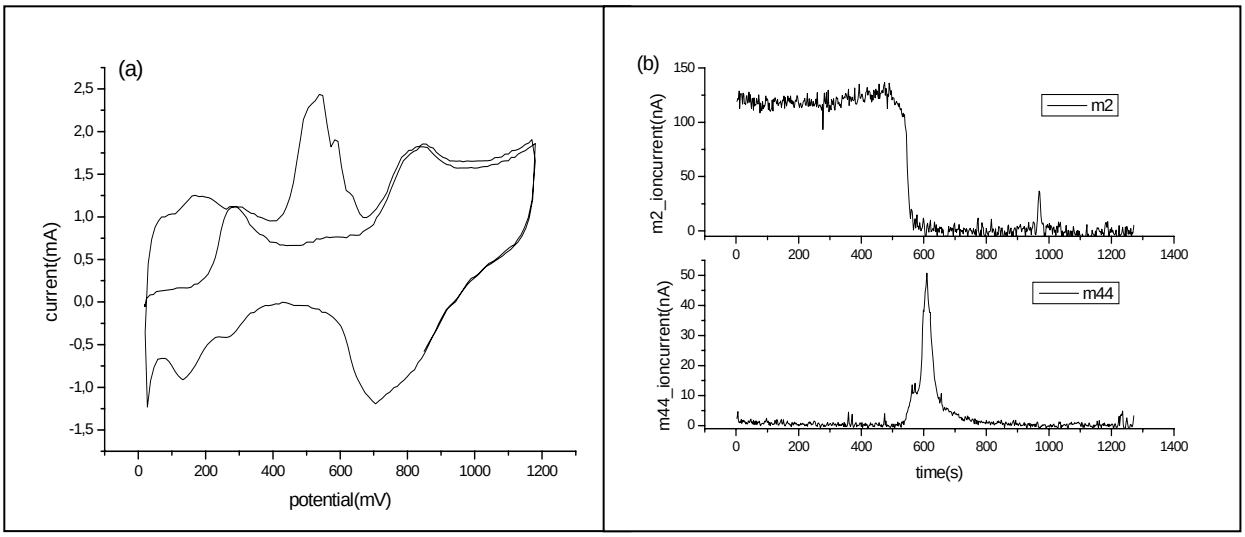

Figure 2.4. (a) This figure shows the CO stripping CV for Pt/C catalyst. (b) m/z =44 (CO_2) and m/z =2 (H_2) are shown as function of time. The H_2 signal drops down as the CO monolayer is stripped off.

Diffusional problems

Our Fuel Cell DEMS setup has a fuel cell with a gas diffusion electrode and a thick catalyst layer. The response time between faradaic and MS ion current is large (around 5-10 seconds). Such large times make it difficult to correlate faradaic and MS ion currents and results in long tailing ion currents in MS. For example the graph shown below is a plot of mass 44 ion current (for CO monolayer oxidation) vs. time.

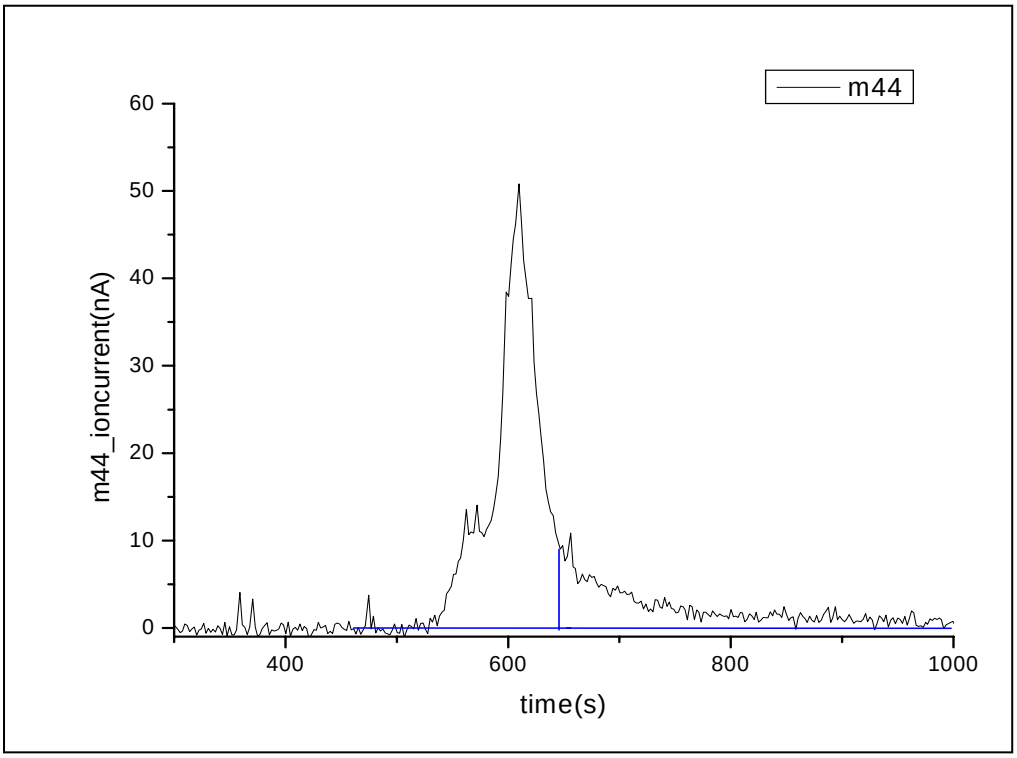

Figure 2.5. The m/z =44 signal is shown as a function of time. The signal decays slowly because of diffusional elements in the MEAs and also slow response time of the FC- DEMS setup.

2.3.2 Potentiostatic bulk CO oxidation for calibration

Because of the above mentioned problems with CO monolayer stripping based calibration method, we decided to use another method based on continuous potentiostatic bulk CO oxidation for calibration of our fuel cell DEMS setup. This method offers following advantages:

• Being a potentiostatic method it counters the problem of the double layer charge involved in the faradaic charge calculation in CO stripping CV.

•Counters the diffusional problems, since no mass signal transients are involved.

$K^*_F = 2*I_{MS}/I_F$

I_{MS} is mass 44 ion current in steady state
I_F is the corresponding faradaic current in steady state

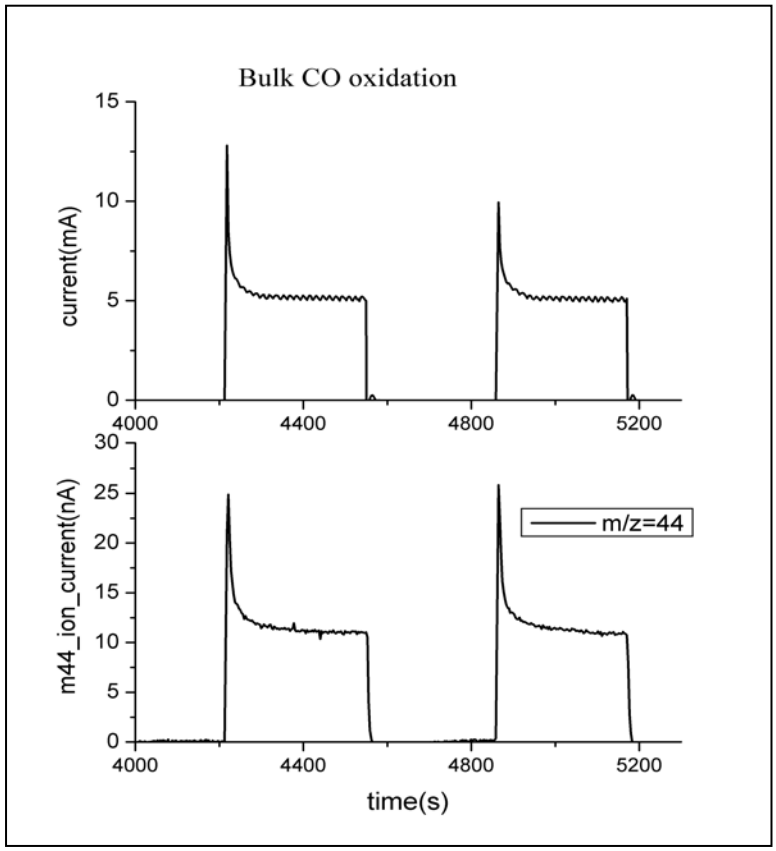

Figure 2.6. Current and m/z =44 signal are shown as a function of time, for potentiostatic CO bulk oxidation experiment.

•But diffused (from cathode to anode) H_2 oxidation current still gets added to the faradaic current. Crossed-over H_2 oxidation current needs to be measured exactly at same potential in water, at which CO bulk oxidation is done. Thus measured crossed-over H_2 oxidation current is subtracted from the overall faradaic current of CO bulk oxidation. The resulting current is the true faradaic current to be used in calculation of the calibration constant.

•The diffused (from cathode to anode) H_2 oxidation current should be measured on the same day of Experiment, as this is not constant and can vary with age of MEA and also potential of anode. For example: in our case the bulk CO oxidation current is around 5mA and out of which 0.25 –1 mA can be the diffused (from cathode to anode) H_2 oxidation current. This could give rise to errors of about 20%, if not subtracted.

2.4 Description of electrochemical cell setup

The electrochemical cell consists of three electrodes, working electrode (WE), reference electrode (RE) and counter electrode (CE). The working electrode, in our case is a smooth gold disk, with a very thin probe catalyst layer deposited on it. The substrate gold electrode has a wide neutral potential window and also has very low surface area compared to the nanoparticle probe catalyst layer. So the contribution of gold disk to electrochemical currents is negligible. Every electrochemical system in daily life has only two electrodes, however the electrochemical measurements are done in three electrode system, because we want to study one electrode at a time or in other words to exclude the effect of second electrode. This is done by separating the current carrying electrode and the potential measurement electrode. In an electrochemical cell the counter electrode is the current carrying electrode and the reference electrode is the potential measurement electrode. In this configuration, the reference electrode carries very small current required to sense the potential. This small current causes the potential drop across the RE independent of cell current.

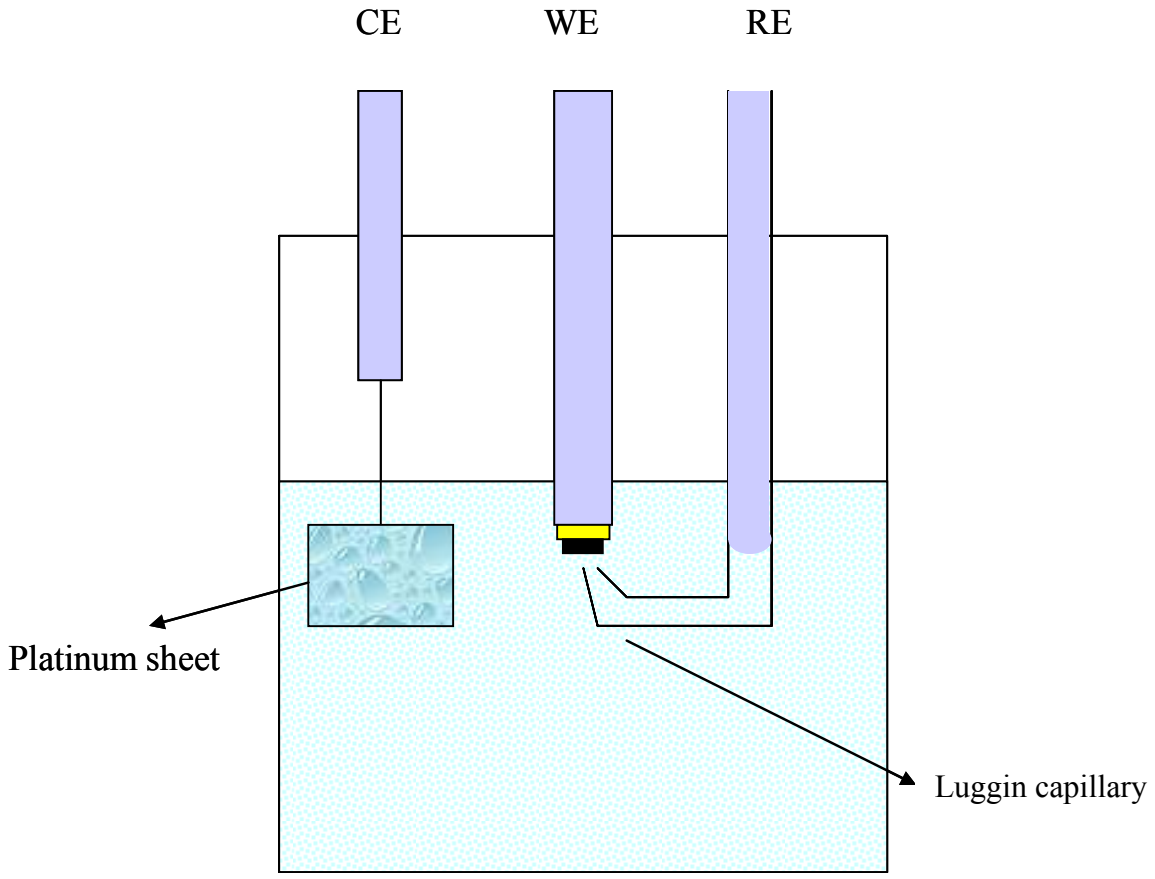

Figure 2.7. Typical electrode arrangements in an electrochemical cell.

If we choose a standard reference electrode, with good stability over the temperature and other operating conditions, then potential drop across the RE would be will be reproducible and stable over all operating conditions of the electrochemical cell. This precise measurement of the potential by RE allows us to study the electrochemical process on the WE independently and free of any interference from any other electrode. In this study the RE is saturated $Hg/HgSO_4$ electrode. At the counter electrode takes place the counter reaction, so as to compensate the electrolyte solution for species consumed or produced at the working electrode. For example if one particular electrochemical reaction produces protons at the WE e.g. methanol oxidation, then excess protons has to be evolved out of the electrolyte solution as H_2 gas at the counter electrode. The electrochemical reaction at the counter electrode depends on the nature of the electrochemical reaction at the working electrode. The potential of the CE is accordingly managed by the potentiostat.

The potentiostat is an electronic device used to apply desired potential or current to the working electrode. The potentiostat observes the potential difference between the WE and RE, and pumps current through the CE, such that the potential difference between the WE and RE remains constant at some predefined value set by the user. This value can be anything depending on the nature of the experiment in concern. If the potential of the working electrode is cycled between some upper and lower limit with a defined potential scan rate, and corresponding current is measured, then such an experiment is called cyclic voltammetry. This technique is most frequently used in electrochemical experiments.

3. Characterization of anode in a direct methanol fuel cell

3.1 DMFC anode catalyst layer properties

The major problem with the commercialization of direct methanol fuel cell technology is prohibitive cost of noble metal catalyst needed to get reasonable power densities. The use of supported catalysts in hydrogen fuel cells helped in reducing the amount of Pt needed by two orders of magnitude, to around 0.1mg/cm^2. But the use of supported catalysts did not have the same effect for direct methanol fuel cells. Methanol oxidation kinetics is much sluggish compared to hydrogen oxidation. So generally we need to have loadings like 6-10mg/cm^2 of unsupported catalysts. Although the Vulcan supported catalysts are well known to have 4 times more mass activity[100], and as has been reported in literature, with some optimizations in morphology and structure of the carbon supports, further increase by a factor of 3-4[60, 69] ,in mass activity can be achieved. So there is potentially at least a factor of 10 between the mass activities of supported and unsupported catalysts. But this immense potential remains unrealized because of some problems with structure of the anode catalyst layer made of carbon supported catalyst. In this chapter some experiments performed to gain further understanding of various parameters related to the anode catalyst layers will be discussed. We will also discuss some strategies to overcome these problems.

3.1.1 Measurement of electrochemically active area by CO stripping

Because of sluggish methanol oxidation kinetics, the noble metal catalyst loading in anode of a DMFC required for any reasonable current density is normally high at about 5-6mg/cm^2 of unsupported PtRu. The carbon supported catalyst which has shown good activities in thin layers may help in reducing the amount of noble metal required. But the high activity advantage is lost as soon as the thickness of the catalyst layer increases after certain value. Catalyst layer thickness is much higher in case of supported catalyst case, for any particular metal catalyst loading. For 20% PtRu/C and a loading of 0.2mg/cm^2, the thickness already reaches around 20 μm. But same thickness for 60% PtRu/C, is reached at loading of 1mg/cm^2 and for unsupported PtRu 20μm is reached at a loading of 4mg/cm^2. This big difference in metal catalyst loading for same thickness of the catalyst layer is because of the presence of low-density carbon support in case of supported catalyst. The increased thickness of the catalyst layer in case of supported catalyst possibly may leads to mass transport problems, low proton conductivity and low electrical conductivity. Now to find out if the increase in

thickness of the catalyst layer can lead to any section of the catalyst layer becoming electrochemically inactive, we measured the electrochemically active area in the anode catalyst layers with different metal catalyst loading, using the CO stripping technique.

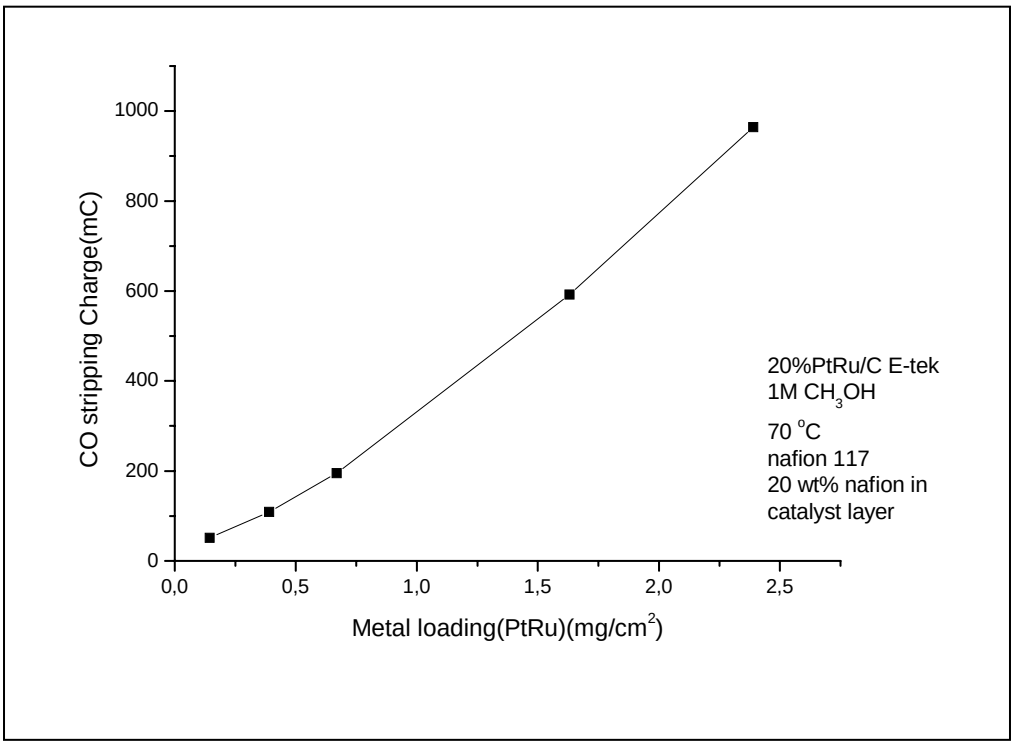

Figure 3.1. CO stripping charge as a function of catalyst loading for 20%PtRu/C catalyst.

From the CO stripping voltammogram we can calculate the charge under the CO stripping peak. This "CO stripping charge" is directly proportional to the electrochemically active area. Figure 3.1 shows the "CO stripping charge" or electrochemically active area increases linearly with the increasing metal catalyst loading. This indicates that the electrochemically active area is not dependent on the catalyst layer thickness. This result is understandable from the fact that CO stripping involves only one time oxidation of adsorbed monolayer of CO and faradaic current involved are low. So the electronic and protonic resistance of the catalyst layer does not affect the CO stripping charge. Also oxidative removal of one CO monolayer is not much affected by the mass transport resistance. But as we will see later, in a continuous polarization case with relatively high faradaic currents, ohmic resistance and mass transport resistances plays major role in activity losses in thick catalyst layers.

3.1.2 Measurement of electrochemically active area by $MeOH_{ad}$ stripping

Dissociative MeOH adsorption on Pt surface also leads to formation of a strongly adsorbed

CO_{ad} or CO_{ad} like species. In CO stripping experiment CO is adsorbed on to the Pt sites from the flowing CO saturated de-ionized water. Now to investigate if the electrochemically active area measured by CO stripping, is also active for MeOH dissociative adsorption, we allowed Methanol to adsorb at non-oxidizing potential and reach a saturation coverage. The Methanol adsorbates were than oxidatively stripped by cycling between 0 and 0.8V. The charge from the MeOH adsorbate stripping CV was calculated for different catalyst layers with different metal catalyst loading. The MeOH adsorbate stripping charge also shows approximately a linear behavior with increasing catalyst loading. The surface CO_{ad} coverage reached by MeOH adsorption is around 70-80% of the surface coverage reached by CO adsorption from CO saturated water in CO stripping experiment. This agrees well with already published data for PtRu/C catalyst[101]. The linear increase in MeOH adsorbate stripping charge with the increasing catalyst loading indicates that the thickness of the catalyst layer do not affect adsorption of methanol up to one monolayer of CO_{ad}. The explanation for this behavior is that the bad effects of thick catalyst layer do not come into play in these MeOH adsorption and stripping experiments, as was the case with CO stripping experiment.

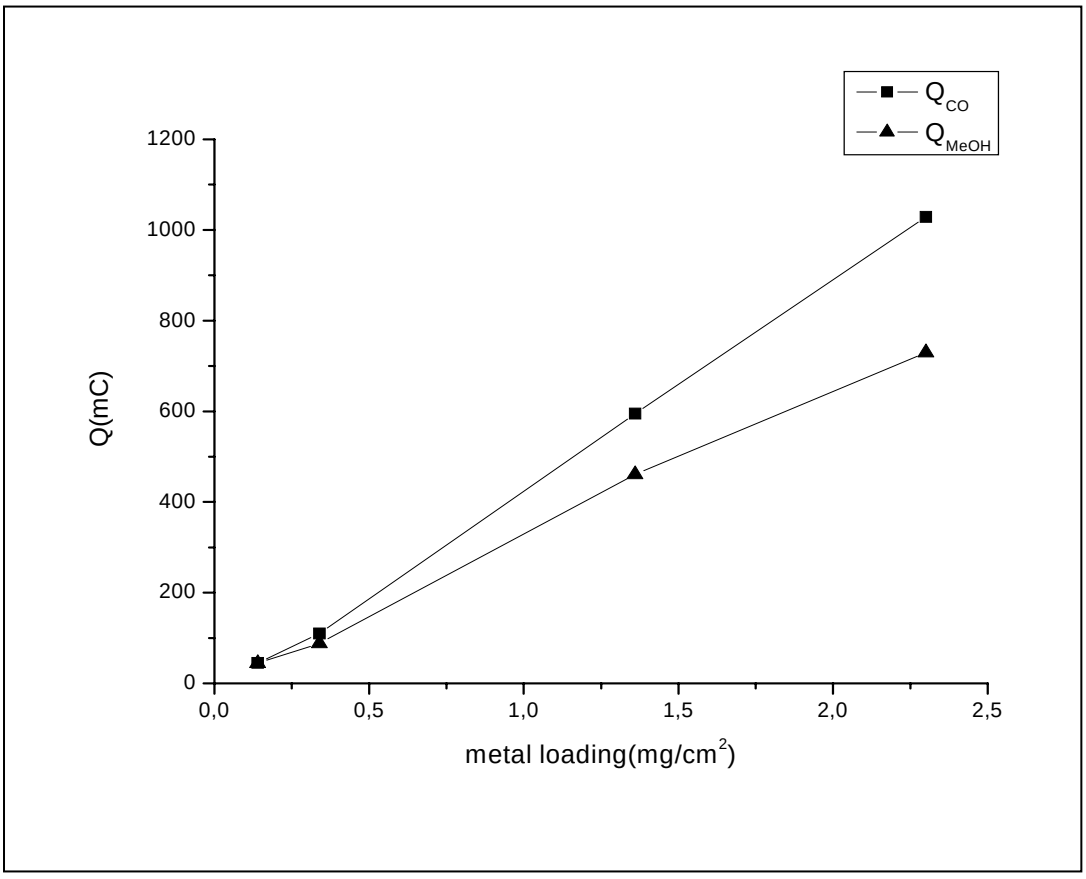

Figure 3.2. CO stripping and methanol adsorbate stripping charge as a function of catalyst loading for 20%PtRu/C catalyst.

3.1.3 Measurement of methanol oxidation current

The methanol oxidation currents were measured for different catalyst layer thicknesses and thus different metal catalyst loadings using the 20%PtRu/C catalyst. The results of these experiments are shown in Figure 3.3 for two potentials of polarization of the half-cell namely 0.4V and 0.5V/RHE. The methanol oxidation current at both potentials increases with increasing catalyst loading. At lower catalyst loading and thus lower catalyst layer thickness the current increasing linearly, but rate of this increase slows down rapidly with increasing catalyst loading and a saturation kind of behavior is seen. For the highest loading case the current is lower than the previous loading case. This behavior is expected for all supported catalysts. But, the "linear increase region" in current @particular potential, will depend on the metal % of that particular catalyst. The higher metal % would mean lower catalyst layer thicknesses, which may help in achieving broader linear increase region. The unsupported catalyst would show the broadest linear increase region. The graph show one point for unsupported catalyst layer with 4mg/cm^2, with exhibits much higher currents in loading range.

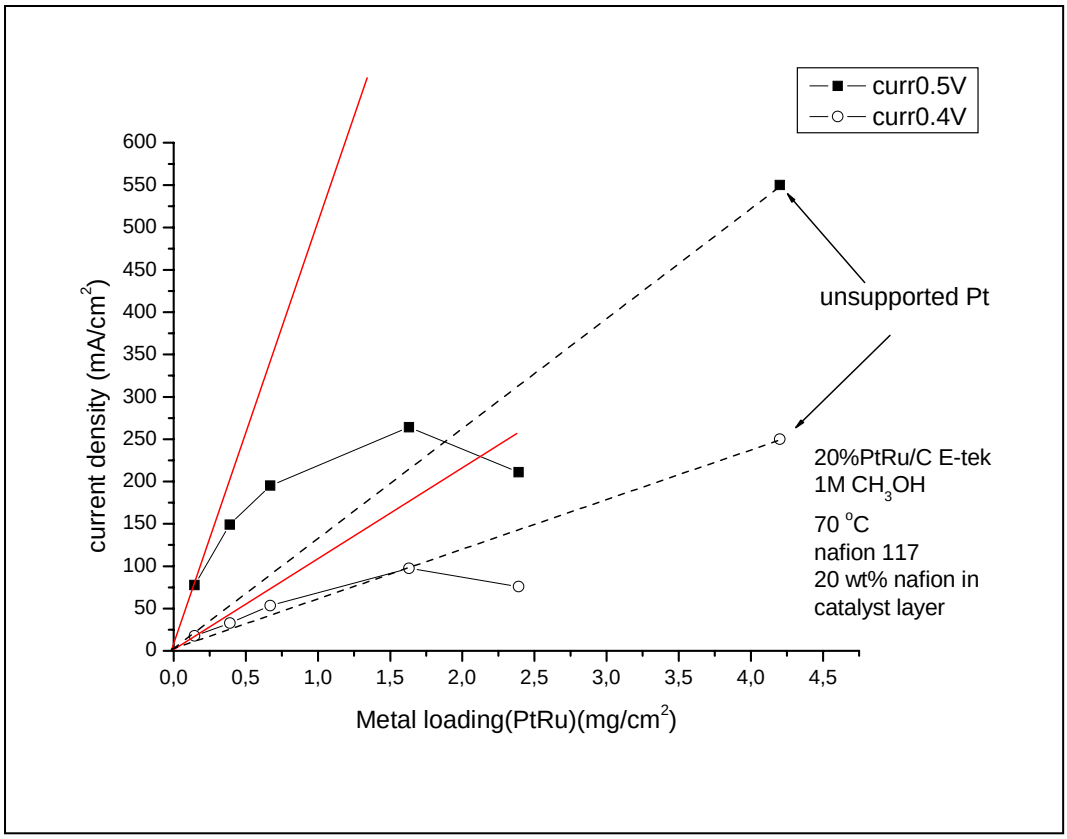

Figure 3.3. Currents at 0.4V and 0.5V/RHE are shown as a function of catalyst loading.

The linear increase region in the current vs. catalyst loading graph and then the saturation effect can be explained by considering the impact of three parameters namely: the protonic resistance, the electronic resistance of the catalyst layer and the mass transport losses in the catalyst layer. To be able to quantify the individual exact impact of all three parameters would require knowledge about their values in real experimental conditions.

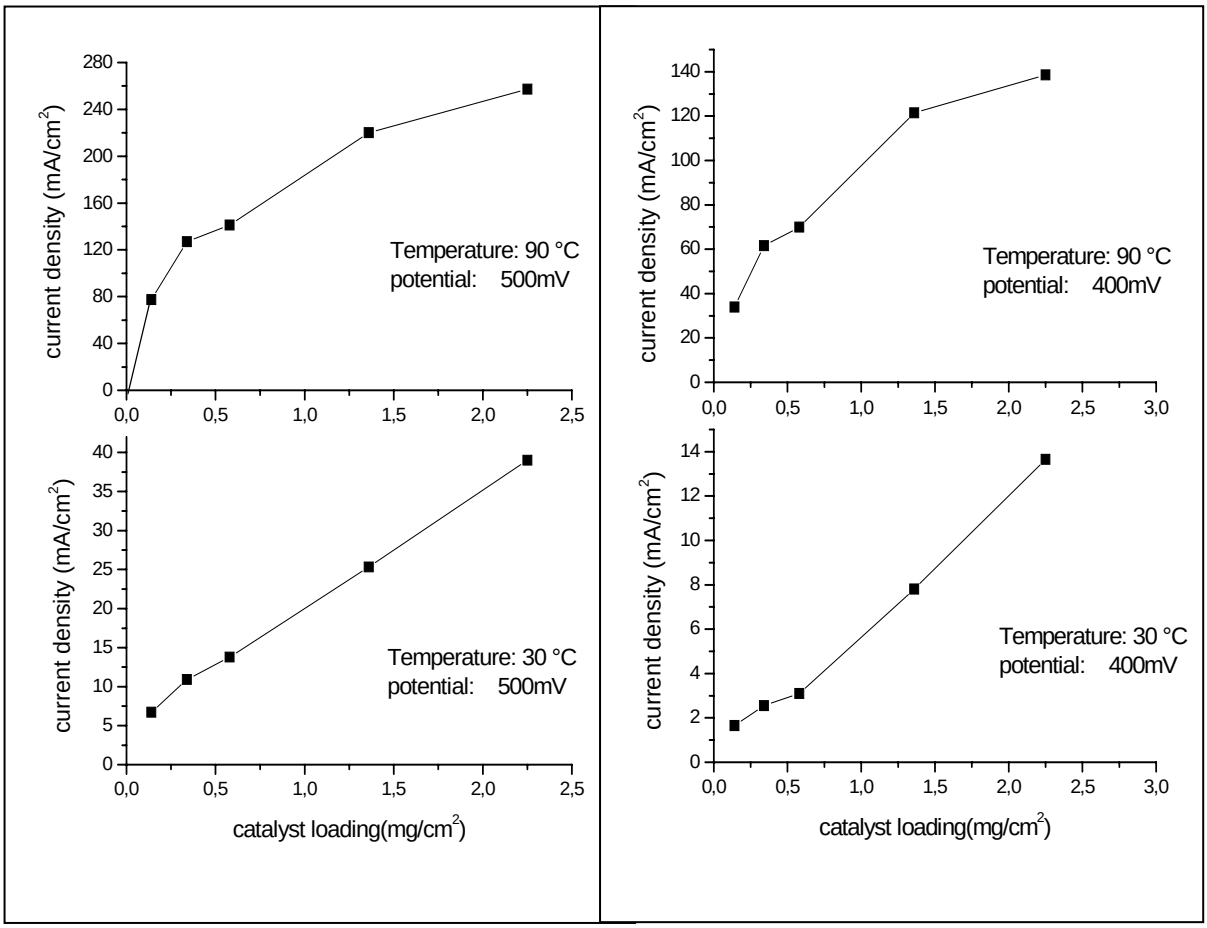

Figure 3.4. Currents at different conditions are shown as a function of catalyst loading.

But simple conclusions can still be drawn. One of such conclusion is that the saturation effect is much faster reached in high current density range (see Figure 3.4, 90°C data). But for lower current density range the saturation effect is not present. The currents increase linearly with catalyst loading in low current range (see Figure 3.4, 30°C data). In low current range the ohmic losses in the electronic media and the electrolyte media are small and also the mass transport losses are small. That's why the currents increase linearly with increasing catalyst loading.

3.1.4 Simplistic catalyst layer model

This section presents a simple catalyst layer model, which may help in explaining the earlier presented experimental results. In this model we do not take in to account impact of mass-transport problems in the catalyst layer. Mass transport losses can be minimized by choosing the high flow stoichiometry for anode of the half-cell. For all of our experiments the methanol flow stoichiometry was kept excessively high at a value of more than 100. In principle around 70% porosity of the pressed catalyst layers should provide enough space for mass-transport. The CO_2 solubility limit at 70°C is around $1.4*10^{-2}$ mol/L [102, 103]. In our conditions, 5ml/minute flow rate of 1M CH_3OH (4vol% methanol water mixture) solution at 70°C, the CO_2 concentration reached at a current density of $0.5A/cm^2$ is $1*10^{-3}$ mol/L. Since the current density observed in our experiments is always lower than $0.5A/cm^2$, the CO_2 concentration remains below 10% of the solubility limit. Only after crossing the solubility limit one could expect the bubble formation and two-phase flow and mass-transport limitations caused by bubbles. Thus taking into account very high methanol flow stoichiometry and high solubility of CO_2 in water, for simple and approximate calculations, we neglect the impact of mass transport across the catalyst layer. Figure 3.5 shows a schematic diagram of anode of half-cell Membrane electrode assembly. The catalyst layer (CL), is contacted by gas diffusion layer (GDL) on one side for electrical current collection and by the polymer electrolyte membrane (PEM) on the other side for providing electrolytic contact for conduction of protons to cathode side. Generally the CL also has some electrolyte ionomer impregnated, which provides proton conductivity inside the catalyst layer. The proton conductivity inside the catalyst layer is determined by the volume fraction of the proton conducting ionomer phase. Figure 3.5 also shows the potential distribution across the catalyst layer. V_o is the anode potential at current collector, which is in turn determined by the load in case of full cell DMFC or is applied by a potentiostat in case of half-cell. But the electrical conductivity of the catalyst layer is lower in comparison to the GDL because of the presence of non conducting electrolyte phase. Catalyst layer is also the source of electrical current. So when electrical current flows through the catalyst layer, due to ohmic losses electrical potential felt in the electronically conducting phase of the catalyst layer becomes lower as one move away from the GDL into the catalyst layer. In Figure 3.5, the profile of the electrical potential is shown linear for the sake of simplicity. The actual profile can only be calculated by solving differential equation satisfying ohm's law in electronic and electrolyte phase. A detailed solution of similar problem was performed for SOFC anode cermets by Divisek et al.[104, 105]. Figure 3.5 also shows the potential profile in the electrolyte phase. The proton

conductivity of the bulk electrolyte phase e.g. nafion (0.1S/cm) is very small in comparison to typical electrical conductivity of graphitic carbons powders (1S/cm). Since the catalyst layer only has a fraction of its overall volume occupied by proton conducting phase, the proton conductivities are typically very small (1-10mS/cm) . So accordingly Figure 3.5 shows more ohmic losses in the electrolyte phase. The difference of the potential in electronically conducting phase and proton conducting phase is overpotential felt by the catalyst layer.

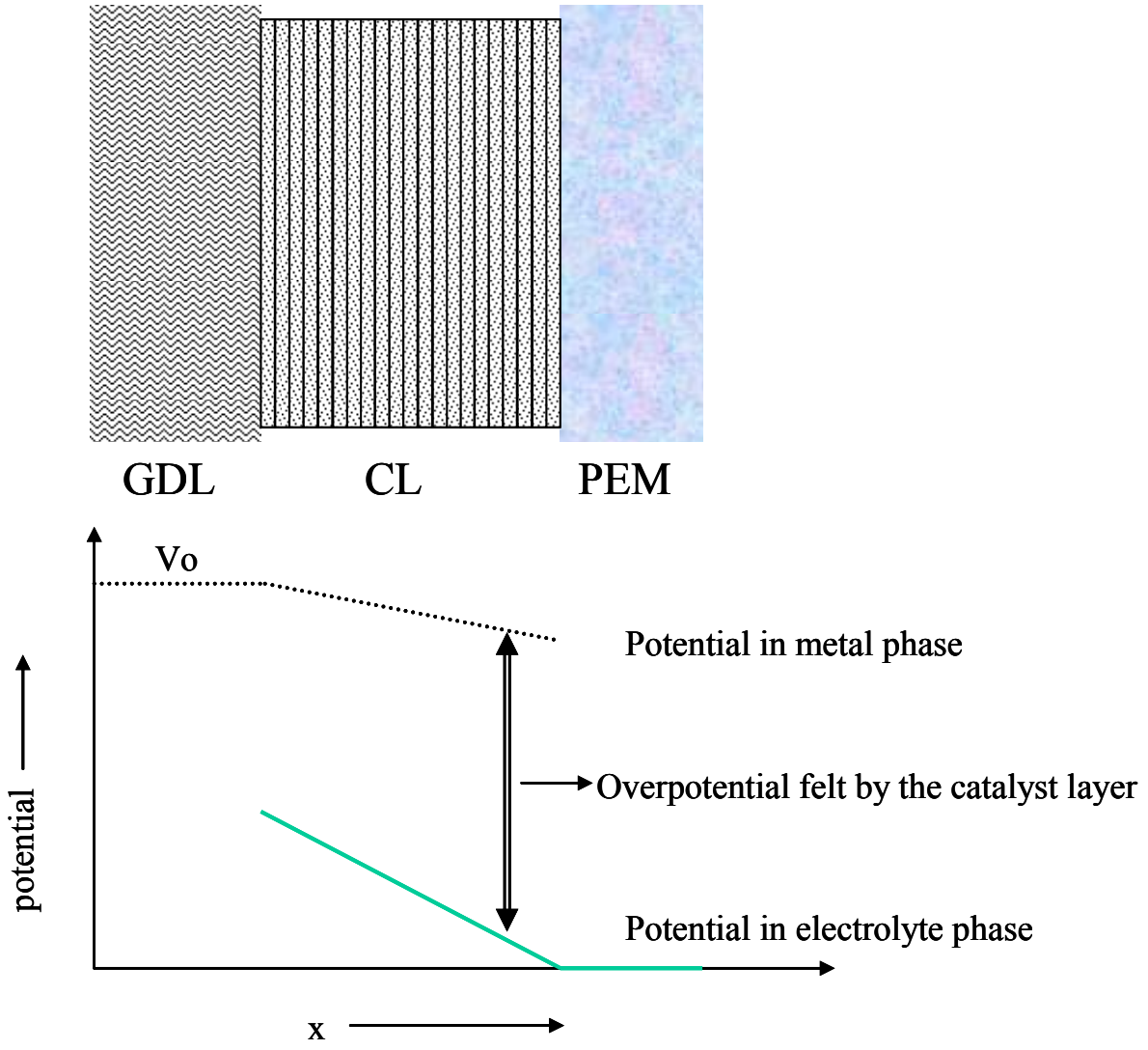

Figure 3.5. Schematic diagram shows the potential profiles across the catalyst layer in electrolyte media and the electron conducting media.

Boyar et al. [106] measured the proton conductivity in the catalyst layer for supported catalyst made PEMFC electrodes. They reported that the proton conductivity is proportional to the volume fraction of the nafion phase. For example the proton conductivity of 33 wt% nafion and 67wt% carbon was found to be 13mS/cm and for a higher nafion amount of 60 wt% and

rest carbon, 18mS/cm was reported.

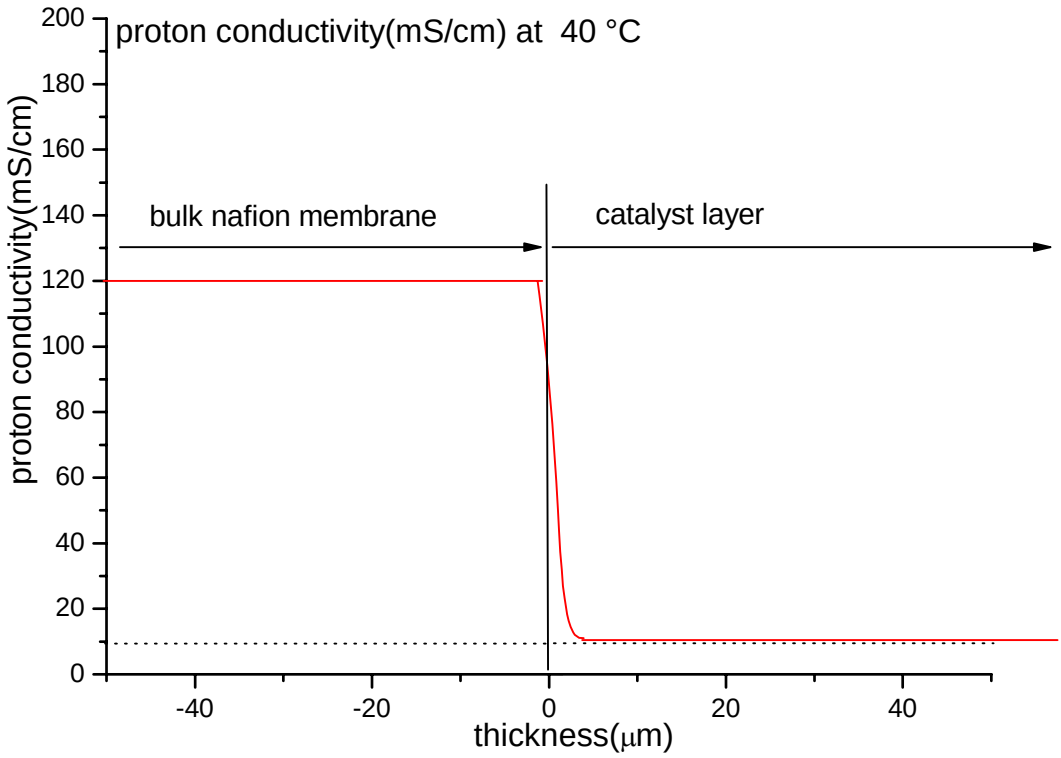

Figure 3.6. The proton conductivity across the MEA.

For carbon powders having electrical conductivity because of the presence of some graphitic phase, the electrical conductivity depends on volume fraction, which is related to extent of compaction or the pressure at which the powder layer is compressed. Different types of carbon can have different response to compaction. The carbons which are harder have some advantage, because they will retain the pore structure even after compaction. But in case of softer carbons like carbon black, this will not be the case.

Another point to note is that as a general rule, the higher the specific surface area of the carbon support, the lower the electrical conductivity. The electrical conductivity of the carbon powders depends on the pressure of compaction. A generally reported value of 4 S/cm at a volume fraction of 0.3 for Vulcan XC-72, is achieved at a compaction pressure of 3-4 Mpa [107].But the electrical conductivity in real fuel cell catalyst layer will depend on the volume fraction of the carbon, volume fraction of nafion and also on the pressure of compaction. No paper in literature was found on electrical conductivity measurement in catalyst layers made of supported catalysts, with nafion incorporated. But taking into account the porosity of the catalyst layer of about 70%, and a nafion volume fraction of 10-15% in the catalyst layer, we

could expect an electrical conductivity of at least about 1S/cm proportional to the volume faction of the conducting carbon phase. The experimental measurement of electrical conductivity of the catalyst layer was performed using a DC technique which involved measurement of resistance of two pressed sandwiches, namely GDL-GDL and GDL-CL-GDL. This experiment yielded an estimate of about 250mS/cm for the electrical conductivity of the catalyst layer. So for first approximate calculations we assume that the ohmic losses in the electrolyte phase with a proton conductivity of around 10mS/cm will be significantly more than ohmic losses in the electronically conducting phase. Thus calculations were made taking into account the overpotential losses only in the electrolyte phase. Figure 3.7 shows the experimental data of currents at 0.4V/RHE in a half-cell, with different anode catalyst loadings. Now for calculations for the whole catalyst layer, the performance of the thinnest catalyst layer which has 0.14mg/cm^2 metal loading and 10µm thickness is assumed to be free of any ohmic losses. The polarization curve (Figure 3.8) for this thinnest layer is then used for making calculations for the whole catalyst layer. If there were negligible ohmic losses in the catalyst layer, then we can expect completely linear behavior between the current and the catalyst loading, as shown by the red line in Figure 3.7.

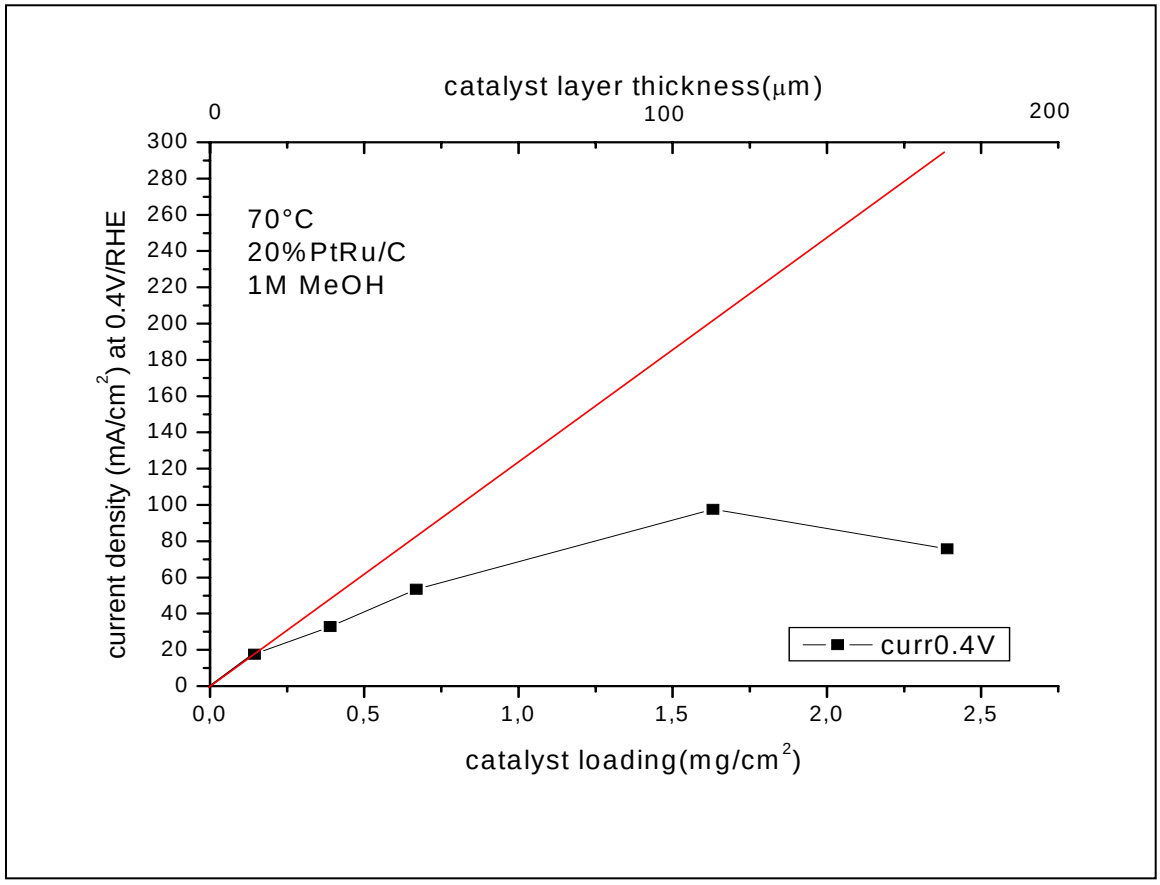

Figure 3.7. This figure shows the currents at 0.4V, for different catalyst loadings. The line indicates the ideal behavior expected if there are no losses in catalyst layer.

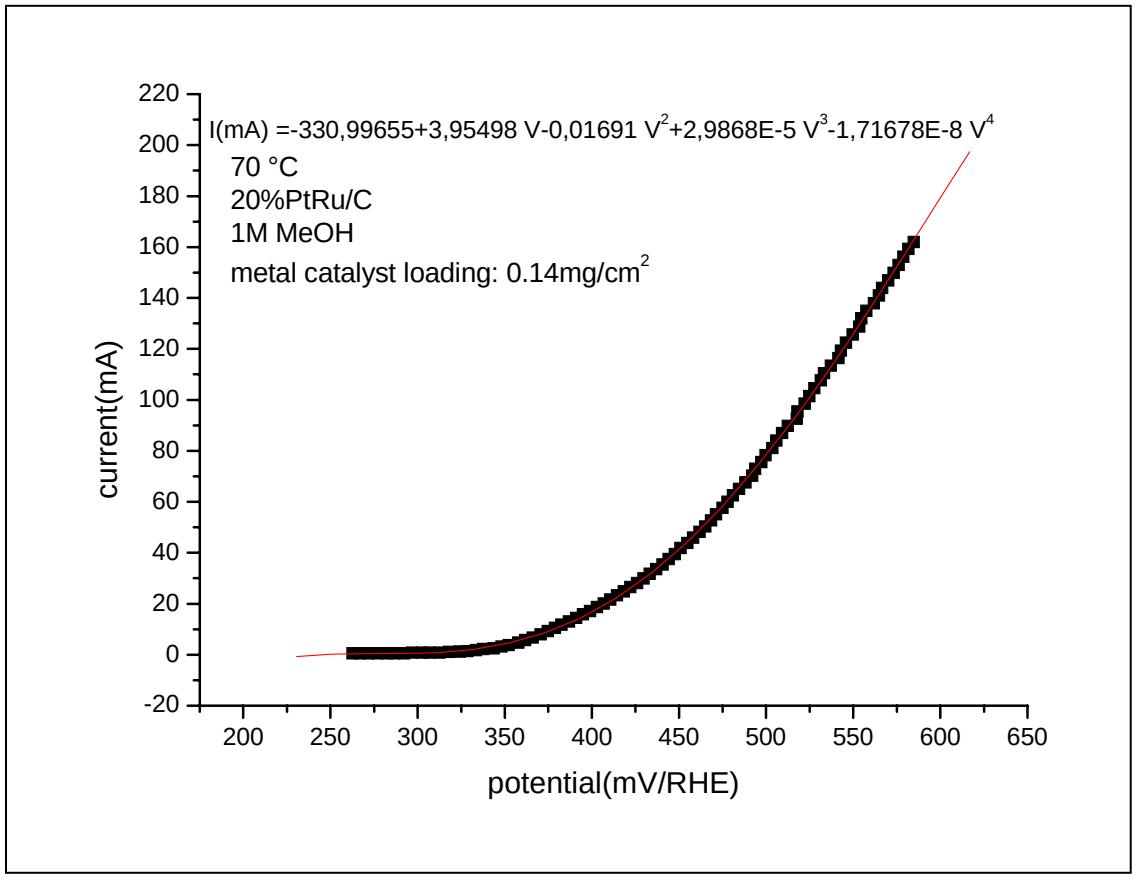

Figure 3.8. The current-potential characteristics for the catalyst layer with lowest catalyst loading.

For calculating the overpotential profile within the catalyst layer, it is divided into appropriate number of layers each with 0.14mg/cm^2 metal loading or 10 μm thickness. With the proton conductivity of 10mS/cm, the protonic resistance of each layer is R_p = 0.1 Ohm.

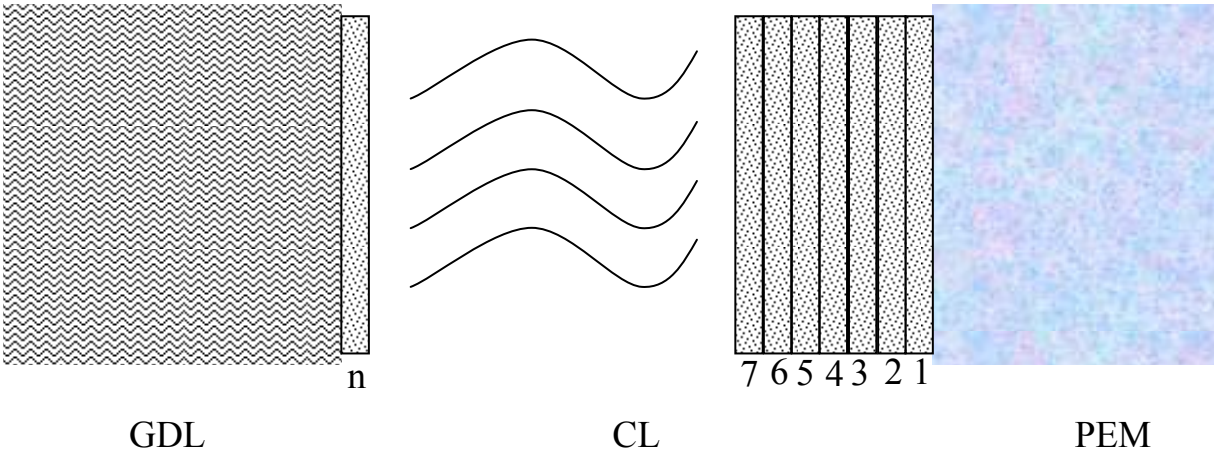

Figure 3.9. Scheme shows the partitioned catalyst layer, into small catalyst layers.

Ohm's law in electron conducting phase

$$\frac{\mathrm{d}\phi_{\mathrm{m}}}{\mathrm{dx}} = \rho_m i_m(x) \qquad --------(1)$$

Ohm's law in electrolyte phase

$$\frac{\mathrm{d}\phi_{\mathrm{e}}}{\mathrm{dx}} = \rho_e i_e(x) \qquad --------(2)$$

ϕ: potential, ρ: resistivity, i: current in respective phase

Over-potential in catalyst layer

$$\eta(x) = \phi_{\mathrm{m}}(x) - \phi_{\mathrm{e}}(x)$$

$$\text{for } \rho_m >> \rho_e \Rightarrow \frac{\mathrm{d}\phi_{\mathrm{m}}}{\mathrm{dx}} = \rho_m i_m(x) = 0 \Rightarrow \phi_{\mathrm{m}}(x) = \text{constant} = \mathrm{V}_0$$

$$\eta(x) = V_0 - \phi_{\mathrm{e}}(x)$$

$$\Rightarrow \frac{\mathrm{d}\eta}{\mathrm{dx}} = -\frac{\mathrm{d}\phi_{\mathrm{e}}}{\mathrm{dx}} \Rightarrow \frac{\mathrm{d}^2\eta}{\mathrm{dx}^2} = -\frac{\mathrm{d}^2\phi_{\mathrm{e}}}{\mathrm{dx}^2}$$

Current balance in electron-conducting and electrolyte phase

$$i_m(x) + i_e(x) = \text{constant} \Rightarrow \frac{\mathrm{d}i_m(x)}{\mathrm{dx}} = -\frac{\mathrm{d}i_e(x)}{\mathrm{dx}}$$

Electrochemical current generation:

$$\frac{\mathrm{d}i_e(x)}{\mathrm{dx}} = \frac{i_e(\eta(x))}{l} \qquad --------(3)$$

Coupling above written equations

$$\frac{\mathrm{d}^2\phi_{\mathrm{e}}(x)}{\mathrm{dx}^2} = \rho_e \frac{\mathrm{d}i_e(x)}{\mathrm{dx}} = \rho_e \frac{i_e(\eta(x))}{l}$$

$$\Rightarrow \frac{\mathrm{d}^2\eta(x)}{\mathrm{dx}^2} + \rho_e \frac{i_e(\eta(x))}{l} = 0$$

with $i_e(\eta(x))$ being exponential in nature, analytical solution is difficult

For an approximate solution to above mentioned problem, the catalyst layer is divided into n thin layers of 10μm thickness which corresponds to a catalyst loading of 0.14mg/cm^2. The proton conductivity is taken to be 10mS/cm, in accordance with literature. In this partitioned version of the catalyst layer, the prospective $i_e(\eta(x))$ solution must satisfy equations (2) and (3). The discrete versions of these two equations are:

Electrochemical current generation :

$$\frac{di_e(x)}{dx} = \frac{i_e(\eta(x))}{l} \qquad --------(3)$$

$$i_n - i_{n-1} = i_{(n-1)}(\eta_{(n-1)})$$

$\eta_{(n-1)} = V_0 - \phi_{e(n-1)} =$ overpotential in (n-1)th layer

$i_{(n-1)}(\eta_{(n-1)}) =$ electrochemical current generated in (n-1)th layer

$$i_{(n-1)}(\eta_{(n-1)}) = -330{,}996 + 3{,}955\,\eta_{(n-1)} - 0{,}0169\,\eta^2_{(n-1)} + 2{,}99E-5\,\eta^3_{(n-1)} - 1{,}72E-8\,\eta^4_{(n-1)}$$

from Figure 3.8

Ohm's law in electrolyte phase

$$\frac{d\phi_e}{dx} = \rho_e i_e(x) \qquad --------(2)$$

$$\phi_{e(n)} - \phi_{e(n-1)} = R_e \sum_{n-1}^{n_{max}} i_{(n-1)}$$

$R_e =$ electrolyte resistance of one layer

$\sum_{n-1}^{n_{max}} i_{(n-1)} =$ *proton* current flowing through the (n-1)th layer

Boundary conditions :

$\eta_0 = V_0 =$ *overpotential* in first layer

The solution to this problem was calculated iteratively, starting from first layer for which the overpotential V_o is known. After adding next layer, current and overpotentials were then recalculated and corrected taking into account the current generated. After addition of each layer current and overpotential in every other layer has to be corrected iteratively so as to satisfy equation 2, 3 and boundary condition. A small C++ program used for this purpose is also added in this thesis (Appendix A1).

3.1.5 Checking validity of the solutions provided by CL model

The validity of the final solutions of $i_e(\eta(x))$, $\eta(x)$ and $\phi_e(x)$ can be checked by putting them into equation 2 and 3 and verifying if they satisfy these equations. For checking if the $i_e(\eta(x))$, $\eta(x)$ and $\phi_e(x)$ satisfy equation 2, one can compare $i_e(\eta(x))$ with the back calculated

$$i_e(\eta(x)) = \frac{1}{\rho_e}\frac{d\phi_e(x)}{dx}$$

which uses the $\phi_e(x)$ as the input. The following Figure 4.10 shows these two $i_e(\eta(x))$ along with $\phi_e(x)$. Both currents agree reasonably well. Data shown here is for a catalyst layer thickness of 180μm.

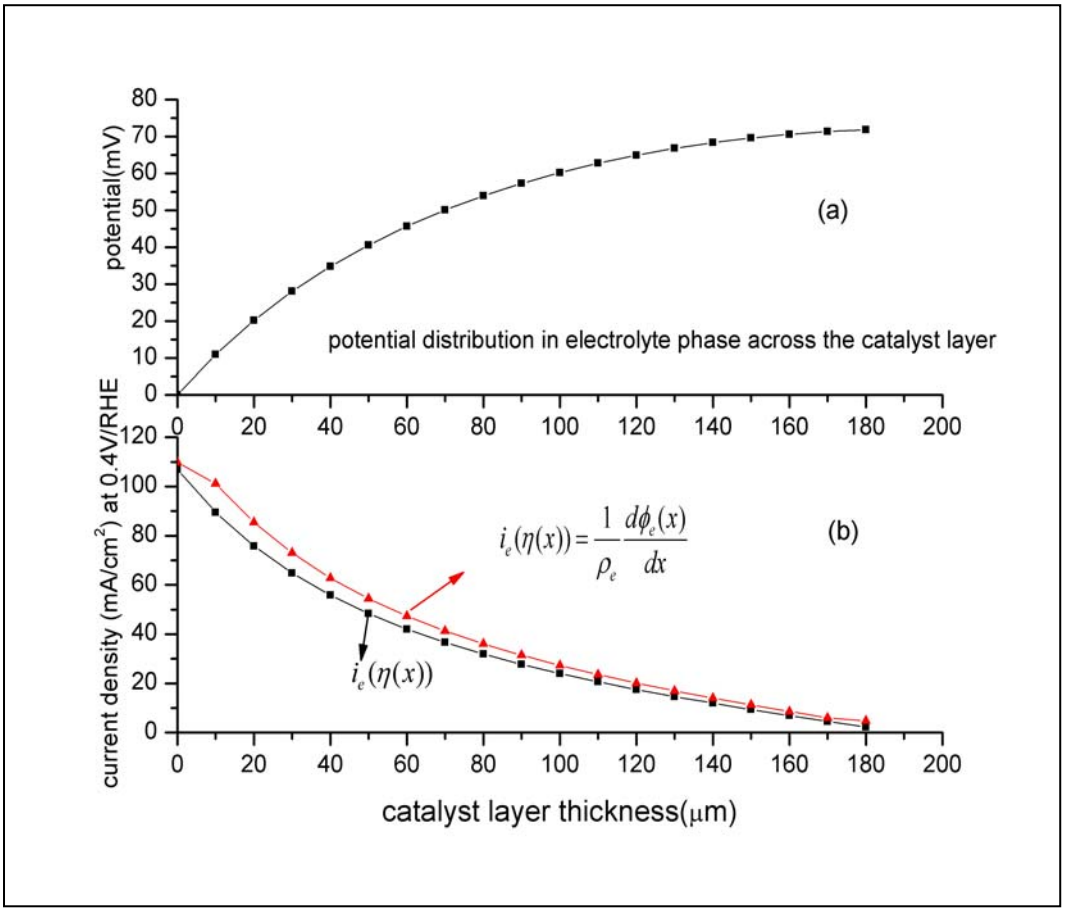

Figure 3.10. (a) The potential distribution in electrolyte phase across the thickness of catalyst layer (b) Comparison between simulated current profile and current profile back calculated using simulated potential profile as input.

Electrochemical current generation equation 3 also needs to be satisfied.

$$i_n - i_{n-1} = i_{(n-1)}(\eta_{(n-1)})$$

$$\eta_{(n-1)} = V_0 - \phi_{e(n-1)} = \text{overpotential in (n-1)th layer}$$

$$i_{(n-1)}(\eta_{(n-1)}) = \text{electrochemical current generated in (n-1)th layer}$$

$$i_{(n-1)}(\eta_{(n-1)}) = -330{,}996 + 3{,}955\,\eta_{(n-1)} - 0{,}0169\,\eta^2_{(n-1)} + 2{,}99\text{E}-5\,\eta^3_{(n-1)} - 1{,}72\text{E}-8\,\eta^4_{(n-1)}$$

$\phi_e(x)$ or its discrete version $\phi_{e(n-1)}$ can be again used in backcalculating $i_n(\eta_n)$. The following Figure 3.11 shows the $i_n(\eta_n)$ and back calculated $i_n(\eta_n)$ using $\phi_{e(n-1)}$.The agreement is good.

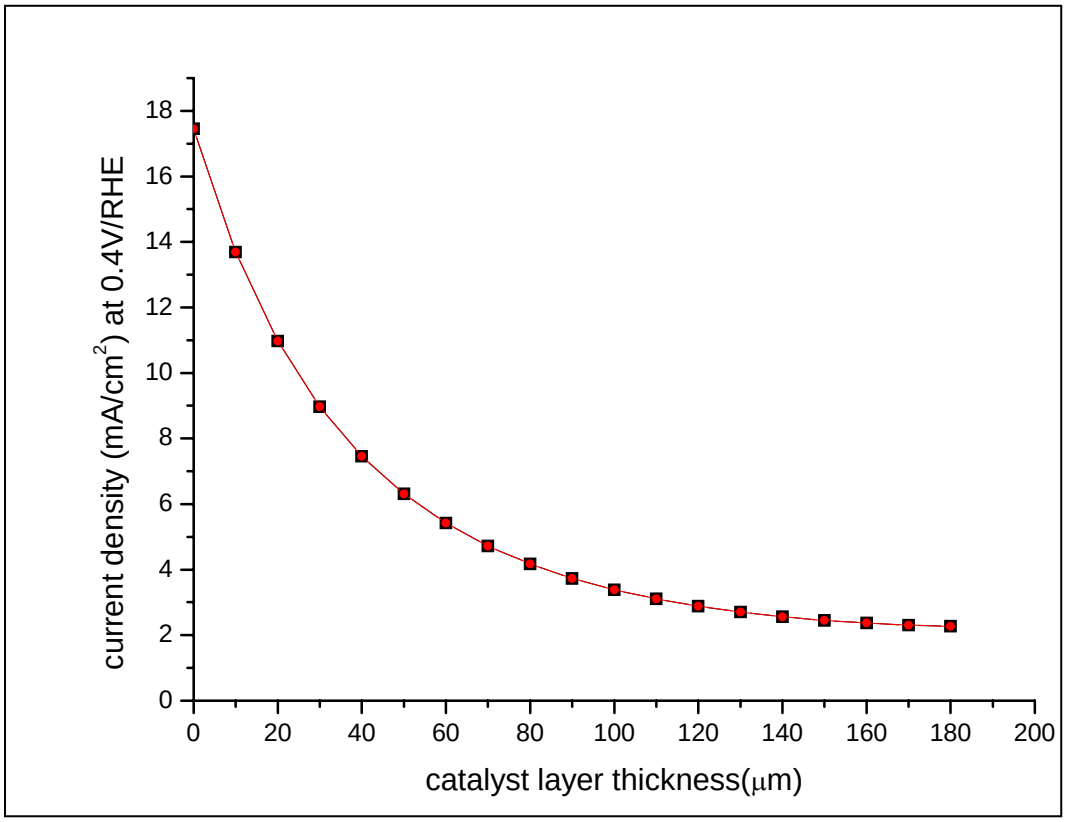

Figure 3.11. The electrochemical current generated in each thin catalyst layer is shown as function of their position in a 180μm thick catalyst layer.

3.1.6 Results obtained from catalyst layer model

Potential in the electronically conducting phase in CL remains same as the electronic conductivity is assumed to be very high. Figure 3.12 shows the overpotential profile for an applied potential of 0.4V in GDL. The thickness plotted is measured from the PEM side to GDL (Figure 3.12). The model calculation helped us in calculating the currents in half cell mode with various anode thicknesses of the CL at 0.4V. The Figure 3.13 shows the experimental data and also the calculated data which is calculated by only taking into account the effect of ohmic losses in electrolyte phase in CL. The calculated result although do not match the experimental results, but still clearly shows the "saturation effect" in current with increasing thickness of CL. This outcome agrees well with the results reported by Boyer et al[106] for cathode catalyst layer of a H_2/air fuel cell MEA. Their modeling studies showed that a cathode layer with 20% nafion by volume has a proton conductivity that limits the utilized active layer thickness to 20-25μm.

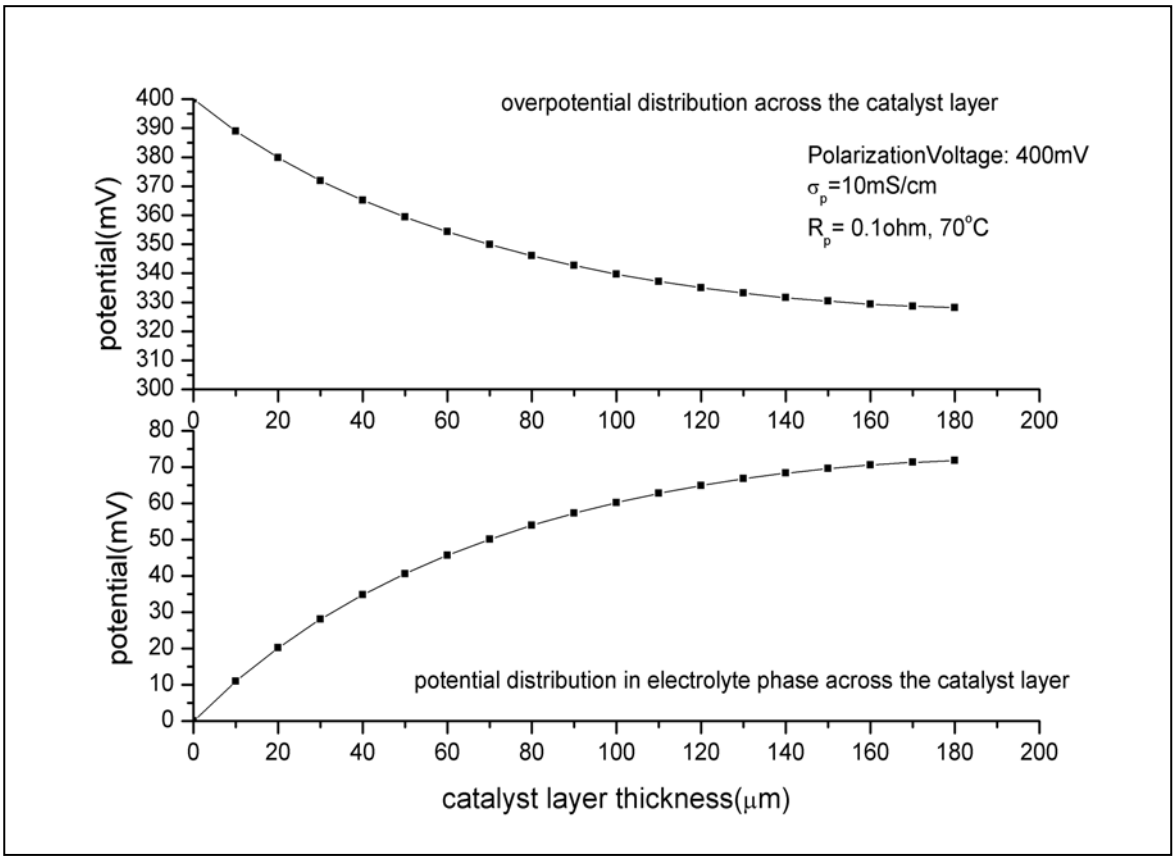

Figure 3.12. The overpotential distribution across the thickness of catalyst layer, if 400mV potential is applied at GDL.

Increasing the thickness further will offer only small increases in performance. Experimental data shows a "linear" increase in current density with increasing catalyst layer thickness or increasing catalyst loading in low current range (see Figure 3.4). The same effect is also seen with the model simulated current density in low current range. Figure 3.14 shows the simulated current density at a low polarization potential of 300mVs. In this simplified anode catalyst layer model, effect of parameters like mass-transport losses because of methanol and CO_2 diffusion, ohmic losses in electronically conducting phase were neglected. But still it is able to qualitatively match the experimental results. This might support the argument that the basic assumption of proton conductivity being most prominent parameter is correct. Any further consideration of effects like mass transport will only bring down the performance. So this model can at least predict the upper limit of the catalyst layer performance with particular proton conductivity.

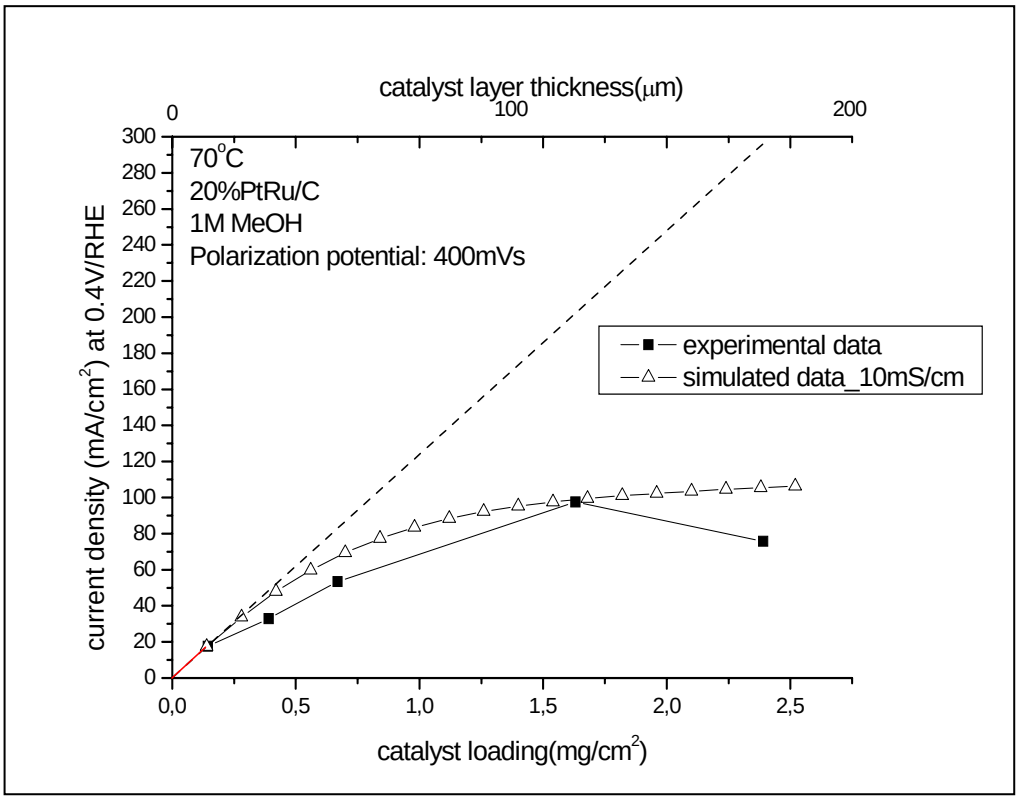

Figure 3.13. This figure shows calculated and the experimental data for current@ 0.4V potential versus the catalyst loading.

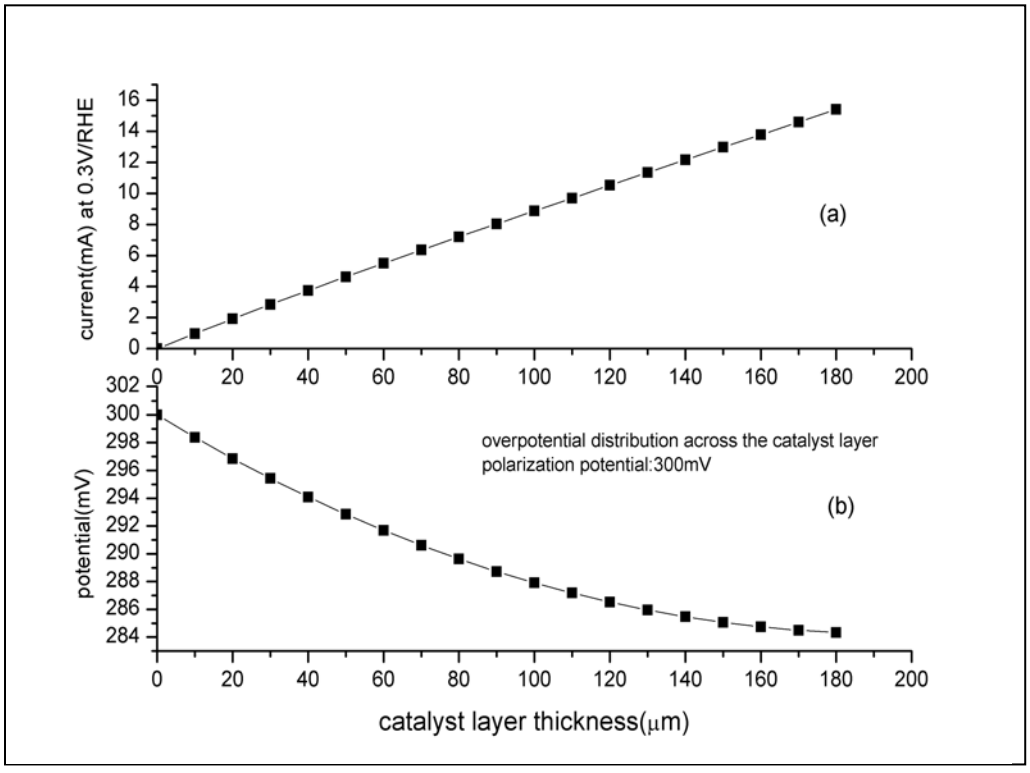

Figure 3.14. (a) This figure shows simulated data for current@ 0.3V potential versus the catalyst layer thickness. (b) overpotential distribution across the 180μm thick catalyst layer.

3.2 Measurement for activity of PtRu/Sibunit catalyst series

3.2.1 Experimental

3.2.1.1 Catalyst preparation

Carbons of the Sibunit family (*Omsk, Russia*) with different specific surface areas ranging from 6 to 415 m^2g^{-1} and Vulcan XC-72 (*Cabot Corp.*) were used as catalyst supports. PtRu (1:1) catalysts were prepared by co-hydrolysis of chloride complexes of Ru^{III} and Pt^{IV} using a procedure similar to that described by Reetz et al. [108] The authors of Ref. [108] found that an addition of alkali to a solution of $RuCl_3$+H_2PtCl_6 results in formation of small colloidal particles of mixed metal oxides, and added organic surfactants in order to prevent their further

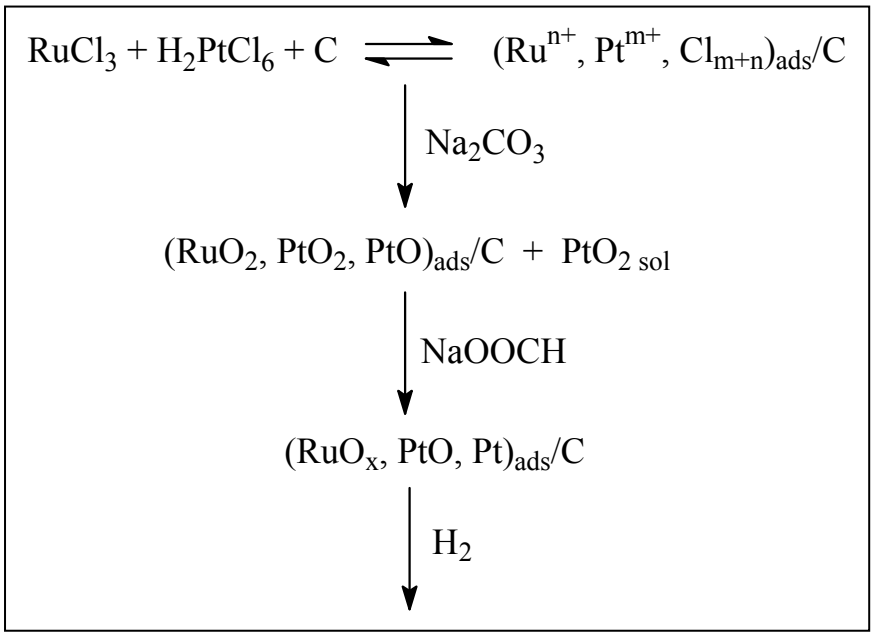

Figure 3.15. Schematic representation of the catalyst synthesis.

growth and coagulation. Unlike them, we avoided organic ligands (which form a shell around metal particles and may thus influence their activity in electrochemical processes), but performed synthesis in the presence of carbon supports, assuming that the latter may act as a macroligand stabilizing colloids of mixed metal oxides. The preparation procedure comprised a number of steps schematically represented in Figure 3.15.

3.2.1.2 Characterization of the sibunit carbon supports

Textural characteristics of carbon supports were obtained from the data on nitrogen adsorption measured at 77K with an automatic volumetric device ASAP 2400 (*Micromeritics*) and given in Table 3.1. Carbon samples were pre-treated at 573K to residual pressure of ca.

10^{-3} torr. The adsorption isotherms were used to calculate values of *BET* (Brunauer- Emmett-Teller) specific surface area S_{BET} (in the range P/P_0=0.05-0.2) and total pore volume V_Σ (at P/P_0=0.98). Here P_0 is the saturation pressure. The volume of micropores V_{mi} accessible to nitrogen at 77K and the total surface area of meso- and macropores A_α were determined using comparative method introduced by Karnaukhov et. al. [109]. The latter is analogous to α_s-method by Sing or *t*-method by Lippens - de Boer [109]. The volume *V* and the surface area *S* of the pores between 1.7 and 300 nm were calculated from the adsorption (BJHcum. ads. (Barrett-Joyner-Halenda)) and desorption (BJH cum. des.) branches of the capillary condensation hysteresis according to *BJH* model [110]. Values of mesopore diameters *D* were calculated on the basis of the *BET* and *BJH* models as $D = 4V/S$. Pore size distributions were acquired using BJH cum. desorption method and represented in Figure 3.16 for selected carbon samples.

Table 3.1. Textural characteristics of carbon materials.

Textural characteristics*	Vulcan XC-72	Sib_176K	Sib_P2677	Sib_111P	Sib_19P	Sib_20P	Sib_619P
Surface area, m^2g^{-1}							
S_{BET}	252	5.96	21.9	64.1	72.3	292	415
A_α	177	7.10	23.8	58.9	65.7	330	470
$S_{(BJH\ cum.\ ads.)}$	94	4.06	18.5	-	33.0	146	222
$S_{(BJH\ cum.\ des.)}$	103	4.10	22.1	38.2	46.9	239	351
Pore volume, cm^3g^{-1}							
V_Σ	0.63	0.018	0.117	0.105	0.154	0.416	0.593
$V_{(BJH\ cum.\ ads.)}$	0.547	0.016	0.114	-	0.132	0.325	0.470
$V_{(BJH\ cum.\ des.)}$	0.550	0.016	0.116	0.088	0.138	0.373	0.532
V_{mi}	0.037	0.000	0.000	0.0024	0.004	-0.012**	-0.019**
Pore size, nm							
$D_{(by\ BET)}$	7.5	11.8	21.4	6.5	8.5	5.7	5.7
$D_{(by\ BJH\ cum.\ ads.)}$	23.3	16.0	24.7	-	16.0	8.9	8.5
$D_{(by\ BJH\ cum.\ des.)}$	21.3	15.9	21.0	9.2	11.8	6.2	6.0

*See Experimental for details.

** Since V_{mi} is determined as an intercept of the t-plot, its negative values do not have physical meaning and point to the absence of micropores.

The X-ray diffraction (XRD) patterns of PtRu/C catalysts were obtained using X-ray diffractometer (*Siemens*, CuK_α radiation) featuring a high-temperature camera-reactor [111]. A catalyst sample taken from air was re-reduced in H_2 flow at 150°C for 1 hour, then cooled down to room temperature, then its X-ray diffraction pattern was recorded by scanning in the 2θ angle range from 20 to 100°. Calculation of the lattice parameter and the average size of metallic crystallites were based, respectively, on the angle position, and on the half-width of the 111 diffraction line for *fcc* structure. Metal dispersion in PtRu/C catalysts was calculated using data on pulse CO chemisorption in H_2 at 20°C, assuming that each Pt and Ru surface atom adsorbs one CO molecule.

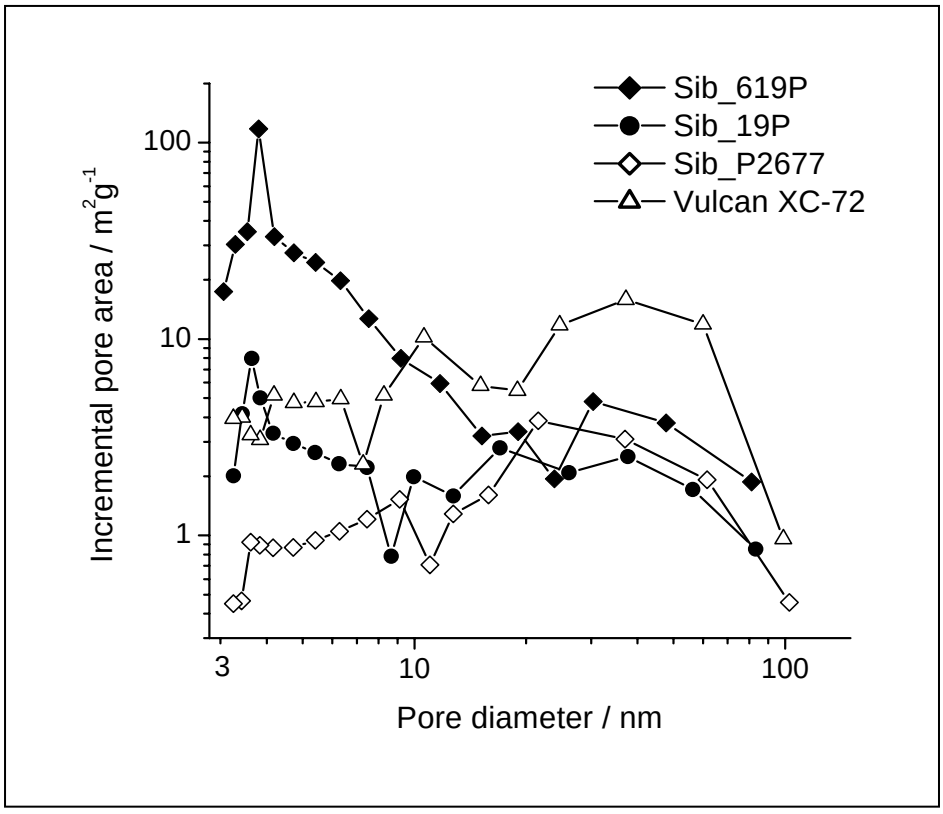

Figure 3.16. Pore size distributions from BJH desorption method.

Metal particle size distributions (PSD) were obtained from transmission electron microscopy

(TEM) images (*JEM-2010* microscope) and used to calculate average $\bar{d} = \frac{\sum_i n_i d_i}{\sum_i n_i}$, surface-average $d_s = \frac{\sum_i n_i d_i^3}{\sum_i n_i d_i^2}$, and mass average $d_v = \frac{\sum_i n_i d_i^4}{\sum_i n_i d_i^3}$ diameters of metal particles.

3.2.1.3 Electrochemical measurements

In order to keep the thickness of the anode electrocatalyst layer constant, the amount of catalyst powder (metal + carbon), is kept constant at nearly 1.5 mg cm^{-2} while spraying the anodes for all sibunit carbon supported catalysts. The anode with these catalyst loadings were then used to prepare the MEAs. After installing a MEA in a DMFC, cyclic voltammograms (CV) recorded in water flow did not show any features. However, during conditioning of the catalyst at 90^0C, anodic and cathodic peaks gradually developed at ca. 100 mV (see Figure 3.19) and after approximately 8 hours a stable CV was attained. Only after such a conditioning, the I-U curves and CO stripping voltammograms were recorded. The I-U curves for methanol oxidation were measured at a sweep rate of 0.5 $mV.s^{-1}$. It has been confirmed in special experiments that this sweep rate was sufficiently slow and gave rise to steady-state polarization curves.

3.2.2 Results and Discussion

3.2.2.1 Catalyst characterization

Data presented in Table 3.1 indicate that unlike Vulcan XC-72, Sibunit carbons do not contain micropores which are defined as pores < 2nm size (see V_{mi} in Table 3.1). This is also reflected in the close values of A_α and S_{BET} for Sibunit carbons, while for Vulcan XC-72 A_α is significantly lower than S_{BET}. Pores sizes from ca. 1 to 2 nm give noticeable contribution to the surface area of high surface area Sibunit carbons (samples 619P and 20P) as well as of Vulcan XC-72 as indicated by the difference between A_α and S_{BJH} values. Figure 3.16 shows that the decrease of specific surface area of Sibunit carbons from sample 619P to 20P, 19P and finally P2677 occurs at the expense of pores below 20 nm size, whose contribution drops, while the average contribution of macropores above 20 nm stays essentially unchanged. This is reflected also in an increase of the average pore size and a decrease in the volume of the pores (Table 3.1). CO chemisorption points to high metal dispersion in all PtRu/C catalysts under study, its values varying between 0.24 and 0.46 (Table 3.2). TEM images of selected catalysts shown in Figure 3.17a and 3.17b evidence that PtRu nanoparticles are separated and

uniformly distributed on support surfaces. Figure 3.17b demonstrates also "shell" morphology of high surface area Sibunit carbons, which results from total burn-off of primary carbon black globules during steam activation of Sibunit. Narrow particle size distributions are observed for catalysts supported on high as well as on low surface area Sibunit carbons (see inserts to Figure 3.17a and 3.17b).

Table 3.2. Dispersion and average metal particle size in PtRu/C catalysts.

Catalyst	Dispersion	Mean particle size, nm				
	CO/M	$d_{chem.}$	$\bar{d}$	d_n	d_s	d_m
1%PtRu/Sib_176K	0.42	2.4	1.8	1.9	1.9	1.9
10%PtRu/Sib_P2677	0.32	3.2				
10%PtRu/Sib_19P	0.36	2.8	2.6	2.8	3.0	3.1
20%PtRu/Vulcan XC-72*	0.40	2.5				
20%PtRu/Sib_19P	0.24	4.2	3.7	3.8	3.9	4.1
20%PtRu/Sib_20P	0.42	2.4				
20%PtRu/Sib_619P	0.46	2.2	2.0	2.1	2.1	2.2

* Non-uniform PtRu distribution: particles of 15-25 Å in diameter are predominantly observed, while some areas of the support surface are covered with large particles ca. 50 Å size.

This is demonstrated also by close $\bar{d}$, d_s and d_m values (Table 3.2). On the contrary, PtRu particles supported on Vulcan XC-72 shows bimodal particle size distribution, likely originating from the support inhomogeneity. Examination of extended support areas proves that predominant part of metal particles on Sibunit supports is not agglomerated. Comparison of CO chemisorption and TEM data leads to a conclusion that metal dispersion (CO/M) and surface-average size of the particles (d_s) obey the equation:

d_s (nm) ≈ 1/(CO/M)

Coefficient 1 in this equation is somewhat higher than that reported for pure ruthenium catalysts (d_s = 0.91/(CO/Ru) [112], but smaller than for platinum (d_s = 1.08/(CO/Pt) [113]. With the obtained formula we estimated an average particle size d_{chem} for PtRu/C catalysts using chemisorption data (Table 3.2). One may see that the preparation procedure employed in this study allows keeping the average particle within 2.2 and 4.2 nm despite considerable

variation (by a factor of 70) of S_{BET} of carbon supports.

XRD measurements were performed both in air and "*in situ*" in H_2-filled XRD chamber. Figure 3.18a compares XRD patterns acquired for 20%PtRu/Sib_619P sample stored in air and after its reduction "in situ" in a XRD chamber. The former hardly shows any metal reflections, indicating that PtRu particles are mostly oxidized under ambient atmosphere. The extent of metal oxidation depends critically on the dispersion of the metal particles, increasing with the increase of the latter. Oxidation of supported PtRu particles under ambient conditions has been reported earlier [61, 63, 114, 115]. As evidenced by Figure 3.18a, treatment of the catalyst samples in hydrogen atmosphere at 150°C, results in reduction of Pt and Ru. XRD patterns of reduced samples represented in Figure 3.18b do not show (101) Ru reflection at $2\theta = 44$, which confirms that Ru is not segregated in a separate phase and most of the metal is comprised in bimetallic alloy nanoparticles. Previously, it has been reported that interaction of oxygen with alloy RuPt or RuPd particles depletes them from Ru due to formation of ruthenium oxide phases. In the course the catalyst reduction with hydrogen, three scenarios have been observed: (i) Ru segregates into a separate phase and forms monometallic nanoparticles, (ii) Ru metal is segregated onto the surfaces of alloy particles [116], or (iii) bimetallic RuM alloy particles are formed [117].

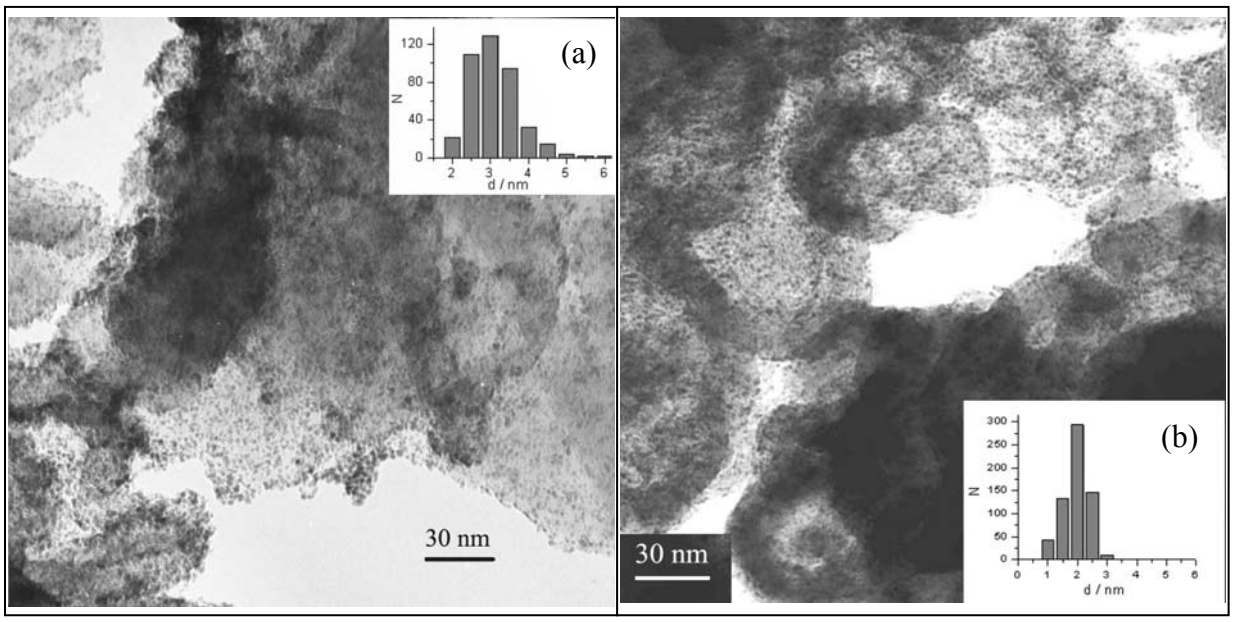

Figure 3.17. TEM images and particle size distributions for (a) PtRu/Sib_111P (S_{BET}=64.1 m^2g^{-1}) and (b) PtRu/Sib_619P (S_{BET}=415 m^2g^{-1}). Particle size distributions are shown in the insets.

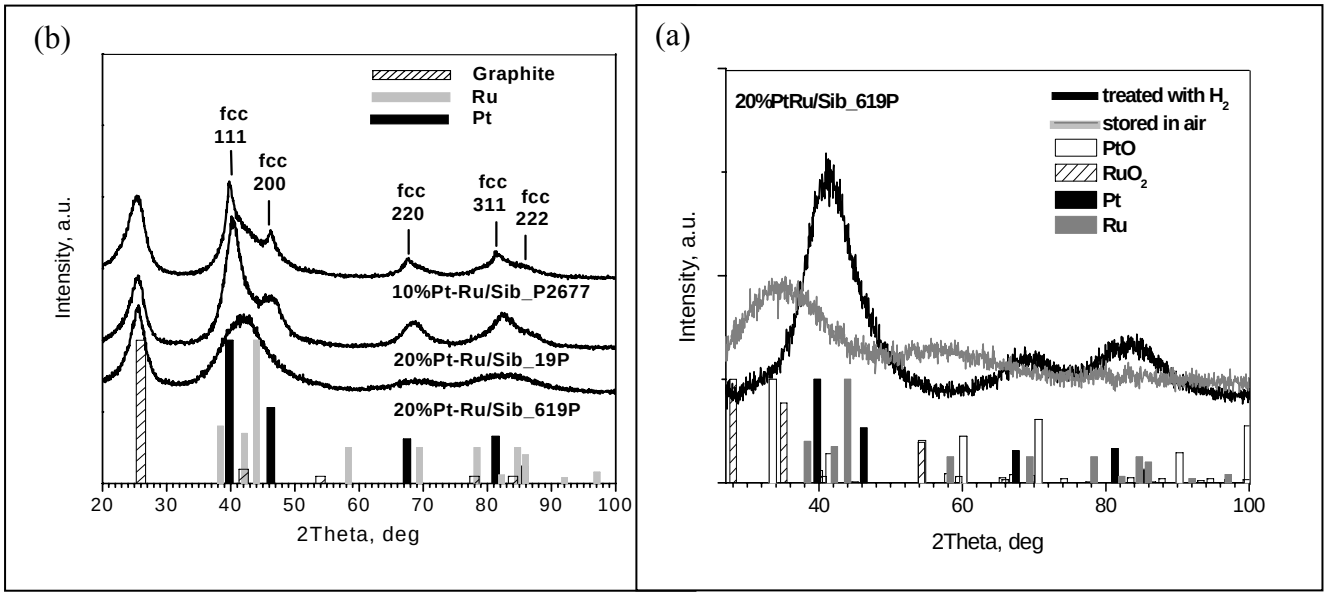

Figure 3.18. XRD patterns for PtRu/Sibunit catalysts: (a) 20%PtRu/Sib_619P stored in air and reduced in H_2 after subtraction of diffraction from the support; (b) 10%PtRu/Sib_P2677; 20%PtRu/Sib_19P and 20%PtRu/Sib_619P reduced in H_2. Bars show positions and intensities of the reflections corresponding to graphite, metallic Pt, Ru and their oxides.

In our case, obviously the latter scenario is realized, with reduction giving rise to alloy PtRu particles. This is confirmed both by the absence of separate reflections from Ru phase and by the value of the lattice parameter, which is equal to 3.88 Å for 20%PtRu/Sib_19P and 3.90 Å for 10%PtRu/Sib_2677P. It should be pointed out, however, that precise determination of diffraction line positions is not feasible due to (i) high metal dispersion, which stipulates line broadening and an overlap of (111) and (200) reflections from *fcc* PtRu nanoparticles, and (ii) superposition of (002) reflection from carbon support. 20%PtRu/Sib_619P catalyst represents the most dramatic example; where due to high metal dispersion (111) and (200) reflections merge together.

3.2.2.2 Optimization of the Nafion® content in MEAs

It has previously been reported that fuel cell performance may be noticeably influenced by the ionomer content in the catalyst layer [118-120]. Since specific surface areas of carbon supports utilized in this study are grossly different, a priori it was not clear which amount of

Table 3.3. Influence of Nafion® content on the mass activity* at 0.5V vs. RHE.

Nafion® content, wt.% / Catalyst sample	13	17	23	29	34
10% PtRu/Sib_P2677		268	190		29
10% PtRu /Sib_19P		272	257		
20% PtRu/Sib_19P	178	174			
20% PtRu/Vulcan XC-72		110		101	
20% PtRu/Sib_20P		130		119	

*Mass activity is given in $A.g^{-1}$ at $50^{o}C$ and 1M methanol feed, with DMFC in a half cell mode.

Nafion® ionomer is necessary to ensure high intra-layer ionic conductivity and optimum catalyst performance for each of these supports. Hence, in order to compare catalyst performance under optimized conditions, the amount of ionomer content in the catalyst layer was varied for each carbon support. The results are given in Table 3.3. Despite our expectations, the influence of ionomer content on the activity of PtRu/Sibunit catalysts in methanol oxidation is not very pronounced. Only at very high (50%) Nafion® content the activity of 10% PtRu/Sib_P2677 sample dropped noticeably, supposedly due to blocking metal particles and hindering methanol diffusion to and CO_2 diffusion from their surfaces. The optimum amount of ionomer was close to 17wt% of dry Nafion® in the anode layer for all the catalysts explored and was further on used for all MEA preparation. An independence of the optimum Nafion® content on S_{BET} in a wide interval from 22 to 416 m^2g^{-1} can be explained by pore size distributions in Sibunit carbons (Figure 3.2). As mentioned above, an increase of Sibunit surface area occurs mainly due to an increase of the amount of pores below 20 nm in size. Since according to Uchida et al [53, 59], Nafion® micelles penetrate mainly in macropores (>40 nm diameter), smaller pores, which develop upon an increase of the surface area of Sibunit carbons, do not demand more Nafion®. Arico et. al. [120] have also observed little influence of Nafion® content in the Vulcan XC-72 supported PtRu anode catalyst layer on the performance of DMFCs. They have found ca. 15% increase in the cell

performance, when the amount of Nafion® was raised from 15% to 33%. Meanwhile, our experiments reveal 10% decrease in mass activity, when Nafion® content increased from 17 to 29% (Table 3.3). It should be noted that the optimum Nafion® amount may depend on the carbon support structure, the metal loading, etc. Thus, Sasikumar et al. [119] reported best PEMFC performances at Nafion® contents of 20, 40 and 50 wt.% for platinum loadings of 0.5, 0.25 and 0.1 mg(Pt)cm^{-2}, respectively.

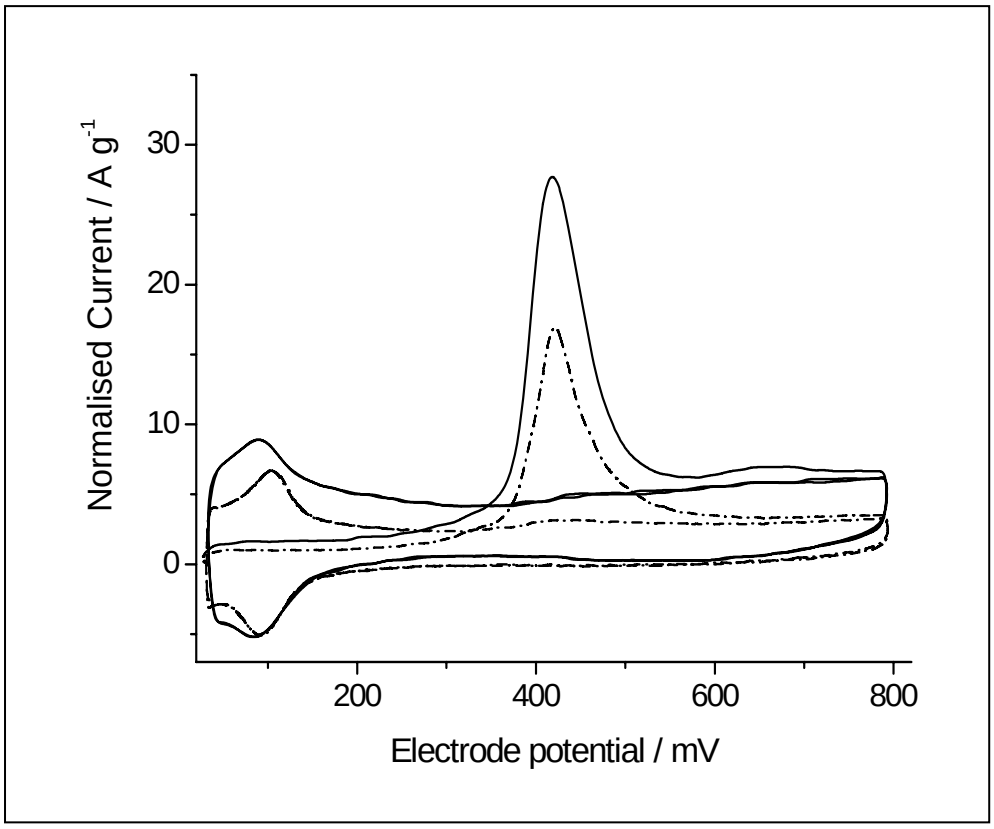

Figure 3.19. Typical CO stripping voltammograms at 50°C and 5 mVs^{-1} scan rate, measured in half-cell DMFC. Y-axis shows current normalized to metal loading. X-axis is the potential vs. RHE. Solid line corresponds to 10%PtRu/Sib_P2677 (0.15mg/cm^2 PtRu loading) and dotted line to 20%PtRu/Vulcan XC-72 (0.3mg/cm^2 PtRu loading).

3.2.2.3 Metal utilization in PtRu/C electrocatalysts

The metal utilization α in electrocatalysts is calculated as a ratio of the electrochemically active surface area (EASA) and the total metal surface area (TSA). The latter is derived from the amount of CO chemisorbed from the gas phase (N_{CO}^{Chem}), while the former is determined from the amount of electrochemically stripped CO (N_{CO}^{Echem}). Finally, α is calculated using the formula:

$$\alpha = \frac{EASA}{TSA} = \frac{N_{CO}^{Echem}}{N_{CO}^{Chem}} = \frac{Q}{2FN_{CO}^{Chem}}$$

Here Q is the CO stripping charge, and F is the Faraday constant.

Typical CO stripping voltammograms are shown in Figure 3.19 for 10%PtRu/Sib_P2677 and for 20%PtRu/Vulcan XC-72 catalysts. The stripping charge Q is calculated as the area under CO stripping peak versus the background (second scan) in 0.35 to 0.8 V potential range. EASA is then calculated assuming 385 μC cm^{-2} [121]. In Figure 3.20 α is plotted versus S_{BET} of carbon supports. The figure clearly shows that the catalyst utilization factor rises along with the decrease of S_{BET}. For PtRu/Vulcan XC-72 (S_{BET} = 252 m^2g^{-1}), α amounts to 50-55%, which agrees well with the data reported in the literature [4, 122]. For Sibunit 19P (S_{BET} = 72 m^2g^{-1}) α exceeds 1, which may be either due to the experimental uncertainty, or to a systematic error arising from an overestimation of CO stripping charge Q. Thus, according to Jusys et al.[99], contribution of the double layer charge to Q for PtRu surfaces may amount to 50%. If this is really so, values of α calculated in this work will be systematically overestimated for all the catalyst samples. This, however, will not change the observed trend of the increase of α with S_{BET}.

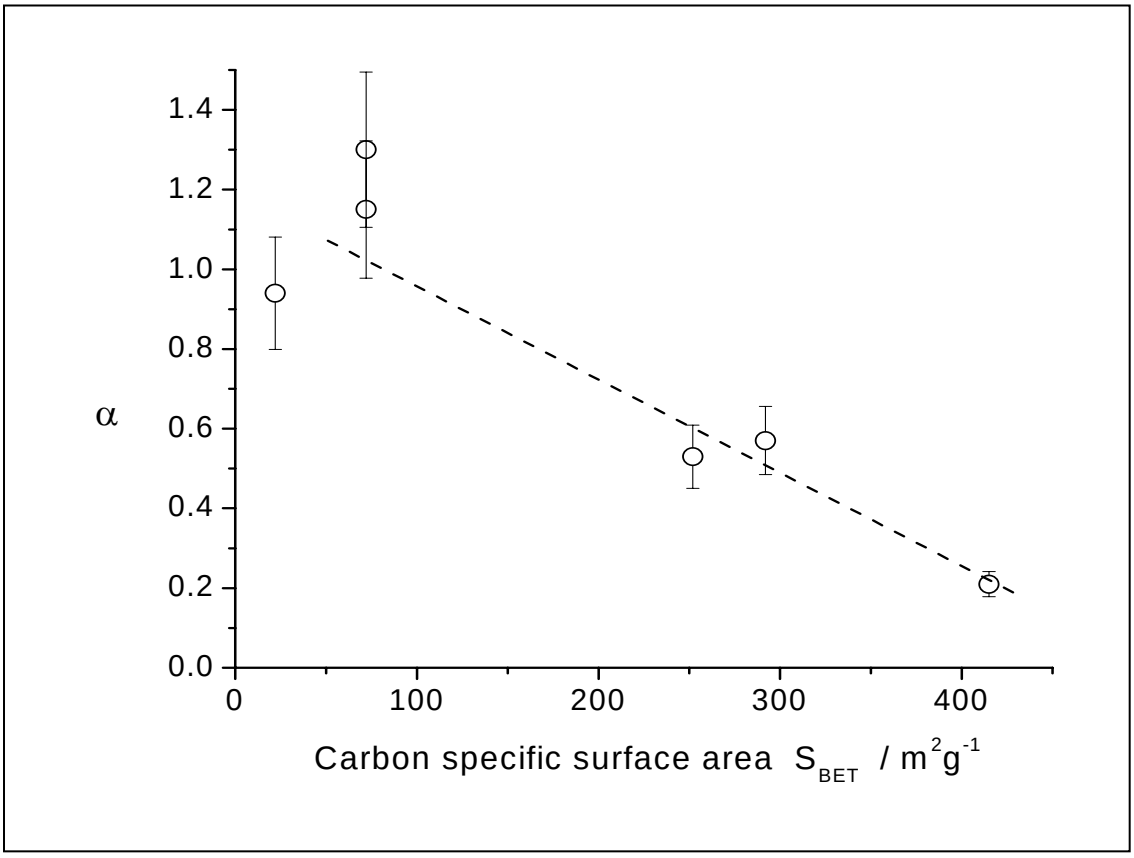

Figure 3.20. Catalyst utilization factor α plotted vs. S_{BET} of carbon supports.

The trend of decreasing metal utilization with an increasing support surface area can be explained on the basis of an increased incompatibility between the morphological structure of carbon support and Nafion® micelles. In CO chemisorption all the metal sites, which are exposed to the surface of nanoparticles and adsorb CO, are counted, since CO gas can reach every nanoparticle regardless its location (unless its surface is blocked by the pore walls or carbonaceous deposits [123]. However, this is not the case in an electrochemical CO stripping experiment from a PtRu/C catalyst incorporated in a MEA. The latter provides information only on the amount of PtRu sites, which are in contact with the Nafion® ionomer and thus can participate in the electrochemical process. As the surface area of carbon supports increases, more small pores with d <20 nm are formed (Figure 3.16). Meanwhile, according to Refs. [53, 59], Nafion® ionomer has rather large (>40nm) micelles, which do not penetrate in carbon pores of smaller diameter. The results of this work strongly suggest that an increase of the contribution of pores with d<20 nm results in a considerable decrease of the metal utilization factor (cf. Figure 3.20 and 3.16), thus providing a qualitative support for the data reported by Uchida et al. [59]. Thus, low surface area carbon materials, featuring minimum (if at all) contribution of pores below 20 nm, favor high catalyst utilization in MEAs of fuel cells with polymer electrolyte.

3.2.2.4 Methanol oxidation

Figure 3.21 shows current potential characteristics for PtRu catalysts supported on Sibunit and on Vulcan XC-72 in 1 M methanol. The most remarkable observation is that the catalysts supported on low surface area carbons (Sib_19P with S_{BET} = 72 m^2g^{-1} and Sib_P2677 with S_{BET} = 22 m^2g^{-1}) show much superior mass activities. Vulcan XC-72 based catalysts (both homemade as well as commercial) show much lower mass activities. PtRu/Sib_619P catalyst, which support has very high surface area of 415 m^2g^{-1} reveals the poorest performance. Surprisingly, the I-U curve for the 1%PtRu/Sib_176K catalyst with an extremely low carbon surface area of only 6 m^2g^{-1} and low metal content lies much above that for 20%PtRu/Sib_619P and at high overpotentials approaches that for 20%PtRu/Vulcan XC-72 catalysts.

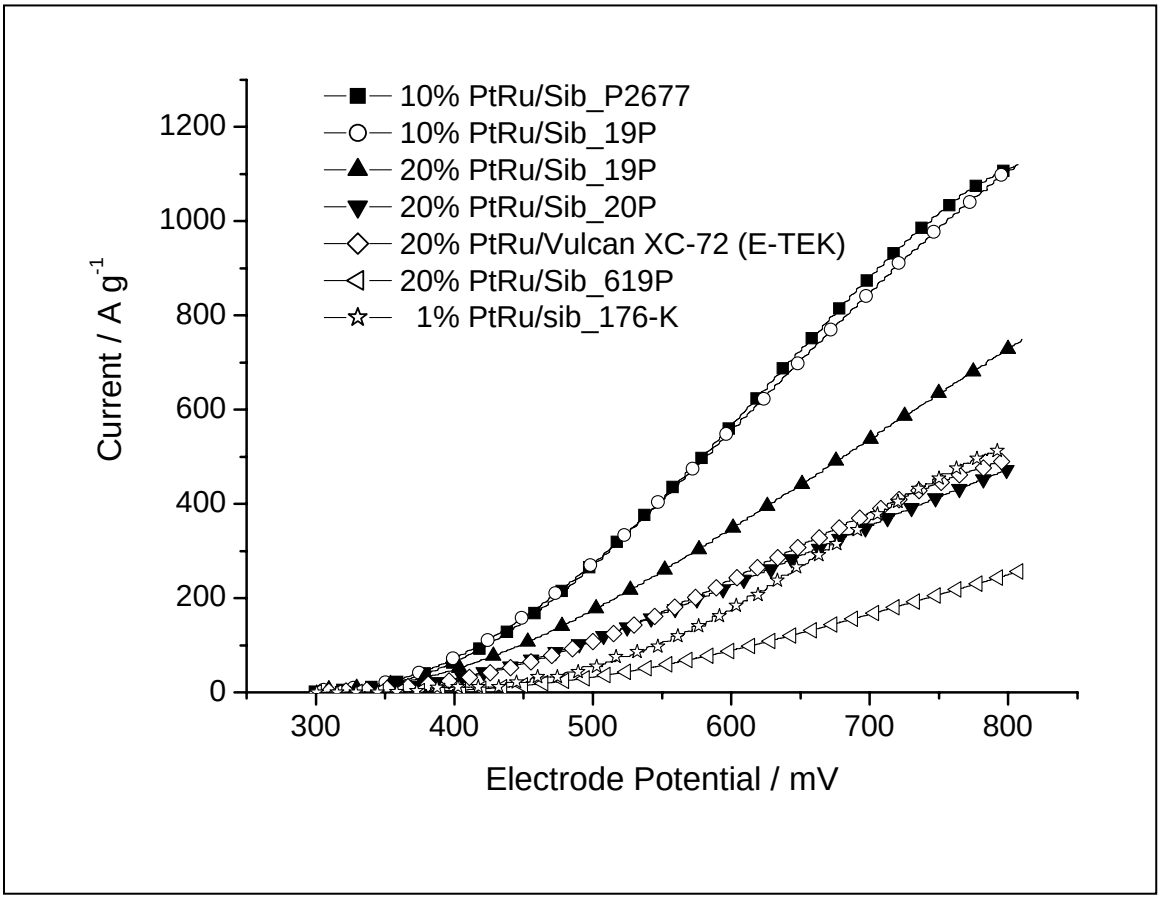

Figure 3.21. Current-Potential characteristics for PtRu anode catalysts at 50°C and 0.5 mVs^{-1} scan rate, measured in half-cell DMFC. Y-axis shows current normalized to metal loading.

Although high overpotential interval is of limited interest for fuel cell applications, the behavior demonstrated by carbon material, containing grains with essentially geometric surface area (nearly no porosity) is interesting and deserves further exploration. The difference in mass activities between 10% and 20% catalyst supported on Sib_19P may be tentatively ascribed to different dispersions of PtRu particles (Table 3.2). Mass activities of the catalysts at 0.5 V are plotted in Figure 3.22 and show clear dependence on the S_{BET} of carbon supports. Mass activities increase systematically, as S_{BET} is reduced from 415 to 72 m^2g^{-1}. Sib_19P and Sib_P2677 supported samples demonstrate the highest mass activities, which are nearly 3 times higher compared to Vulcan XC-72.

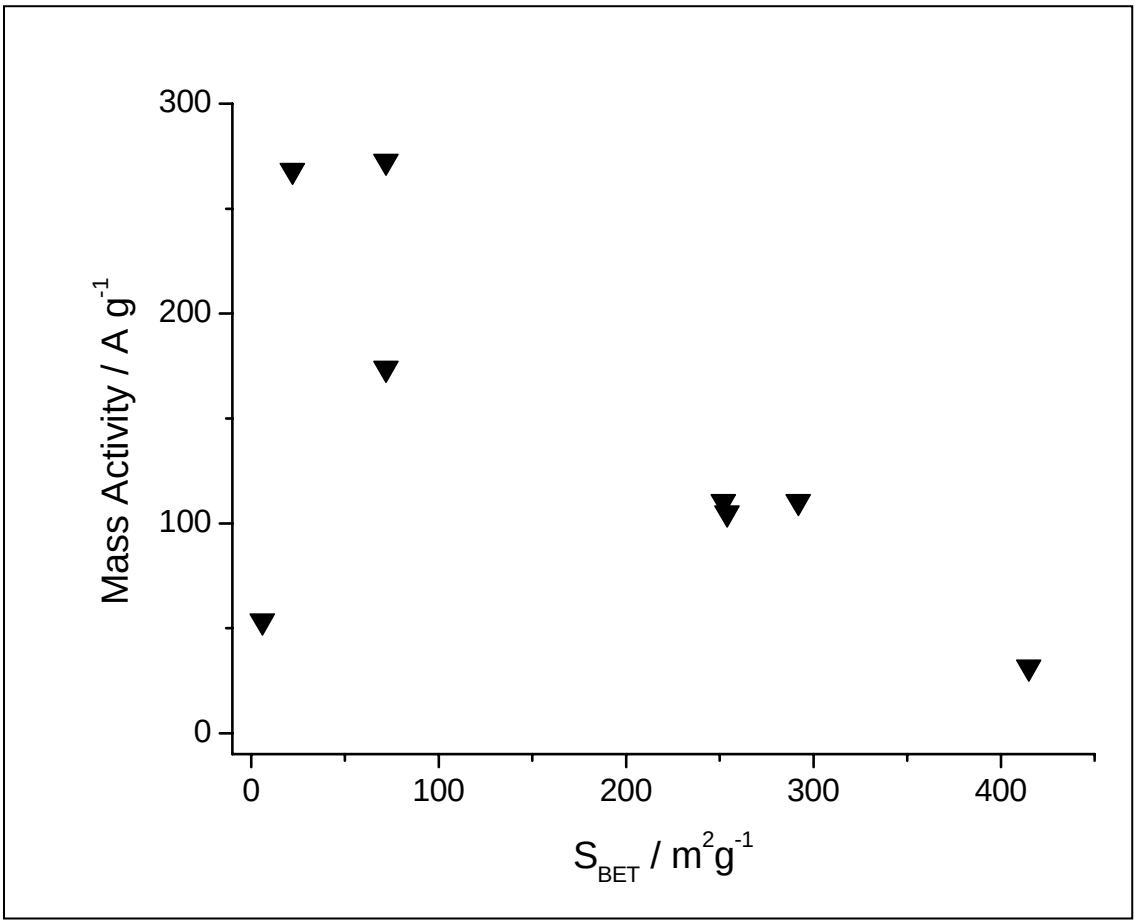

Figure 3.22. Mass activities at 0.5V RHE plotted versus S_{BET} of carbon supports.

It should be stressed that this effect indeed arises from different pore structures of carbon materials, rather than from (i) different catalyst preparation procedures or (ii) different metal particle dispersions. Indeed, Table 3.2 proves that metal dispersion for 20%PtRu/Vulcan XC-72 and 10%PtRu/Sib_19P is very similar (0.4 and 0.36, respectively), while the difference in mass activities amounts to a factor of 3. The preparation procedure cannot explain the observed current enhancement either, as illustrated by the observed coincidence of the I-U curves for the commercial catalyst and the homemade 20%PtRu/Sib_20P, the latter having very similar to Vulcan XC-72 specific surface area (292 m^2g^{-1}). The reason of low mass activity of the catalyst supported on Sib_176K with S_{BET}=6 m^2g^{-1} is not quite clear yet. Either catalytic activity shows an optimum vs. S_{BET} between 20 and 70 m^2g^{-1}, or the observed decrease of the catalytic activity results from the low (1wt.%) metal content in the sample. At such a low metal content even small amounts of impurities in the catalyst layer may be detrimental for the catalytic activity. Superior performance of low surface area carbons with

S_{BET} between 20 and 70 m^2g^{-1} was not unexpected, since we believe that utilization of high

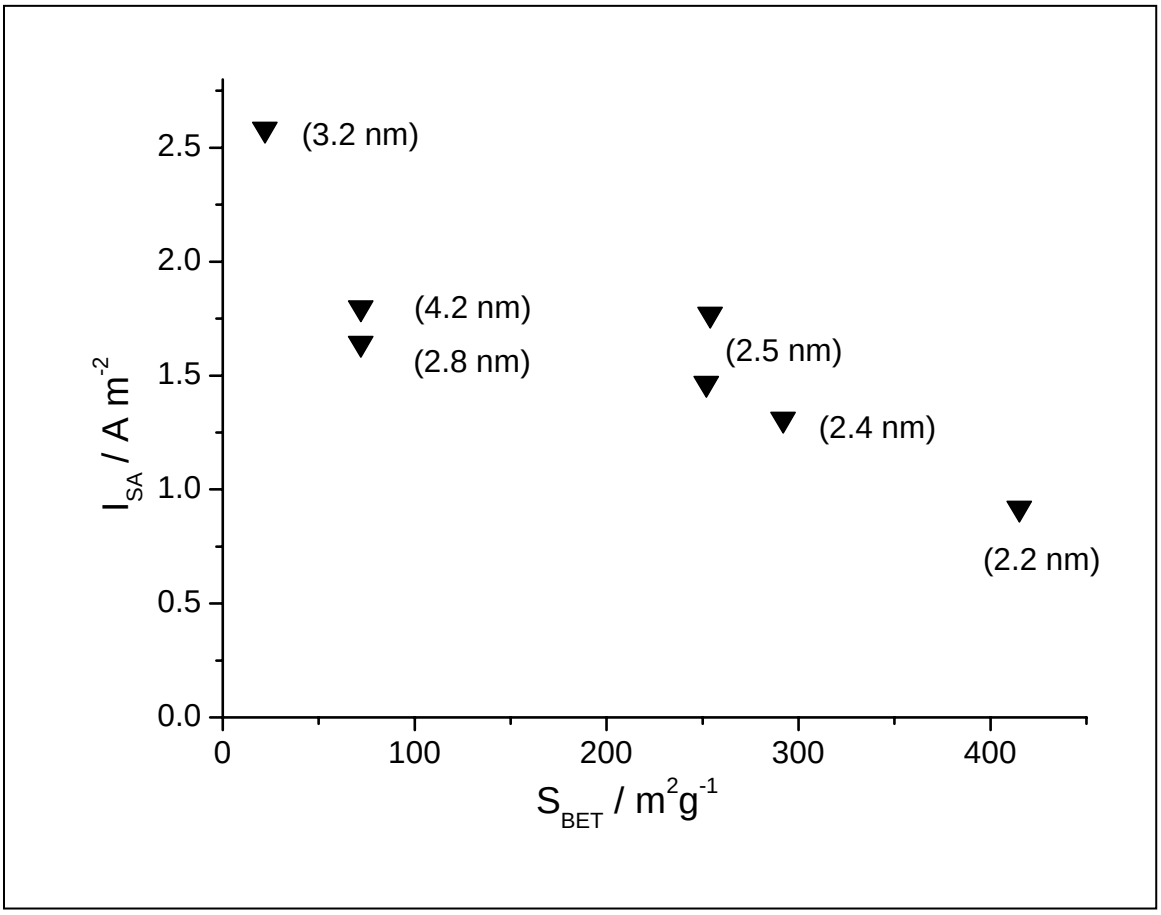

Figure 3.23. Specific activities ($A.m^{-2}$) at 0.5V RHE plotted versus S_{BET} of carbon supports. Unfortunately, due to experimental problems, data on EASA and hence specific activity of Sib_176K (6 m^2g^{-1}) are not available.

surface area supports in PEMFCs and DMFCs leads to two disadvantages: (i) low metal utilization and (ii) diffusion hindrance in narrow pores. While the influence of the metal utilization on the catalyst performance was discussed above, the issue of diffusion hindrance in the pores needs further clarification. Therefore, we normalize anodic currents to EASA (electrochemical active surface area) and obtain specific activity values (Am^{-2}), which are plotted in Figure 3.23 for the anode potential of 0.5 V versus S_{BET}. If the differences in the metal utilization were the only reason for the observed mass activity enhancement, the values of specific catalyst activities per unit of EASA should have been independent of S_{BET}. On the contrary, a clear trend of specific activity enhancement is observed, when carbon surface area is reduced from 415 to 22 m^2g^{-1}.

Since despite our efforts, metal dispersion in the catalysts under study was not exactly the same, let us analyze whether the differences in specific activities might originate from different PtRu dispersions. For clarity, we indicate the average PtRu particle sizes measured by gas phase CO chemisorption in Figure 3.23. Obviously, the differences observed cannot be attributed to the influence of dispersion alone. As mentioned in the introduction, Takasu et al. [52] reported remarkable size effect for Vulcan XC-72 supported PtRu nanoparticles during methanol oxidation. They have observed a considerable decrease of specific activity per unit surface area, when the average particle size decreased below 3 nm. In our case, size effects are obviously much less pronounced as illustrated by the close values of specific activities for 2.8 and 4.2 nm PtRu particles supported on Sib_19P. One should however bear in mind that Takasu et al tested their catalysts in sulfuric acid, and not incorporated in MEAs with a polymer electrolyte, as in this work.

Comparison of Figures 3.23 and 3.16 demonstrates clear correlation between the values of specific activity of PtRu methanol oxidation catalysts and the contribution of pores with d<20 nm: the higher their contribution, the lower the activity. Indeed, Sib_P2677, which shows superior specific activity, features a very small amount of pores with d< 20 nm (Figure 3.16). As S_{BET} increases, the contribution of the pores below 20 nm to the support surface area gradually increases, while specific activity decays. Hence, the results of this work strongly suggest that utilization of lower surface area carbons with larger pores relaxes diffusion hindrance inside the pores. It is not quite clear yet either the effect observed is due to slow methanol (or its oxidation products) diffusion or due to blocking the pore mouths by Nafion® micelles.

3.2.2.5 Mass activity at higher catalyst loading(>0.3mg/cm^2)

The metal catalyst loading in the anode catalyst layers used in this study are below 0.3mg/cm^2. As has been mentioned in the experimental section the overall catalyst loading (metal+carbon) is kept low, at around 1.5mg/cm^2 to avoid problems which comes into play at higher catalyst layer thicknesses. To understand the influence of the increasing catalyst layer thickness on the methanol oxidation current density, half-cell methanol oxidation experiments were performed with increasing catalyst loading for 20%PtRu/Vulcan commercial catalyst.

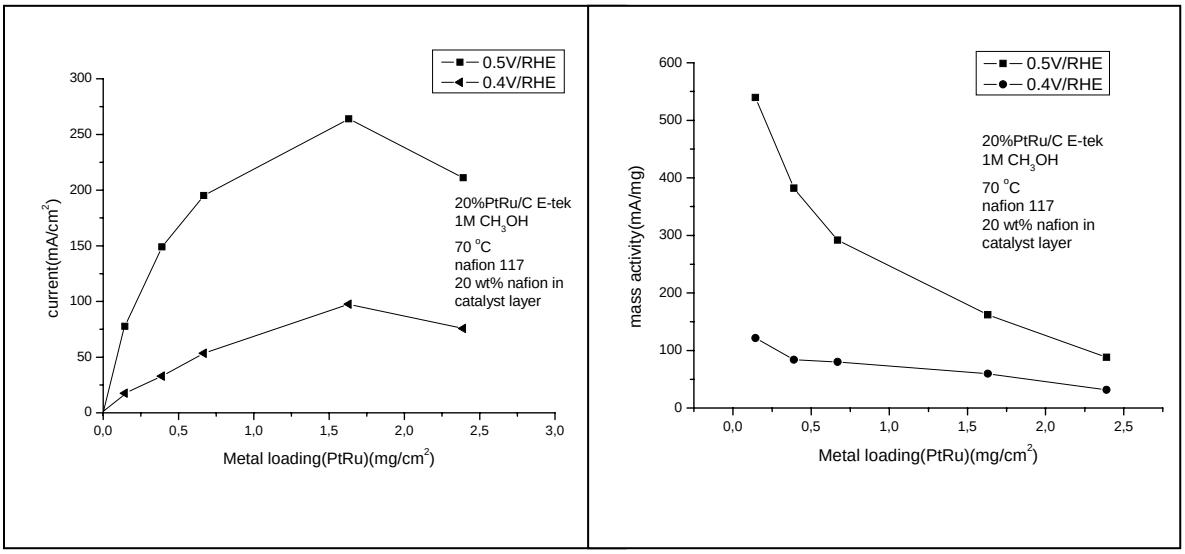

Figure 3.24. (a) This graph shows the methanol oxidation current density at 0.5 and 0.4V/RHE in a half-cell as a function of catalyst loading. (b) Corresponding mass activity at 0.5 and 0.4V/RHE as a function of catalyst loading.

At a particular polarization potential, in lower catalyst loading range, the methanol oxidation current density increases linearly with increasing catalyst loading. But the current density saturates to certain value at higher catalyst loading as can be seen in Figure 3.24(a). Figure 3.24(b) shows the variation of mass activity as function of catalyst loading. As expected the mass activity is highest at the lowest loading and it decreases rapidly with increasing catalyst loading. At higher catalyst loadings and thus also higher catalyst layer thicknesses, the positive effect of higher intrinsic activity of the supported catalyst is overshadowed by the strong negative effects associated with the thick catalyst layer. Supported catalysts with higher metal% on carbon (e.g. 50-80%PtRu/C), would behave better at higher metal catalyst loadings as the catalyst layer thickness is relatively lower. K.A. Friedrich et al.[124] compared the mass activity of the catalysts with varying metal% on carbon from 10 - 80%PtRu/C, in a loading range of 2.0mg/cm^2 and reported that 10%PtRu/C is the least active catalyst. This result is easily understandable when we take into account the results of Figure 3.24(b). But as has been discussed earlier the low mass activity at higher catalyst loadings for the low metal% (10-20%PtRu/C) catalysts is because of strongly negative effects of high catalyst layer thicknesses. Mass activity in thin catalyst layers for the same catalyst in much higher, as can be seen in Figure 3.24(b).

3.2.2.6 Oxygen reduction

The same batch of catalyst was also investigated for oxygen reduction reaction. Although PtRu/C is not the catalyst optimized for O_2 reduction reaction (ORR), as pure Pt based catalyst are known to be standard catalysts for ORR. But Ru itself is known to be active for ORR although is not stable at typical potentials of ORR. So Ru component of the catalyst can at most be oxidized to completely amorphous RuO_2, which may act as an insulator. Since the atomic percentage of Ru is same in all catalysts at around 50%, we can argue that measuring the ORR activity for this batch of catalysts could still give important information about the impact of carbon support surface area on the ORR rates. These experiments were performed to look for any effect of carbon support S_{BET} on the mass activity of the catalysts towards O_2 reduction. High Pt (3-4mg/cm^2, 40% Pt/C) loaded electrode with continuous flowing (100 sccm) hydrogen at 1 bar overpressure was used as a dynamic hydrogen reference electrode (DHE). Cathode was kept at 1bar overpressure also. All potentials in ORR results are reported with respect to this reference. MEAs were prepared by hot pressing method. Catalyst powders sprayed on TGPH060 (no wet proofing, 0.17mm thick) of 1.2 cm^2 area were hotpressed with nafion 1135 membrane, at 140 ^{o}C and 826N/cm^2 pressure.

Humidification and reproducibility problems

Since all experiments were performed in gas phase, humidity fluctuations because of cathode flooding and fluctuation in hydration levels of the membrane are major factors responsible for instability in the I-U curves. This problem was overcome by using low temperature (28 ^{o}C) for all measurements and humidifying H_2 and O_2 at 45 ^{o}C. Under these conditions it was possible to get reproducible I-U data. Every sample was examined for a period of 3-4 days. At 28 ^{o}C the membrane resistance or the hydration levels of the nafion membrane do not change much, but another not so harmful phenomena happening is electrode flooding. It was seen several times but after heating the cell by 6-7 degrees and with higher flow rate this sample current levels were restored again to previous levels. So this was perfectly reversible. To demonstrate how flooding show up in I-U curves, Figure 3.25 provides a good example.

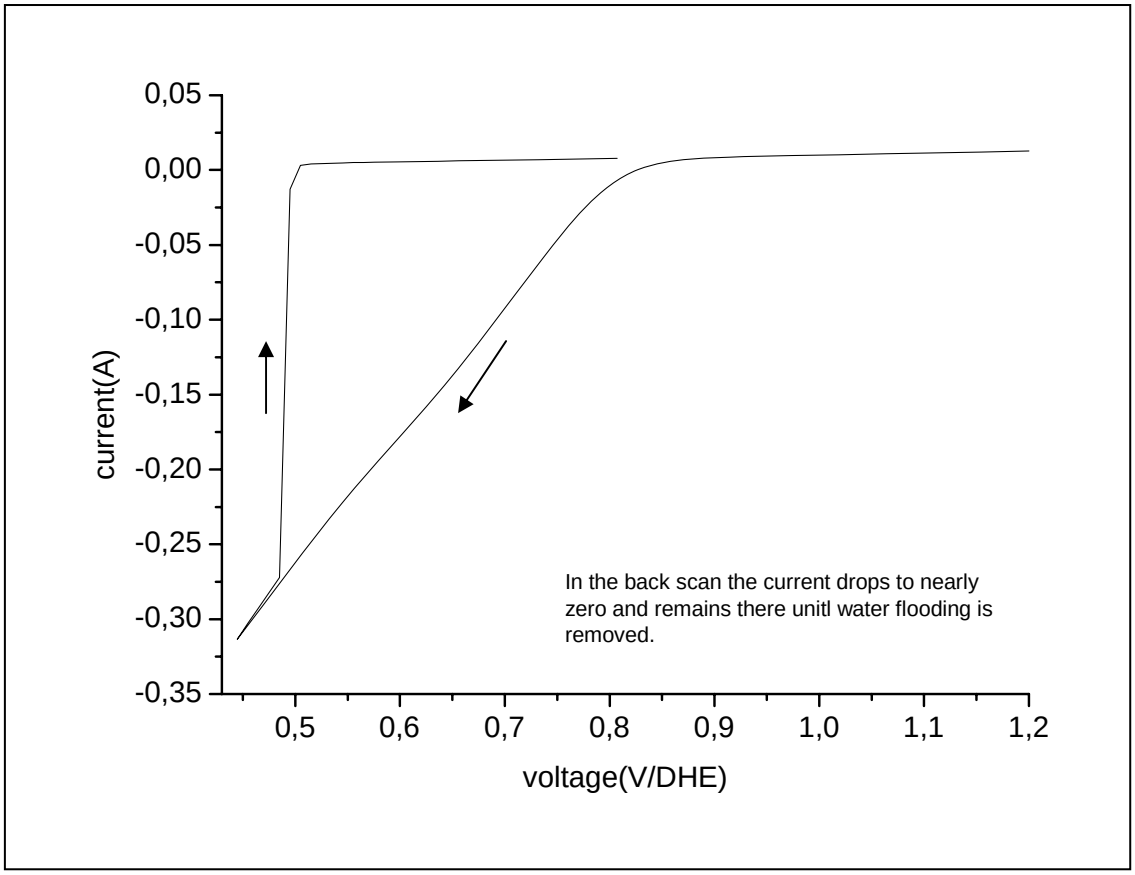

Figure 3.25. Current density drops to zero because of cathode flooding.

Figure 3.25 shows a CV with a 0.5mV/s scan rate. In the backward scan the current drops almost to zero. The transition from a good functioning electrode to a flooded electrode is not gradual but surprisingly abrupt. It seems that either the GDL or catalyst layer or both gets covered and flooded with a condensed water layer which obstructs the diffusion of oxygen to the catalyst particles. Figure 3.26 shows a CV with flooded cathode. The current do not change with potential beyond 10-15 mA. This is the mass transport limited current as the diffusion coefficient and solubility of O_2 in water is very small. After heating the cell to 35 ^oC and purging it with high flows, the current levels again recover back to normal. At higher potentials >0.85V, small positive current is observed. This current might result from the oxidation of crossed-over hydrogen. In this potential range the overpotential for hydrogen oxidation is very high, but overpotential for oxygen reduction is not high enough. So the positive current from crossed over H_2 will dominate.

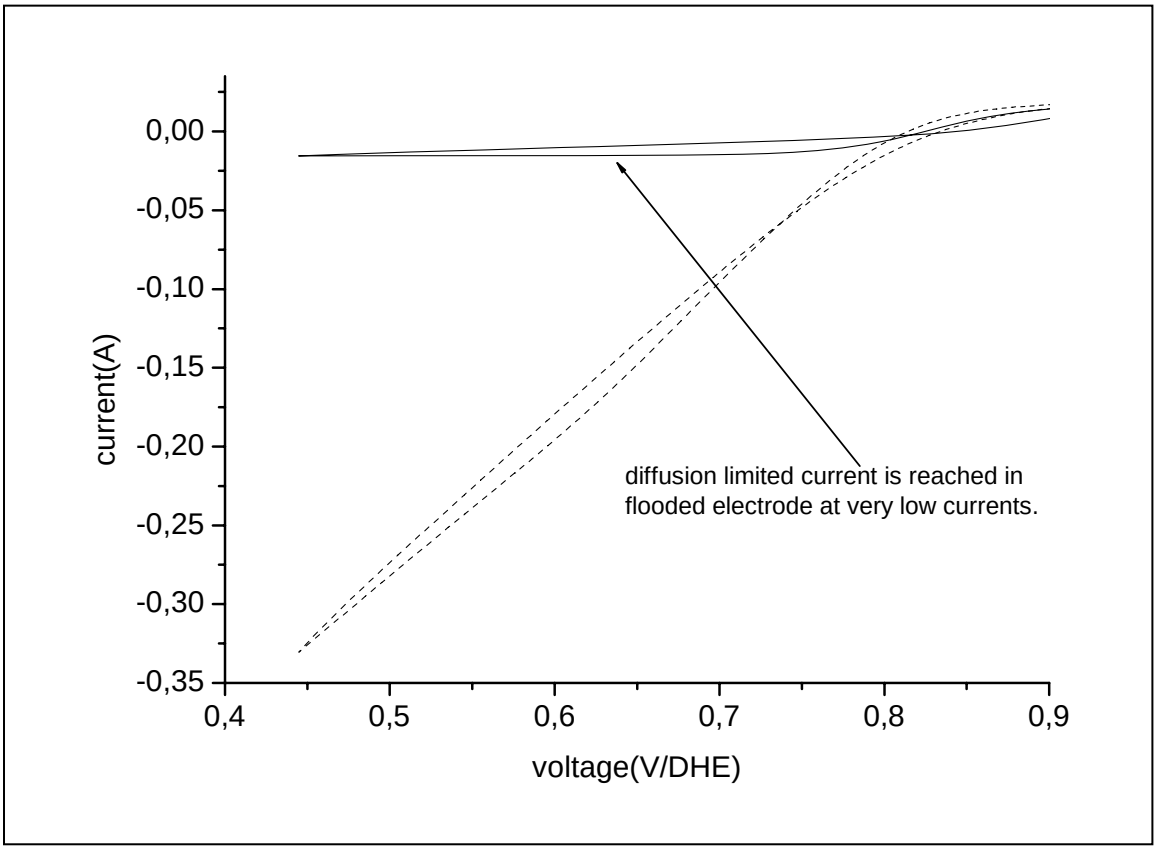

Figure 3.26. Cyclic voltammogram shows a diffusion limited current plateau.

Although it is possible to achieve stable I-U data at high temperature with the help of special GDLs with microporous layers and various degrees of teflonization, but since the electrodes were already sprayed onto TGPH060 (no wet proofing), it was not possible to change to another well-optimized GDL.

Figure 3.27 shows the mass normalized currents vs. voltage (DHE), for different catalysts, all with nafion percentage of 17wt%.

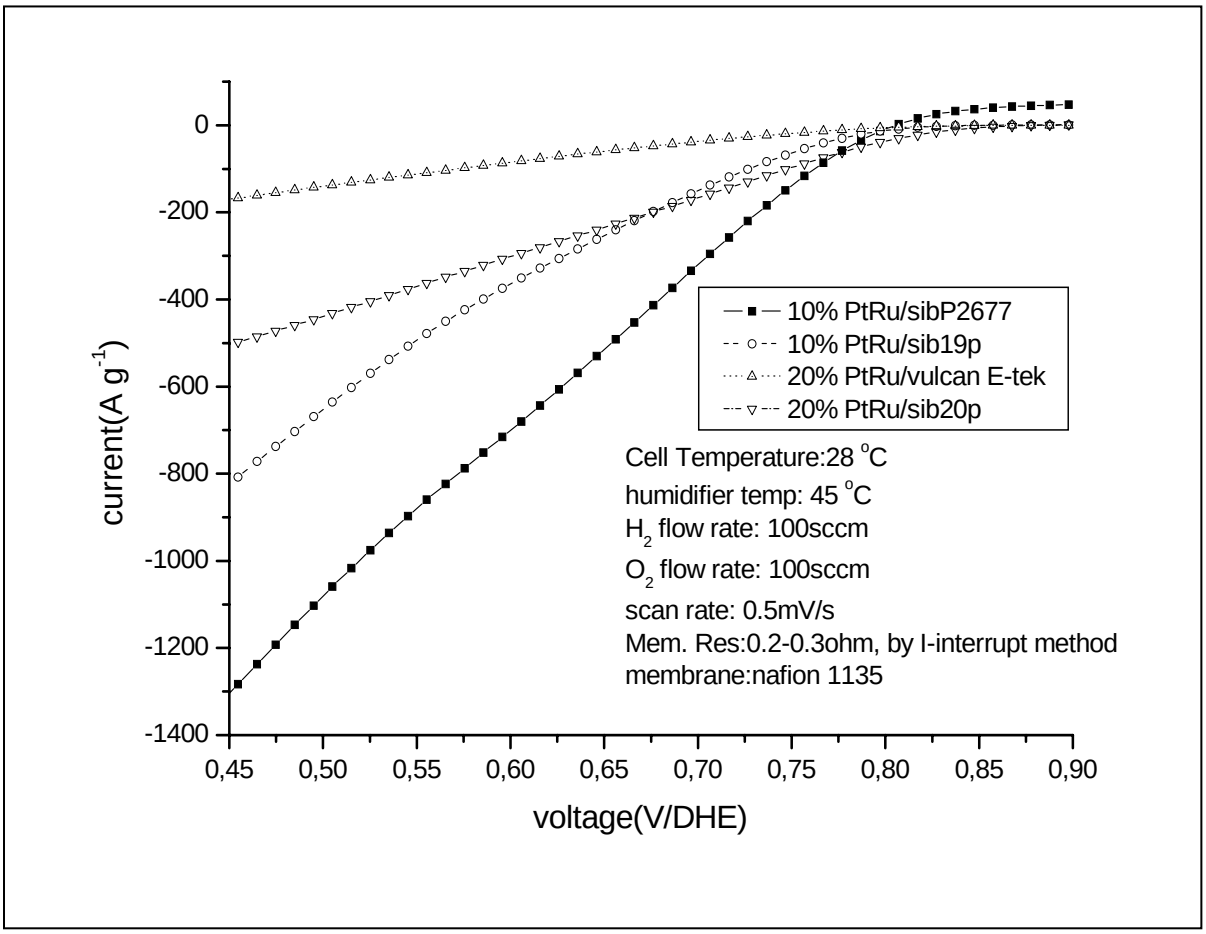

Figure 3.27. Mass normalized U-I curves for different catalyst.

There seems to be strong impact of the surface area of the carbon support on the mass activity of the catalyst towards O_2 reduction. Membrane resistance measured by I-interrupt method was found to be in the range of 0.2 –0.3 Ohm for all MEAs, so even though the I-U curves are not IR corrected, it would be appropriate to compare various catalysts below 100mA absolute currents, as there will be very small IR correction. The performance of the catalyst with lowest carbon support surface area shows much higher performance in comparison to Vulcan supported catalyst. The reason behind this behavior may be high catalyst utilization which has been established earlier with the help of CO stripping technique and better mass transport properties because of bigger average pore diameter. For the sibunit series of catalysts the activity decreases with the increasing S_{BET} of the carbon support. But the catalyst with sib20p as a support shows higher activity than Vulcan supported catalyst. For methanol oxidation these two catalysts showed similar activity. The following curve shows not-mass normalized I-U curves.

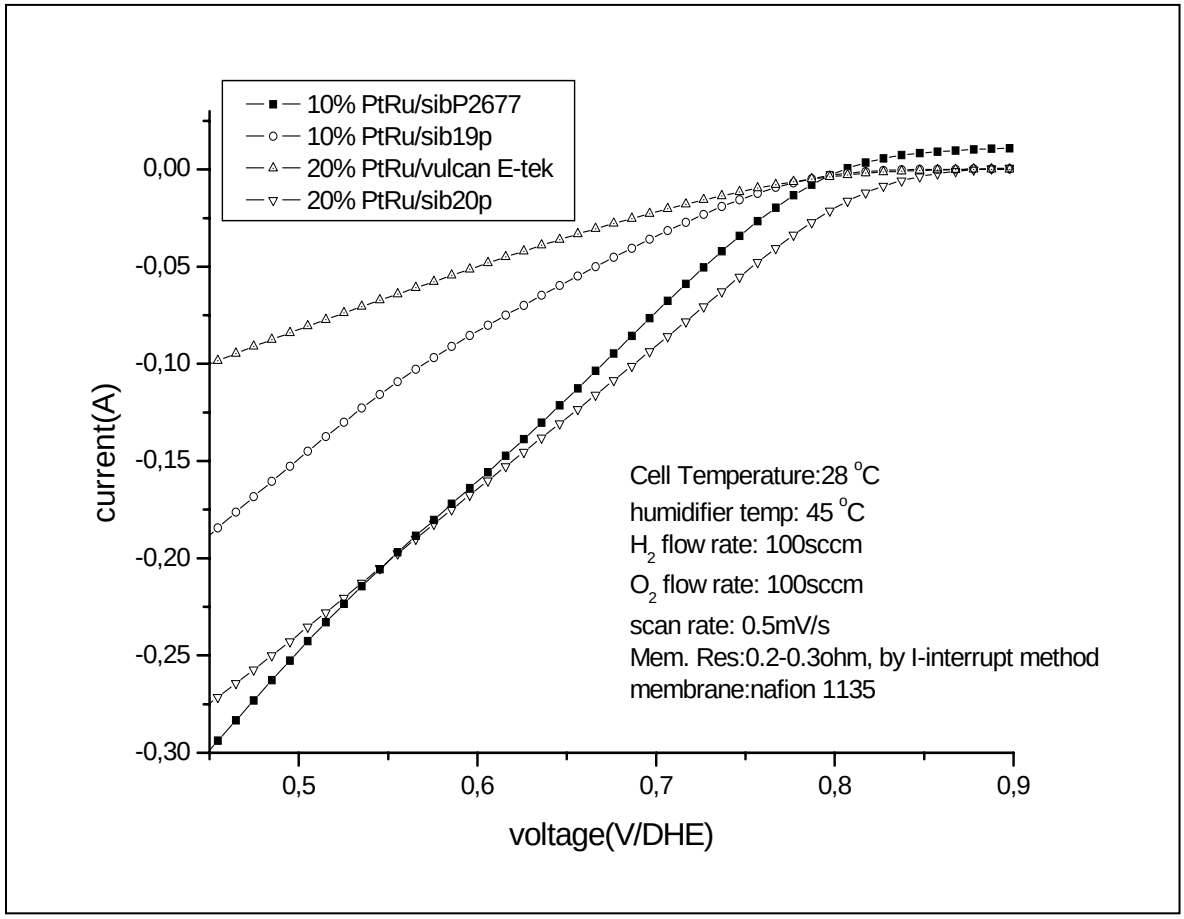

Figure 3.28. Actual U-I characteristic for different catalysts.

3.2.2.7 Investigation of the sibunit sample series in electrochemical cell

The catalysts of sibunit series with varying carbon support porosities were also investigated in electrochemical cell environment for methanol oxidation reaction. Activity measurements were performed in the electrochemical cell, in order to understand better the earlier results of activity measurement in MEAs. Measurements were made in electrochemical cell with 0.5M H_2SO_4 electrolyte and $Hg/HgSO_4$ as the reference electrode.

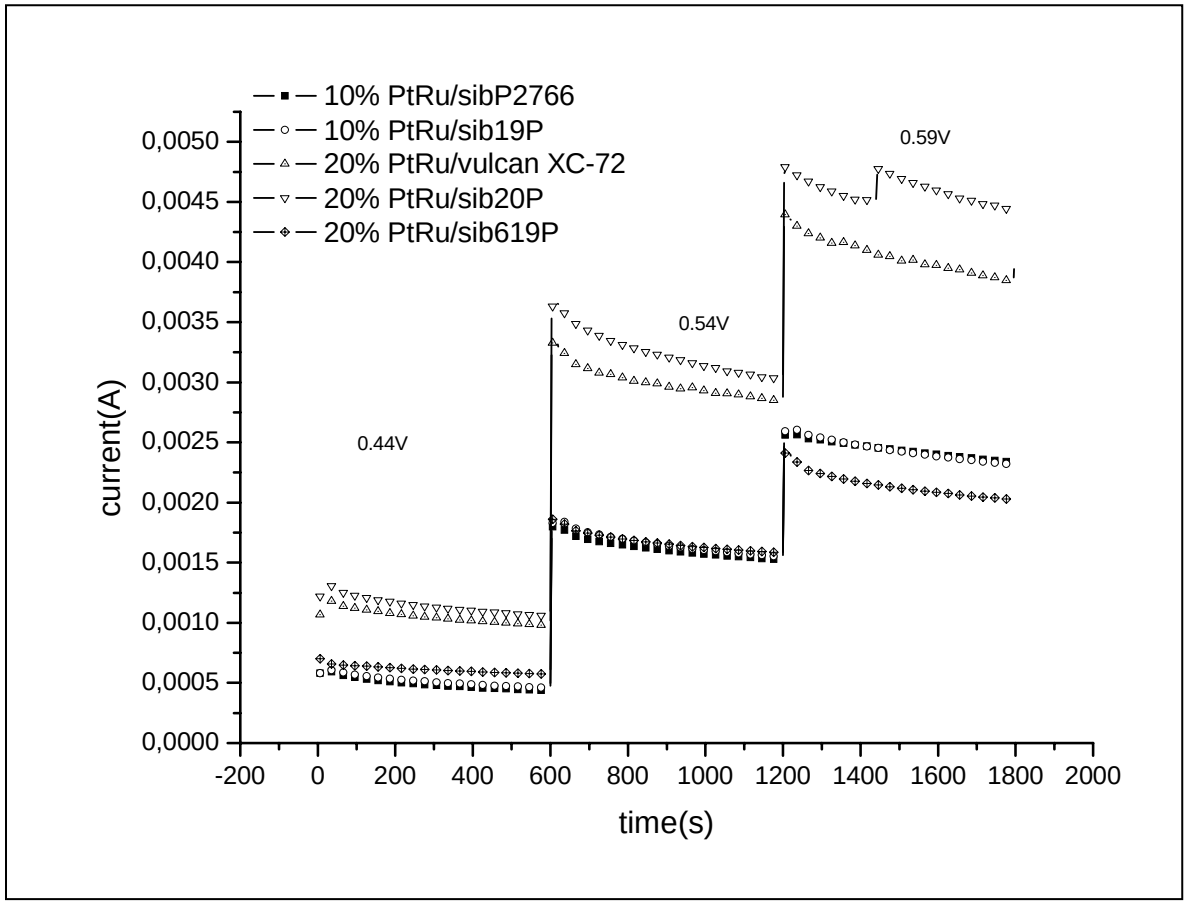

Figure 3.29. Currents at different potential pulses, under potentiostatic oxidation conditions.

A certain amount of the catalyst ink containing 3wt% nafion was deposited on the gold electrode and measurements were then performed in 1M MeOH + 0.5M H_2SO_4 solution. The deposited layer was not stable without nafion.

Potentiostatic oxidation measurements were performed at different potentials at 35 ^oC, as is

shown in the Figure 3.29. There was no effect of the rotation speed, since concentration at 1M MeOH is too high for any mass transport problem.

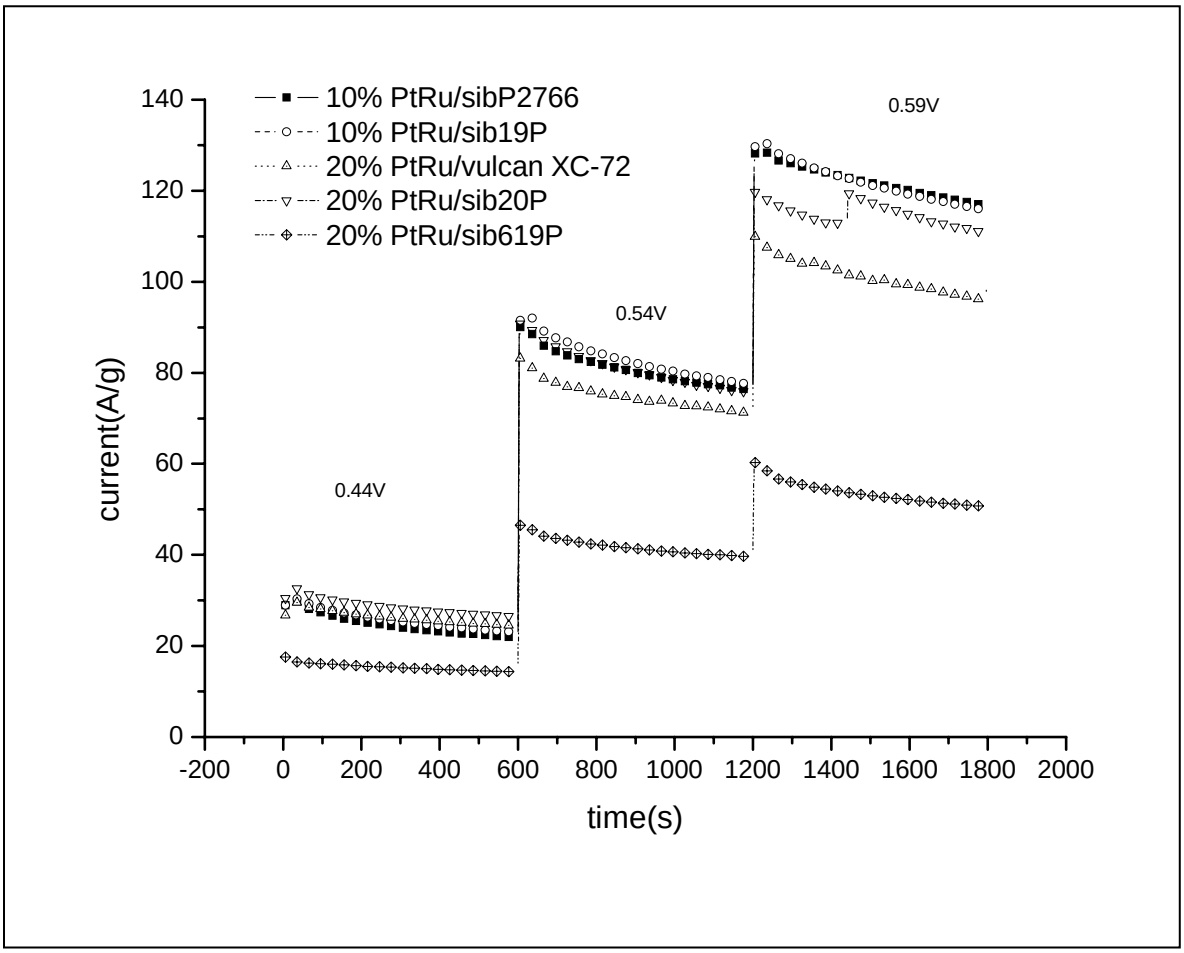

Figure 3.30. Mass normalized currents at different potential pulses, under potentiostatic oxidation conditions. Data for different catalysts is shown.

In these experiments the catalyst layer thickness effects would be absent as the catalyst layer thickness and catalyst loading is very low. Also the catalyst utilization can be expected to be complete, as the liquid electrolyte can contact almost all nanoparticles. There are no problems in electrolytically contacting nanoparticles unlike in a MEA where the nafion micelles can not contact catalyst nanoparticles lying in carbon pores which are smaller than their own minimum size. As can be seen in the Figure 3.31, these experiments shows that in liquid electrolyte there is not much effect of the SSA of the carbon support till 290 m^2/g, and only 20%PtRu/sib619P showed bad performance. So it could be that variation of performance in MEA (nafion electrolyte) with SSA of the carbon support is mainly because of the available electrochemically active area, as in sulfuric acid, we have all particles wetted with electrolyte.

So the advantage of having higher catalyst utilization in MEA form is leveled in liquid electrolyte case at least until the S_{BET} of 290m^2/g. In case of activity of a catalyst in MEA form, since the catalyst layer thickness is higher, so we can expect some other parameters also to come into picture. These parameters could be electrical conductivity or hard and open porous structure. These factors along with higher metal catalyst utilization could explain better activity of low S_{BET} carbon supported catalysts in MEA form.

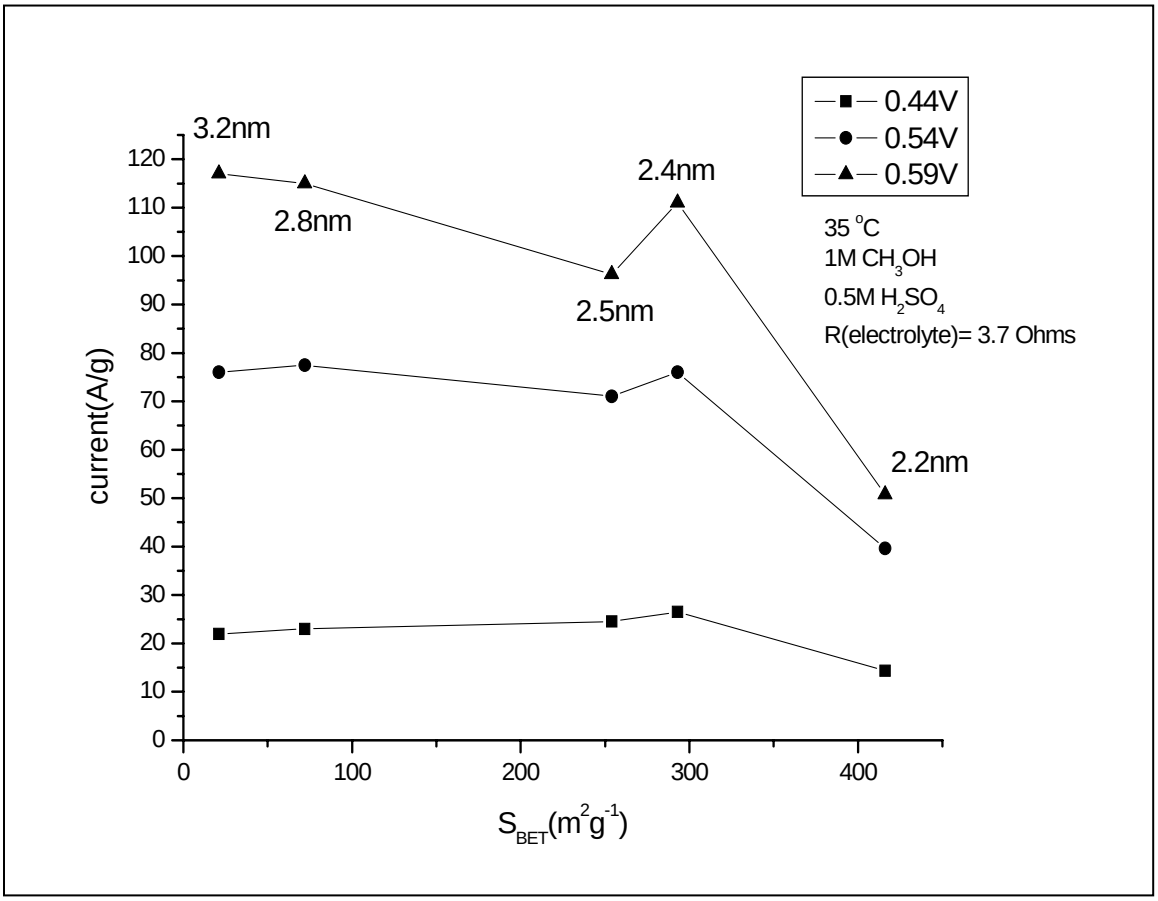

Figure 3.31. Mass normalized currents at different potentials, as function of surface area of the carbon support.

4. In-situ DEMS studies on direct C2-alcohol fuel cells

4.1 DEMS on ethanol oxidation and ethylene glycol oxidation in acidic membranes

4.1.1 Experimental strategies

Using our fuel cell DEMS system we have tried to obtain the product distribution of the ethanol oxidation with the 40 % Pt/C catalyst. It is known that the different oxidation products of ethanol are carbon dioxide, acetaldehyde and acetic acid. Out of them, being volatile enough, only the first two can be monitored by DEMS. But the problem is that the mass number of both CO_2 and CH_3CHO is the same at 44. So to monitor both together is not possible at m/z = 44. One way of solving this problem is by using deuterated ethanol (CD_3CH_2OH) , an approach utilized by Fujiwara et al [81], for determining the product yield ratio between carbon dioxide and acetaldehyde. But the high cost of deuterated ethanol precludes its use for extensive experiments. Another approach is to monitor them as their major fragments. For CO_2 the m / z = 22 corresponding to doubly ionized CO_2^{2+} molecular ions can be used, which has been reported by H. Wang et. al [87]. Similarly for acetaldehyde the most prominent fragment COH^+ at m / z = 29 can be used.

We also monitored the m/z = 22 and 29 during ethanol oxidation for CO_2 and CH_3CHO. The calibration of DEMS for CO_2 is performed with potentiostatic bulk CO oxidation. Figure 4.1 shows a good signal for m / z = 22, although the signal quality is not as good as for m/z = 44, but this current is about a factor of 30 smaller.

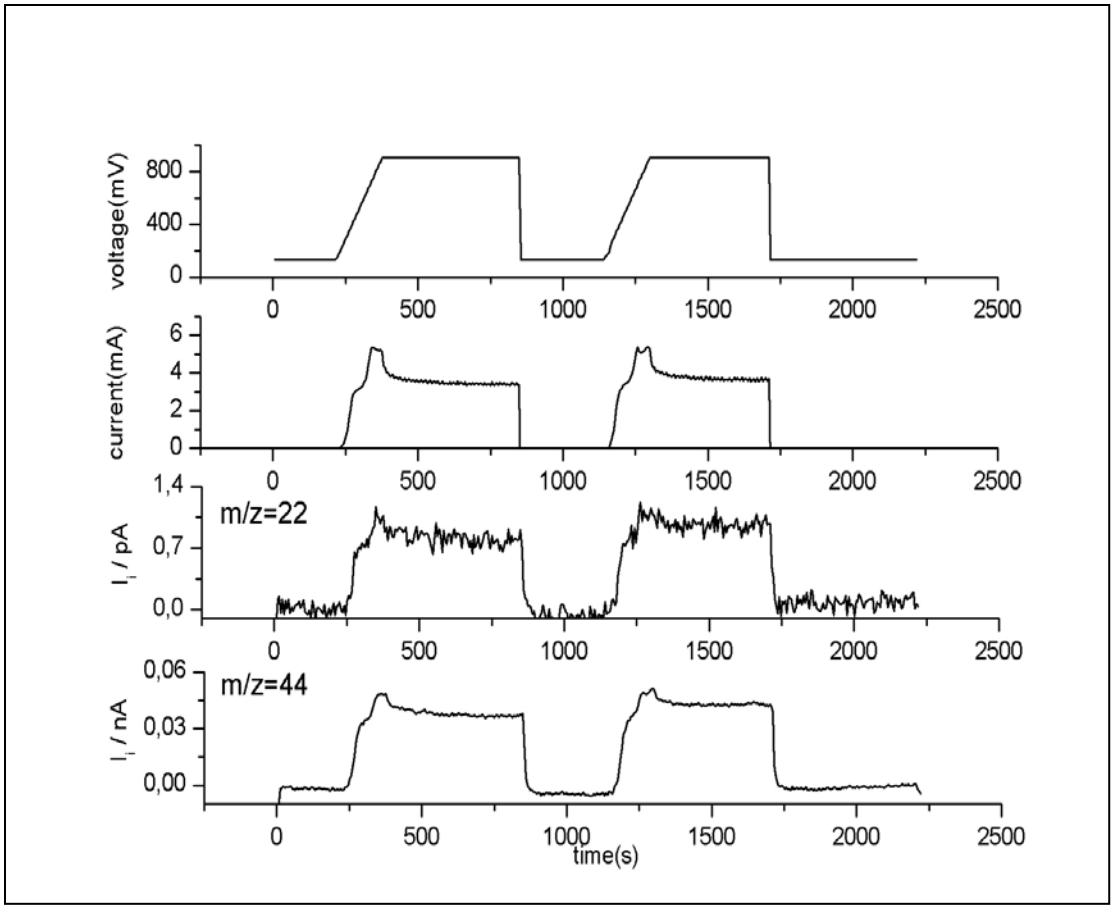

Figure 4.1. This figure shows voltage, bulk CO oxidation current and m/z = 22 and 44 signal as a function of time.

The calibration constant is calculated using the formula:

$K_F^* = 2*I_{MS} / I_F$

where I_{MS} is the steady state ion current for m/z = 22, and I_F is the corresponding faradaic current. In order to measure the current efficiency of CO_2 formation during ethanol oxidation, we performed potentiostatic oxidation of ethanol at various potentials, temperature and concentrations of ethanol. Calibration constants were obtained for all temperatures separately. Then the CO_2 current efficiency can be calculated using the formula:

0 (CO_2 current efficiency) = $6 * I_{MS} / I_F \; K_F^*$

where I_{MS} is the steady state ion current for m/z = 22 for ethanol oxidation, and I_F is the corresponding faradaic current.

Similarly the CO_2 current efficiency for Ethylene Glycol oxidation reaction can be calculated using the formula:

0 (CO_2 current efficiency) = $5 * I_{MS} / I_F \; K_F^*$

where I_{MS} is the steady state ion current for m/z = 22 for Ethylene Glycol oxidation reaction, and I_F is the corresponding faradaic current. The error in determination of CO_2 current efficiency is determined by the m/z =22 signal quality. This could give an error of around ± 10-15%.

4.1.2 Experimental Results

4.1.2.1 CO_2 current efficiency as a function of potential and temperature

Figure 4.2 shows that the CO_2 current efficiency is strongly dependent on potential and temperature. The increase in the CO_2 current efficiency with temperature can be explained by the fact that the kinetics of the C-C bond breaking will be accelerated at higher temperatures.

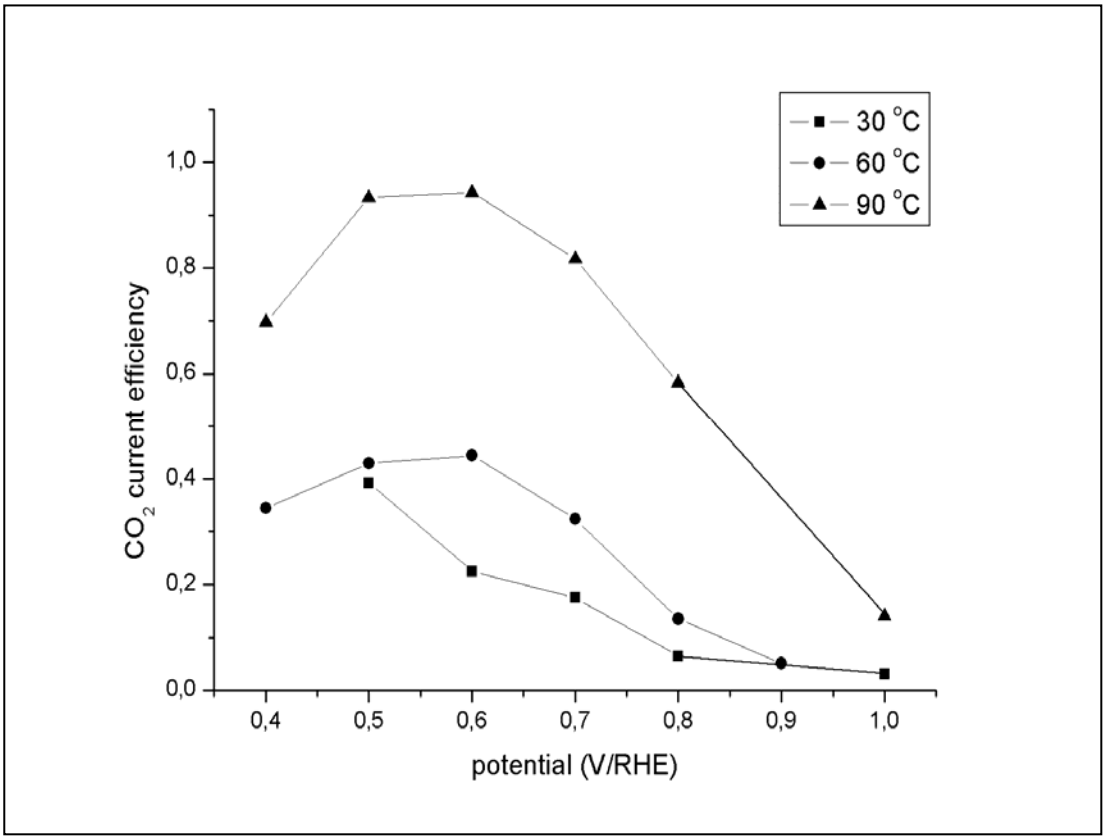

Figure 4.2. CO_2 current efficiency vs. potential for different temperatures. Measurement is done in a fuel cell MEA. Anode: 40% Pt / C (Alpha Aesar), 5 mg / cm^2 metal loading. Anolyte : 0.1M EtOH.

The decrease in CO_2 current efficiency after 0.6 V is a bit surprising result. Although we can

expect that at potentials > 0.8 V the Pt surface is mostly covered by PtO, which may hinder the complete oxidation of ethanol, but will support formation of various oxidation by-products like acetaldehyde and acetic acid [87]. We also found that the formation of acetaldehyde is more favored at high potentials, as can be seen in Figure 4.3. The m/z = 29 is assigned to the major acetaldehyde fragment COH^+. In Figure 4.3 the MSCV of m/z = 22 have a peak at around 850 mV and after that it declines fast. On the contrary m/z = 29 (acetaldehyde) follows the faradaic current, as it becomes flatter at higher (> 1V) potentials, but no decrease in m/z = 29 ion current. Acetaldehyde formation depends strongly on the concentration and temperature also. At higher temperature and lower concentration less acetaldehyde is formed as can be seen in Figure 4.5.

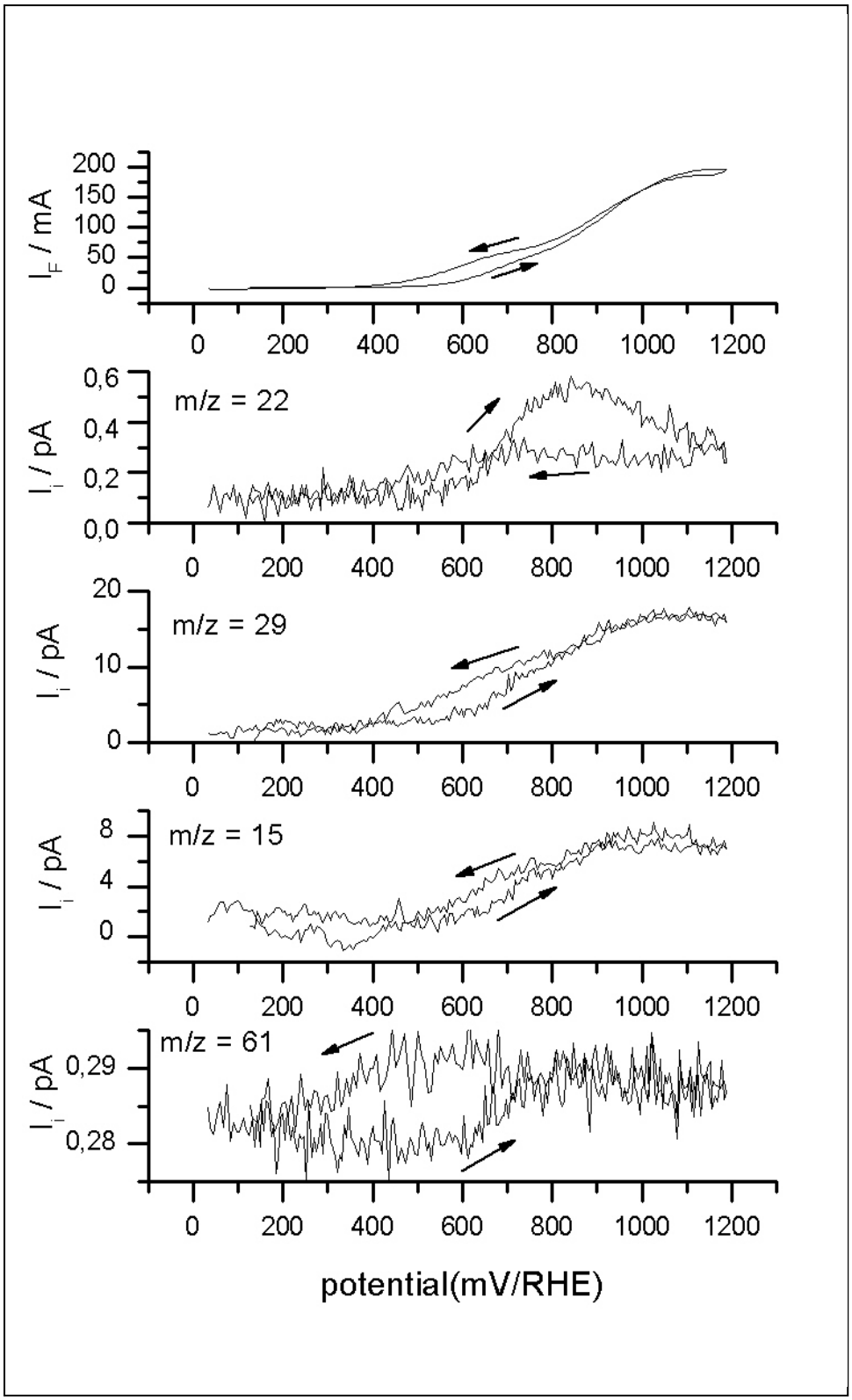

Figure 4.3. This figure shows CV and MSCV for m/z = 22, 29,15 and 61. The anode feed is 1 M EtOH at 5 ml/minute at 30 ^{0}C. Scan rate is 1 mV/s.

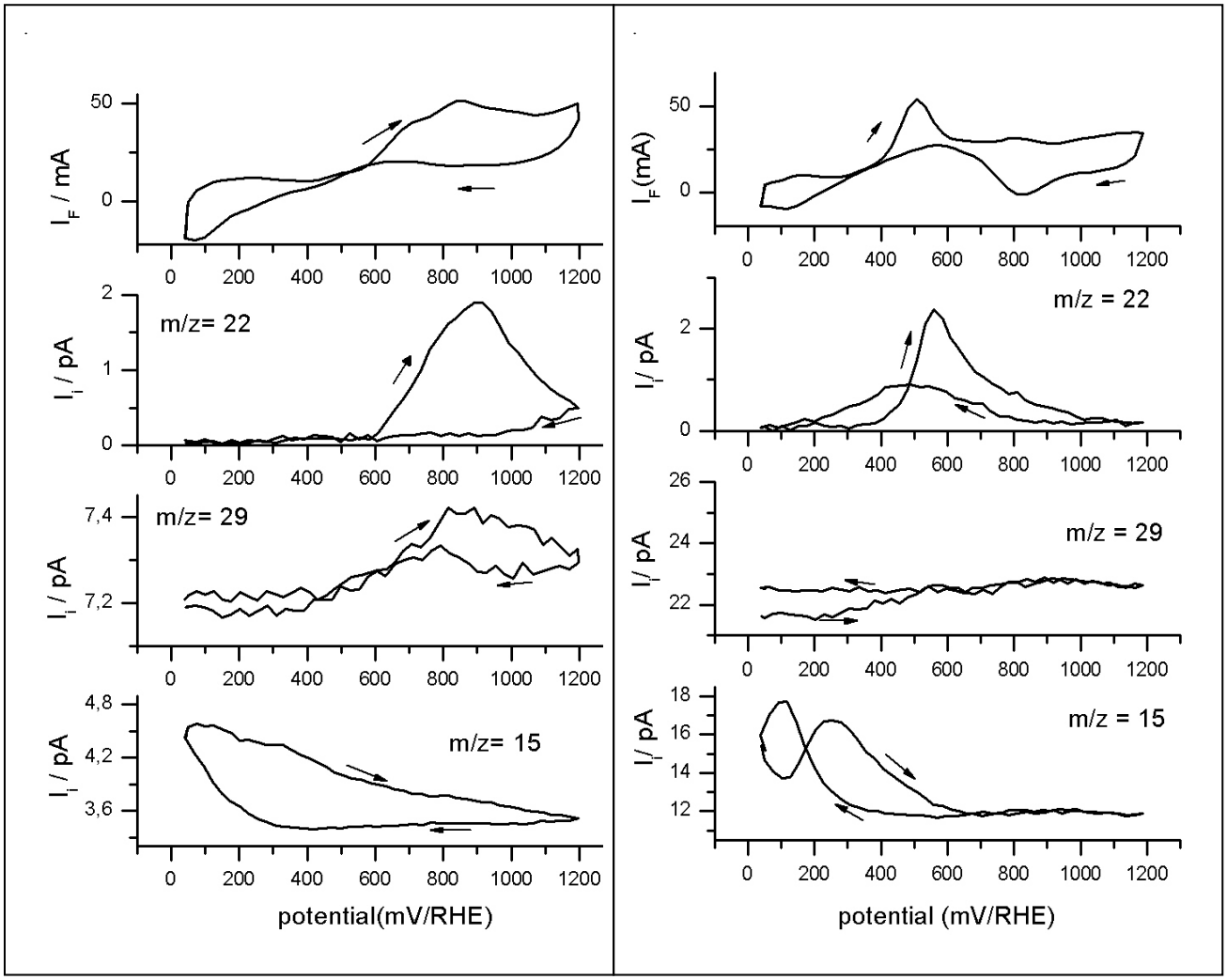

Figure 4.4. This figure shows CV and MSCV for m / z = 22, 29 and 15.The anode feed is 0.1 M EtOH at 5 ml/minute at 30 ^{0}C.scan rate is 5 mV/s.

Figure 4.5. This figure shows CV and MSCV for m/z = 22, 29 and 15. The anode feed is 0.01 M EtOH at 5 ml/ minute at 90 ^{0}C.scan rate is 5 mV/s.

The m/z = 15 corresponds to the CH_3^+ ion which is a fragment of methane and acetaldehyde also have a fragment at m/z = 15 (rel. abundance 40 %). Formation of methane is reported by the cathodic reduction of the adsorbed species, which are formed by the dehydrogenation of ethanol on catalysts surfaces [87, 125]. In Figure 4.3, the m/z = 15 signal rises with the potential on positive side and almost follows the m/z = 29 (CH_3CHO) signal, as acetaldehyde is the main source of CH_3^+ fragment in potential range > 0.4V. Cathodic production of methane is overshadowed by the CH_3CHO, which is a major product at 1M EtOH concentrations and low temperature.

But at lower concentration of 0.1 M EtOH, with high CO_2 current efficiency (40% at 30 ^oC and 0.5V), CH_3CHO seems to be a minority product, as there is no rise in m/z = 15 signal in the positive potential range (Figure 4.4). At 0.01M EtOH and at 90 ^oC there is no formation of acetaldehyde as can be seen in both m/z = 15 and m/z = 29 signals (Figure 4.5). In both cases cathodic methane is formed in potential range < 0.4V as can be inferred from the rising signals of m/z = 15 in Figure 4.4 & 4.5.

m/z = 61 is a fragment (100% rel. Abundance) of ethyl acetate, which provides an indirect way of monitoring acetic acid. The detection sensitivity is low through DEMS, because of low volatility, as the B.P. of ethyl acetate is 77 ^oC. The formation of ethyl acetate is through the esterification reaction between the acetic acid (formed as a byproduct of ethanol, oxidation) and unreacted ethanol, possible catalyzed by the acids. m/z = 61 in Figure 4.3 shows that the onset of the formation of ethyl acetate is around 600mV and after that signal saturates at higher potentials. In the negative scan it shows a peak at around 500mV.

The CO_2 current efficiency for ethanol oxidation, which we found in our fuel cell DEMS measurements, is significantly (about an order of magnitude) higher than, what has been reported in model electrochemical systems with thin catalyst layers or polycrystalline platinum electrodes, as measured by Wang et al. [87] using DEMS , by Camara et al [86] using FTIR spectra and by Vigier et al [93] using HPLC. It is likely because of a thicker catalyst layer (>100 microns with 5 mg / cm^2 metal loading using 40 % Pt / C, in our case), where the desorbed and dissolved intermediates stay a longer time in proximity to the catalyst allowing for readsorption and thus resulting in a more complete oxidation of the ethanol. The thickness of the catalyst layer plays obviously an important role in the formation of the final by-products, as thin layers seem to produce more acetaldehyde. The effect of the catalyst loading and thus catalyst layer thickness on the CO_2 current efficiency for ethanol oxidation will be discussed later in this chapter.

4.1.2.2 CO_2 current efficiency as a function of concentration

The CO_2 current efficiency is lower for higher concentrations of ethanol. This result agrees with the findings of DEMS[87, 126] and FTIR spectroscopy[86] experiments on ethanol oxidation. The similar tendency of CO_2 current efficiency variation with increasing concentration has also been reported for methanol oxidation reaction[127, 128].

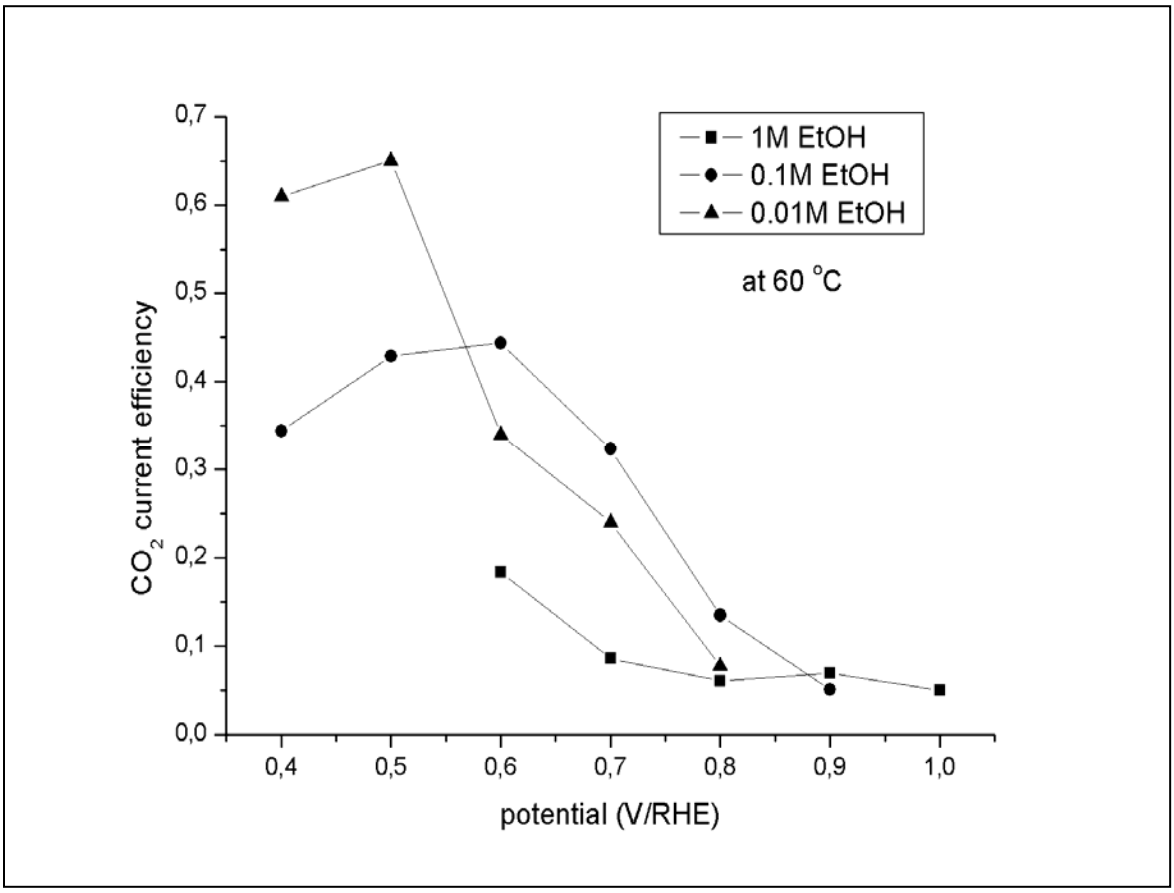

Figure 4.6. This figure shows CO_2 current efficiency versus potential for different ethanol concentrations, at 60 ^oC.

A probable reason for these phenomena is that at higher concentrations, it is more likely that soluble intermediates may get out of the cell unoxidized, since there are enough of ethanol molecules available which are waiting for first step of oxidation. So under high ethanol concentration conditions partial oxidation routes becomes relatively more prominent.

As can be seen in Figure 4.7 the CO_2 production passes through a maximum, which is reasonable because as the concentration of EtOH increases, the partial reactions like formation of acetaldehyde become dominant. This observation agrees well with the results of Camara et al [86] , who reported that the CO_2 production passes through a maximum at 0.025M C_2H_5OH and then decreases, for their polycrystalline platinum electrode.

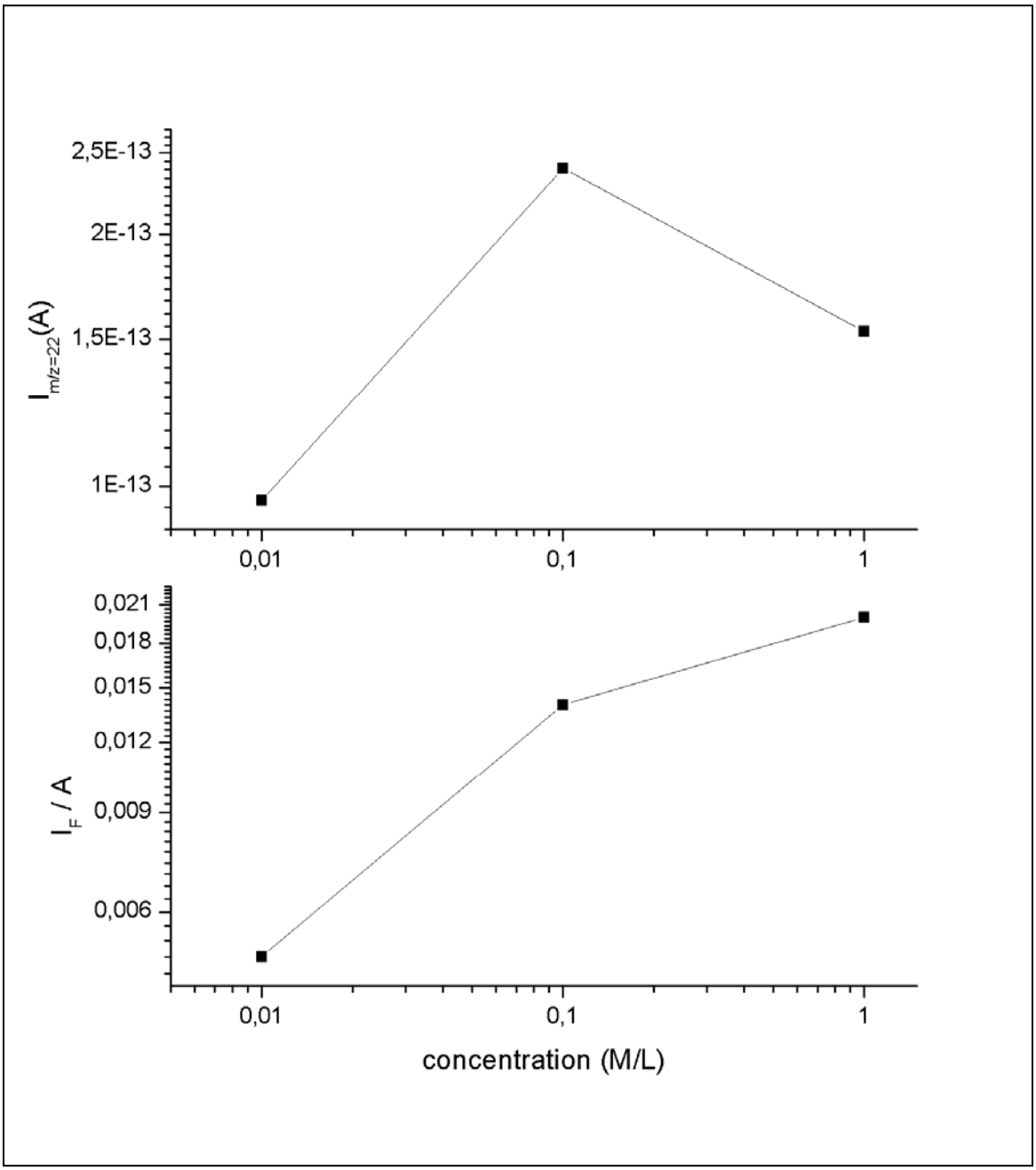

Figure 4.7. This figure shows m/z= 22 ion current and faradaic current vs. concentration on log scale. Temperature is fixed at 30 ^{o}C.

In our case this optimum concentration is around 0.1 M. This difference is explainable by the difference in the electrode structure, which is a thick layer made up of nano-particle catalyst in our case. Assuming linearity below 0.1 M EtOH concentration, reaction order was calculated from first two points of Figure 4.7. A reaction order of 0.4 for CO_2 formation reaction, and 0.45 for overall ethanol oxidation reaction, agrees with values that haven been reported in literature [87].

4.1.2.3 Activation energy calculation

From the linear slopes of the Arrhenius plots in Figure 4.8 averaged apparent activation energy was determined for overall ethanol electro oxidation reaction and for partial reaction of for the formation of the product CO_2.

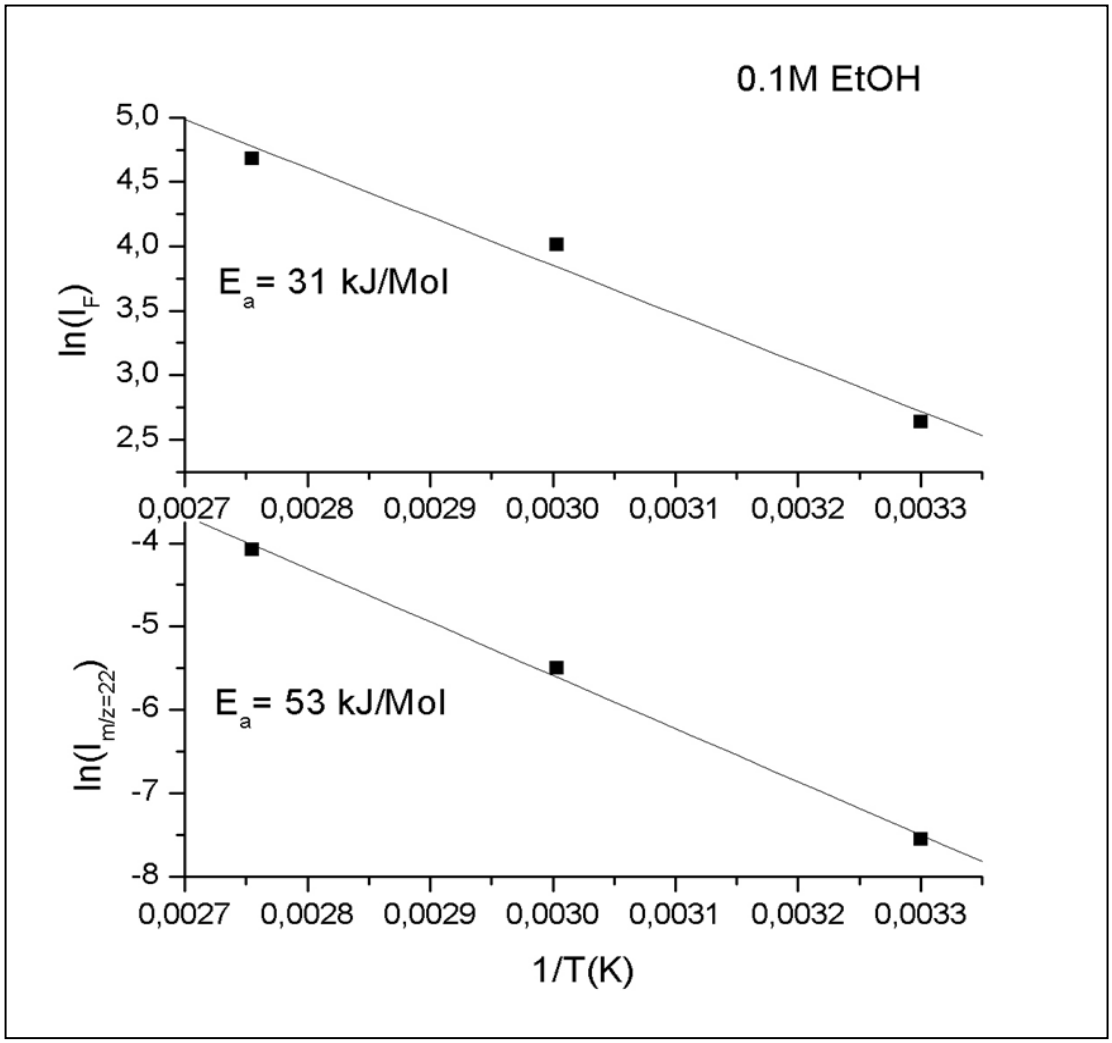

Figure 4.8. This figure shows the Arrhenius plots with 0.1 M EtOH and at 0.6 V RHE. Catalyst used is 40% Pt/C and loading is 5mg/cm^2.

The apparent activation energy calculated from the faradaic currents for ethanol oxidation in the temperature range 30-90 ^oC (with 0.1 M EtOH and at 0.6 V RHE) over the 40% Pt/C catalyst, is 31 kJ/mol, agrees quite well with literature. The activation energy for CO_2 formation was calculated after correcting the m/z=22 ion current for temperature effects of MS, and is 53 kJ/mol. This do not agree with the apparent activation energy for CO_2

formation reported by Wang et al[87], which is 20kJ/mol. But Wang et al used overall charge from CV in ethanol in potential range 0- 1.2 V/RHE, for calculating apparent activation energy instead of potentiostatic bulk oxidation currents at 0.6V /RHE, as in our case. We found that the CCE depends strongly on the potential of oxidation. So this difference in the protocol of activation energy calculation may explain the difference in the values of apparent activation energy for CO_2 formation.

4.1.2.4 Effect of catalyst layer thickness or catalyst loading

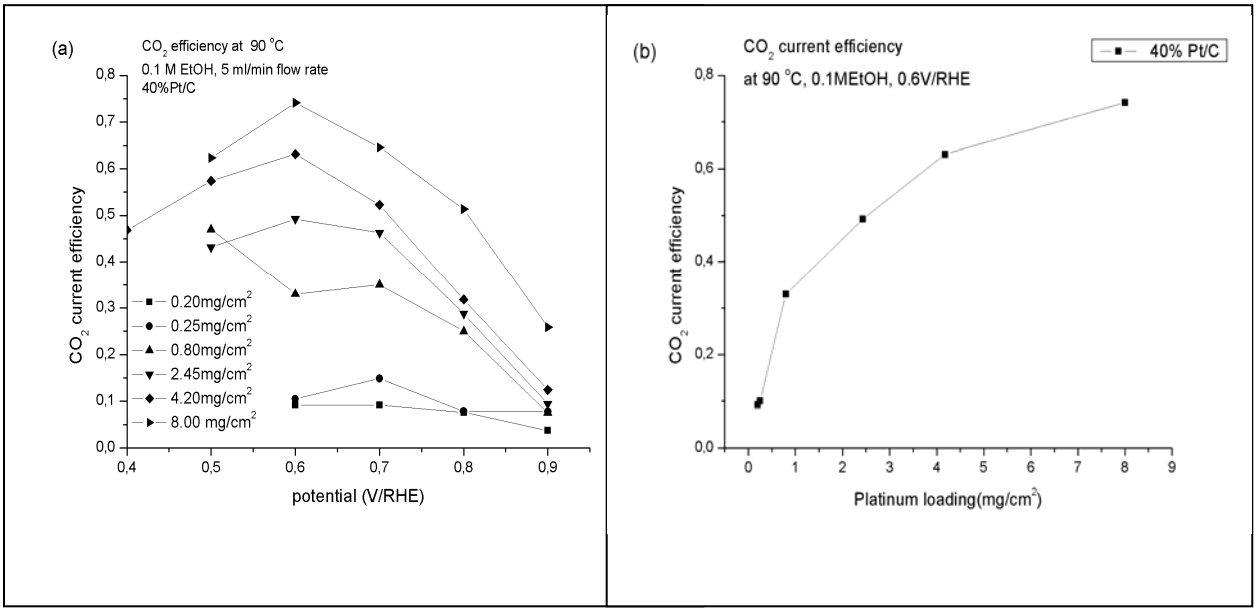

Figure 4.9. (a) CO_2 current efficiency versus potential for different catalyst loadings, at 90 ^oC. (b) The variation of CCE as function of metal loading at oxidation potential of 0.6V /RHE Anode feed is 0.1M EtOH with 5ml/minute flow speed. Catalyst used is 40% Pt/C.

The effect of catalyst loading and thus the catalyst layer thickness, on the CO_2 current efficiency for ethanol oxidation reaction is very important to understand, if we wish to evaluate different catalysts in fuel cell conditions. But this effect has more to do with the physical parameters of catalyst layer and flow conditions than the real activity of the catalyst towards EtOH reaction. The porosity, pore size distribution, residence time and other flow conditions determine the product distribution. For low loading cases we observed negligible CO_2 current efficiency at 30 ^oC. This result agrees well with the literature [86, 87, 93]. With

our fuel cell DEMS operating at 3 bar overpressure we could measure CO_2 current efficiency at higher temperatures as well, which was found to be increasing with increasing catalyst loading and almost saturating to 80%,at catalyst loading of 8mg/cm^2, at 90 °C .

4.1.2.5 Different catalysts show different CCE even with same metal loading

Although the CCE for a same catalyst increase with increasing catalyst loading, this has been discussed earlier for the case of 40% Pt/C. But platinum loading itself does not seem to be the determinant for CCE as we found that with other catalysts like unsupported Pt, 20% PtSn/C and 20% Pt/C do not follow the same graph like 40% Pt/C.

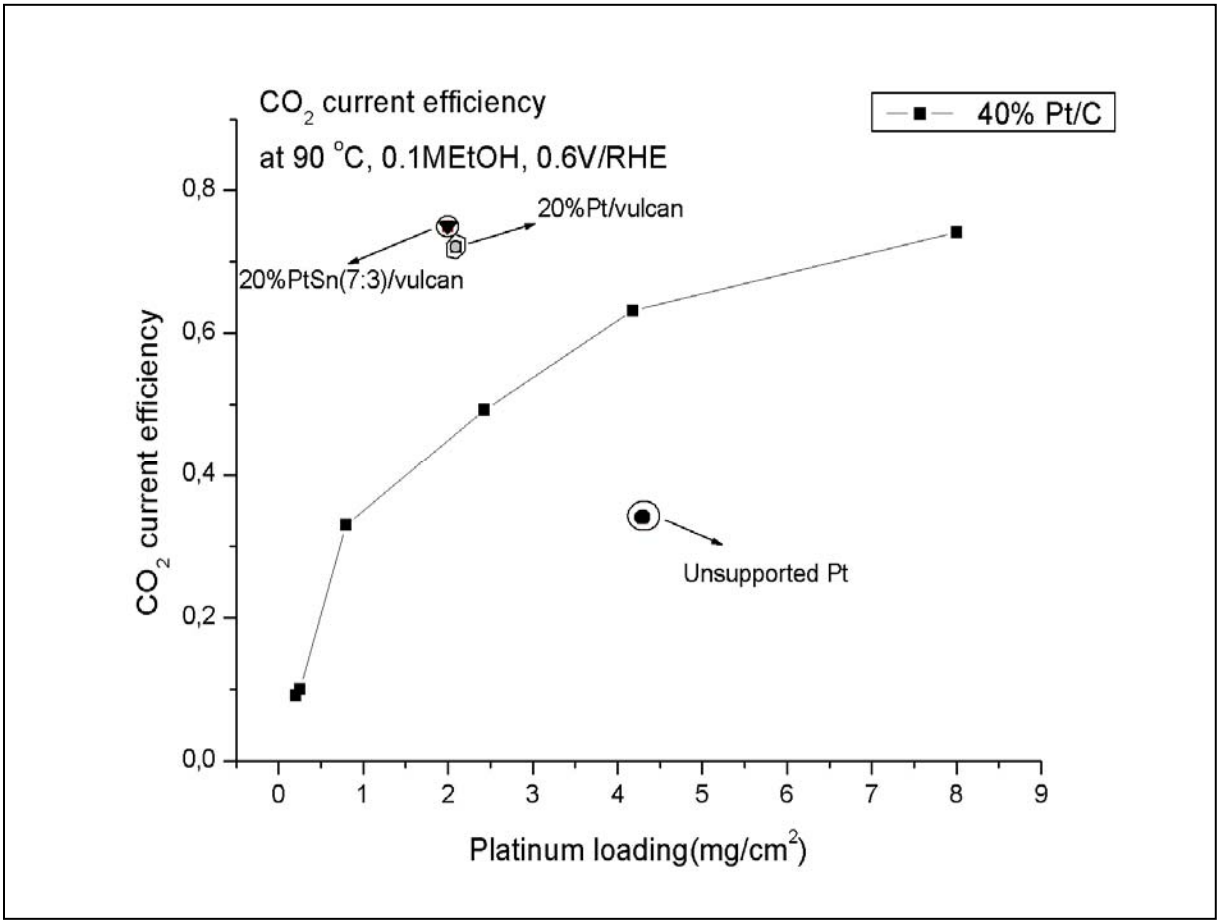

Figure 4.10. CCE versus platinum loading for different catalysts.

The reason behind this discrepancy is the difference in the electrochemically active area (ECA). The ECA is the area which is available for readsorption of the intermediates of EOR. The next section deals with the effect of the ECA on the CCE.

4.1.2.6 Effect of electrochemically active area available in the catalyst layer on the CCE

The CCE depends strongly on the metal loading and thus also the catalyst layer thickness. For same catalyst the CCE vs. metal loading follows a saturating curve. But if we want to analyze other catalysts for CCE, which have different metal % on carbon support or unsupported catalyst, then CCE do not follow the same curve as 40%Pt/C.

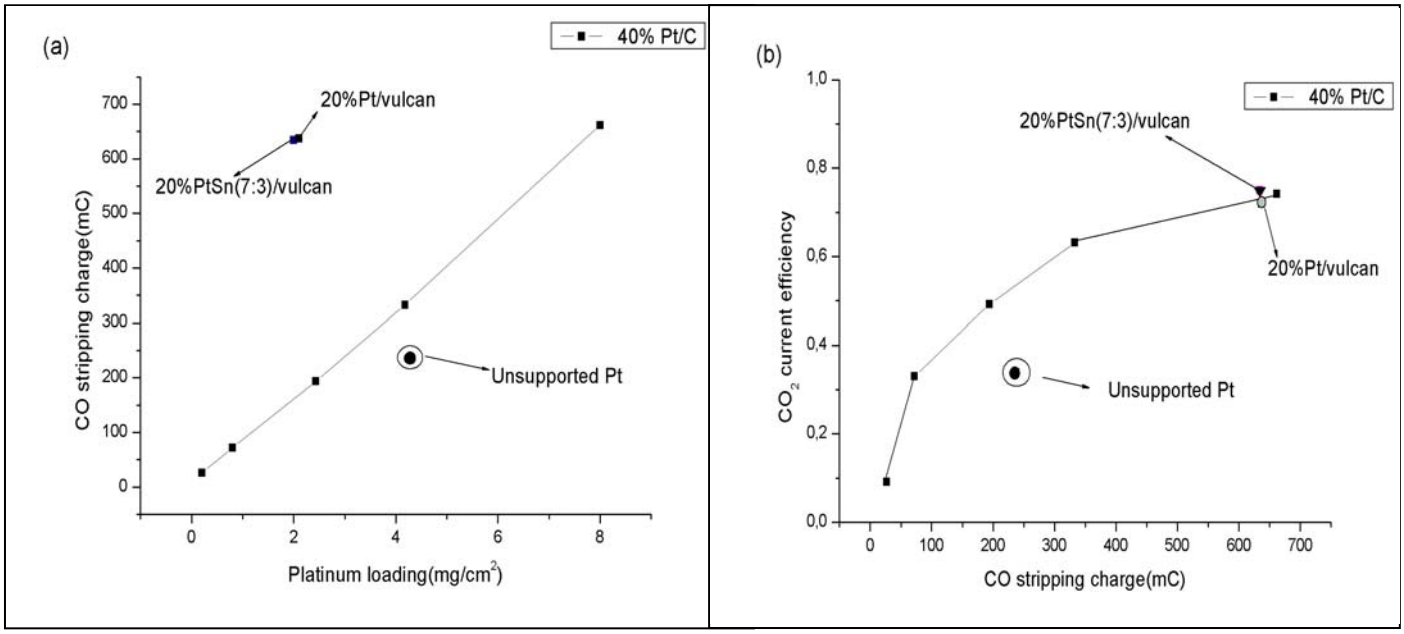

Figure 4.11. (a) The graph on the left side shows CO stripping charge variation with the platinum metal loading in catalyst layers. (b) The graph on the right side shows dependence of CCE on the CO stripping charge for anode catalyst layer.

To under stand this we measured the ECA for each catalyst layer and thus each metal loading. The left part of Figure 4.11 shows the CO stripping charge vs. platinum loading, which is quite linear with the metal loading until 8mg/cm^2 for 40%Pt/C.The CO stripping charge is directly proportional to ECA with a conversion factor of 420µC/cm². Catalysts namely 20%PtSn/C, 20%Pt/C and unsupported Pt are also indicated in the Figure 4.11. Expectedly 20% PtSn/C and 20%Pt/C have better dispersion and higher ECA than 40%Pt/C for the same Pt loading. Similarly unsupported Pt has lower ECA than 40%Pt/C for similar Pt loading which is also on expected lines. Right part of Figure 4.11 shows the CCE versus the CO stripping charge (ECA). In this figure the 20%PtSn/C and 20%Pt/C seems to follow the same

curve like 40%Pt/C but not the unsupported Pt sample. This result is probably explainable by invoking the concept of a chemical reactor. If we assume the fuel cell electrode as a chemical reactor, which is quite reasonable, since fuel cell electrodes also have active area and reactants flowing in. Then in such a case the product distribution is dictated by the residence time and active area available for the reaction to occur. This could explain the lower CCE for unsupported catalyst for similar ECA. The unsupported catalyst will have lower residence time because of the thin layer for similar metal loading and ECA, as there is no low density carbon support in the catalyst layer. This lower residence time under similar conditions could give rise to lower CCE. Wang et al[87] also reported increase in CCE for EOR when they changed their electrode from polycrystalline Pt to catalyst layer made from a nanoparticle powder in their thin layer flow cell DEMS. This is agreement with our results.

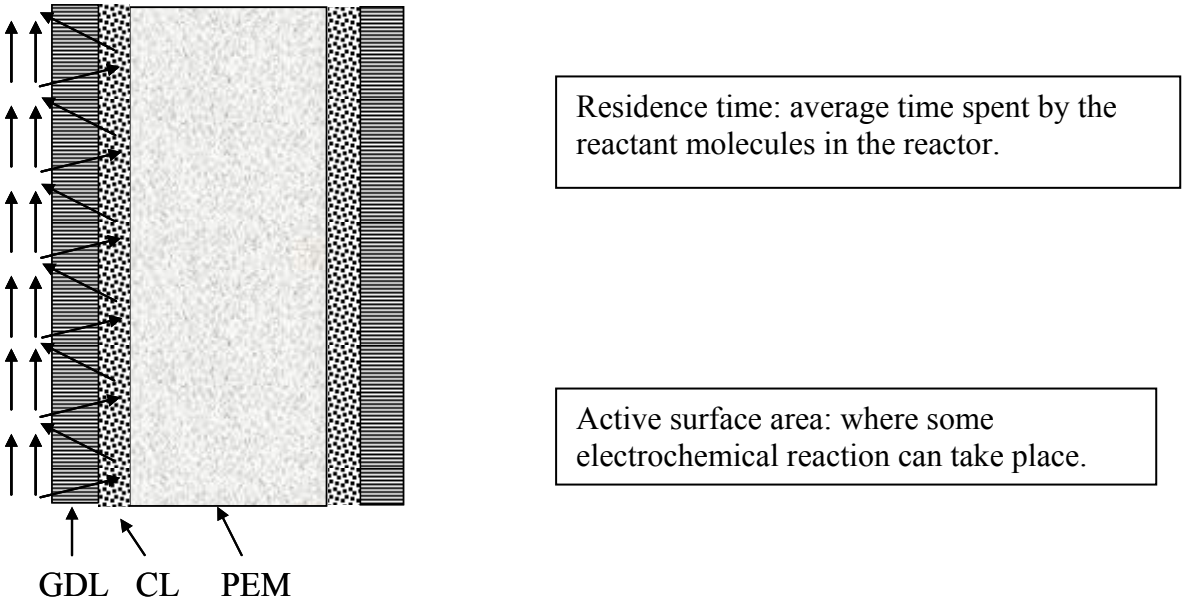

Figure 4.12. This figure illustrates the flow and diffusion conditions in a fuel cell MEA (membrane electrode assembly).The convective flow takes place in a flow field channel. Diffusion is the dominant transport mechanism in GDL (gas diffusion layer) and CL (catalyst layer).

4.1.2.7 CCE dependence on anolyte flow rate

The CCE depends strongly on the thickness of the catalyst layer and the available electrochemical active area in the catalyst layer. The thickness of the catalyst layer would

control the residence time of the ethanol molecules in the catalyst layers. Another way to change the residence time of the reactants is by changing their flow rates. So we investigated the effect of anolyte flow rate on CCE for EOR. Figure 4.13 shows the variation of the CCE with the anolyte flow rate.

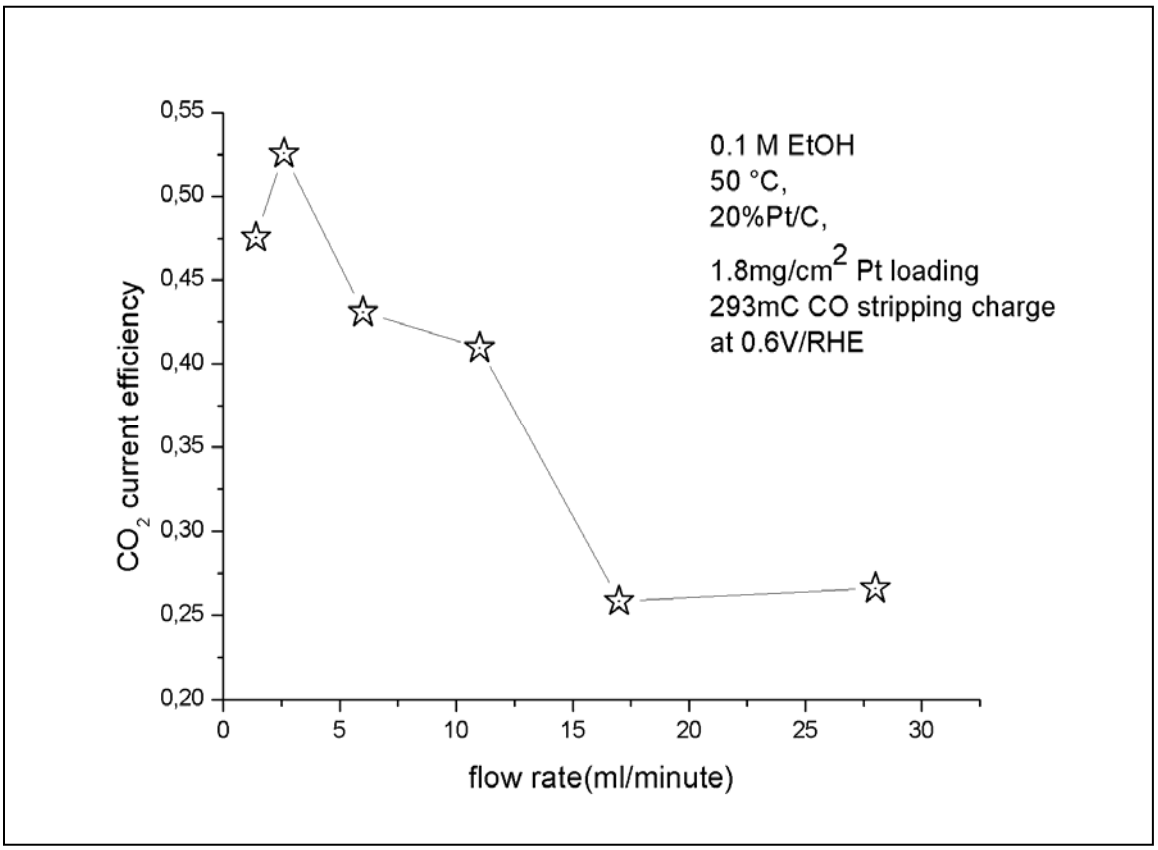

Figure 4.13. CCE variations as a function of anolyte flow rate is shown.

The fuel cell MEA has convection and diffusion as the mechanism for reactant transport to the catalyst layer. By changing the flow rate mostly convection in the flow field channel will be changed, with diffusion rates in GDL and CL remaining same. Diffusion is the dominant mechanism of reactant transport in the GDL and CL. This might explain that changing the flow rate by a factor of 30 changes the CCE only by about 20%.

4.1.2.8 Dissociative adsorption of ethanol on Pt/C and PtSn/C

In these experiments ethanol is allowed to adsorb on the catalysts from a 0.1M EtOH solution at different potentials namely 0.0, 0.1 and 0.2V. Purpose of these experiments is to understand the nature and coverage of adsorbate, which is generally supposed to be C1 species like CO_{ad} or CHO_{ad}.

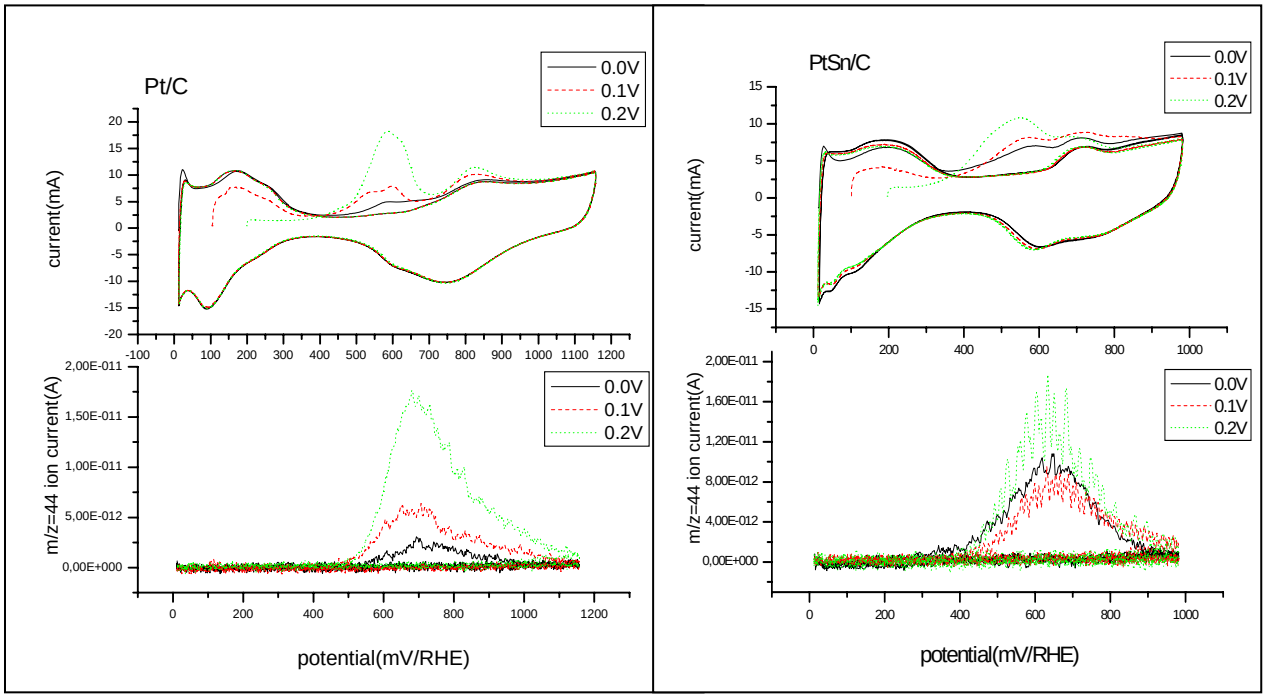

Figure 4.14. Simultaneously recorded CVs and MSCVs of m/z=44, for the oxidation of ethanol adsorbate formed upon adsorption on a Pt/C and PtSn/C catalysts at increasing potentials (scan rate = 5mV/s). The adsorption potential is given in the figure.

Vigier et al measured the adsorbate coverage with the SNIFTIRS, and reported that Pt based catalyst forms the adsorbed CO species at higher potentials than the PtSn based catalyst[92]. It was proposed that the dissociative adsorption of ethanol takes place on PtSn catalyst at lower potentials than Pt, which might explain better activity of PtSn based catalyst for EOR than Pt based catalyst. In this experiment we also determined the equilibrium CO_{ad} coverage on Pt and PtSn catalyst at different potentials <0.3V. The CO_{ad} coverage from dissociative adsorption of ethanol is shown in the Figure 4.15 normalized with the full CO monolayer stripping charge. The CO_{ad} coverage increases with the potential for both catalysts. At 0.0V the Pt shows coverage of 10% but PtSn show coverage of 20%. This result might indicate that PtSn is more efficient at dissociative adsorption of ethanol than Pt at 0 V. But the difference

in the CO_{ad} coverage is lower at 0.1V. At 0.2V Pt has more CO_{ad} coverage than PtSn. Generally there is almost no bulk oxidation current at such low potentials. So the overall result about CO_{ad} coverage in 0-0.2V range do not support the argument that PtSn in more effective at dissociative adsorption of ethanol than Pt. But it is clear that PtSn adsorbs oxygenated species earlier than the Pt which lead to lower onset potential of oxidation of CO_{ad}, as can be seen in the CVs and MSCVs.

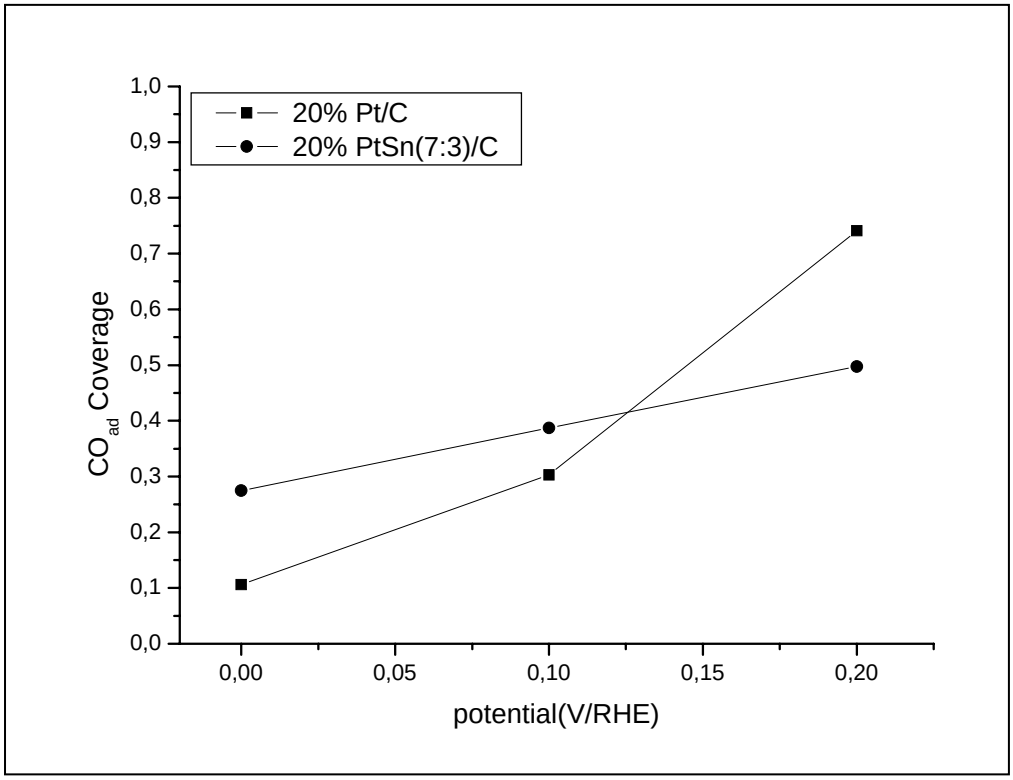

Figure 4.15. CO_{ad} coverage for the oxidation of ethanol adsorbate formed upon adsorption on 20%Pt/C and 20%PtSn/C catalysts at increasing potentials is shown. The adsorbate oxidation charge is normalized to one CO monolayer charge.

4.1.2.9 Dependence of CCE on the intrinsic nature of catalyst

Although it was found that CCE depends strongly on the properties of the catalyst layer. But still one of the most important determinants for the CCE is the intrinsic nature of the catalyst. In our investigation we studied the Pt, 20%PtSn(7:3)/C and 20%PtRu (1:1)/C catalysts for EOR. We found that in similar working conditions the CCE for PtSn and Pt catalysts were high. But PtRu catalyst gave completely different results.

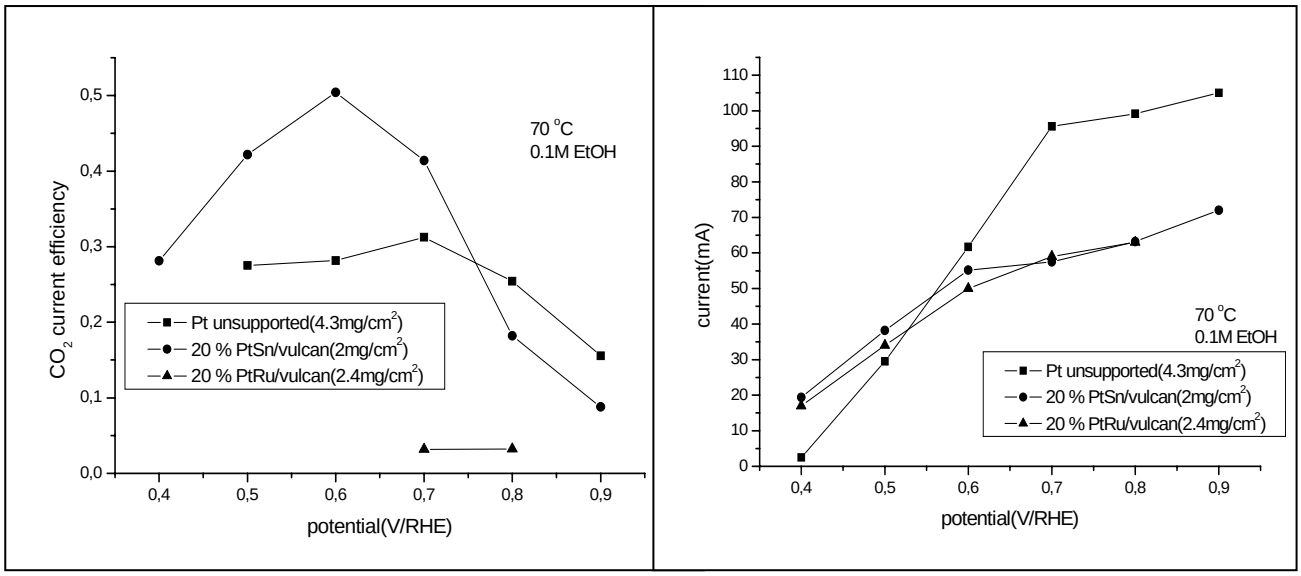

Figure 4.16. The graph on left shows the CCE as a function of potential for unsupported Pt,20%PtSn(7:3)/C and 20%PtRu(1:1)/C. The graph on right side shows the faradaic currents as a function of potential for all three catalysts.

Although the faradic current was comparable to PtSn catalyst but CCE was found to be very low in comparison. In literature similar results has been reported for a rather similar compound, ethylene glycol(EG), which also contains one C-C bond. De Lima et al.[129] studied ethylene glycol electooxidation on PtRu catalysts with different Ru contents and reported that more Ru rich catalyst tend to form more partially oxidized byproducts than CO_2.The oxide covered Ru sites on one hand helps in oxidation of CO like adsorbed species but on the other hand hinders the dissociative adsorption of EG and thus promotes the partial oxidation reaction. This also seems to apply to EOR as well. With our catalyst PtRu(1:1) demonstrate very low CCE as can be seen in the Figure 4.16. For same electrochemical active area in the catalyst layer 20%PtSn(7:3)/C catalyst exhibits similar CCE as pure Pt based catalyst as has been as has been discussed in section 4.1.2.6. This result does not agree with the results reported in ref[94]. In this paper S. Rousseau et al[94] reported that addition of Sn to Pt catalyst brings down the CO_2 yield in ethanol oxidation reaction. Although H. Wang et al[88] reported similar CO_2 current efficiency for Pt/C and Pt_3Sn/C catalysts for ethanol oxidation reaction, which agrees with our results. The actual reason behind these differences related to CO_2 current efficiency of PtSn based catalysts for EOR is yet clear.

4.1.2.10 Direct oxidation of acetaldehyde and acetic acid

Acetaldehyde oxidation was investigated in the fuel cell to determine the nature and quantity of products of oxidation. The experiment showed that acetaldehyde is quite active for further oxidation as the faradaic currents were quite comparable to ethanol oxidation reaction in similar conditions and with same catalyst namely Pt/C. The CCE in acetaldehyde oxidation reaction is also quite good at around 86% at 0.6V, which is also similar to CCE for ethanol oxidation reaction. These results showed that if acetaldehyde is formed as an intermediate in ethanol oxidation reaction, it is still quite active for further oxidation.

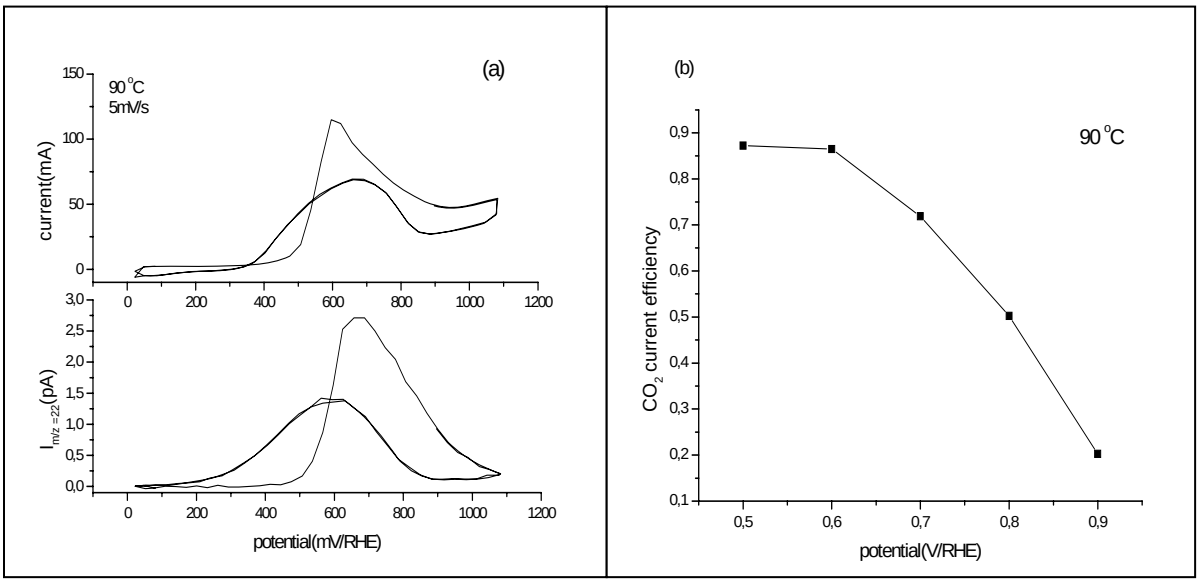

Figure 4.17. (a) This figure shows the CV and MSCV for 0.1M acetaldehyde at 90°C (b) CCE for acetaldehyde oxidation reaction as a function of potential. Catalyst used is 40% Pt/C with 8mg/cm^2 metal catalyst loading.

Similar experiments of direct oxidation were performed with 0.1M acetic acid also to check if it is possible to oxidize it further and what could be the final products of oxidation reaction. Direct oxidation of acetic acid in fuel cell with Pt/C and PtSn/C both showed almost negligible faradaic currents in comparison to ethanol oxidation. Figure 4.18 shows the cyclic voltammograms in 0.1M acetic acid for PtSn/C and unsupported Pt catalysts. The CV with acetic acid solution as anolyte in case of both catalysts shows a peak around 500mV. This peak seems to be because of oxidation of some CO like species. The peaks in hydrogen region in the CV are not much suppressed, which indicate a low coverage of CO like species. After this peak at around 700mV, the currents in acetic acid CV are similar to the base CV in

deionized water. The faradaic currents in acetic acid CV are further compared with the currents in CV with ethanol as anolyte in Figure 4.19. The faradaic currents for acetic acid oxidation reaction are almost negligible in comparison to ethanol oxidation reaction. This indicates that acetic acid is a final product of ethanol oxidation reaction, which is not oxidizable any further.

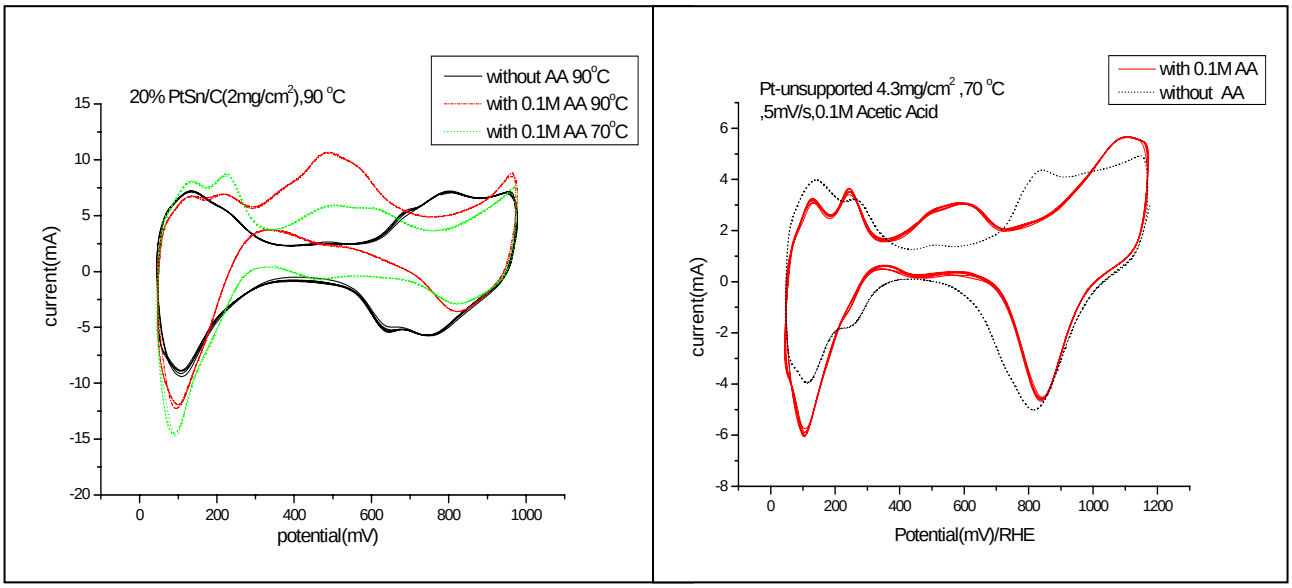

Figure 4.18. (a) This figure shows the CV in 0.1M acetic acid at 70 °C and 90°C for 20% PtSn/C(2mg/cm^2) as catalyst (b) CV in 0.1M acetic acid at 70 °C for unsupported Pt (4.3mg/cm^2).

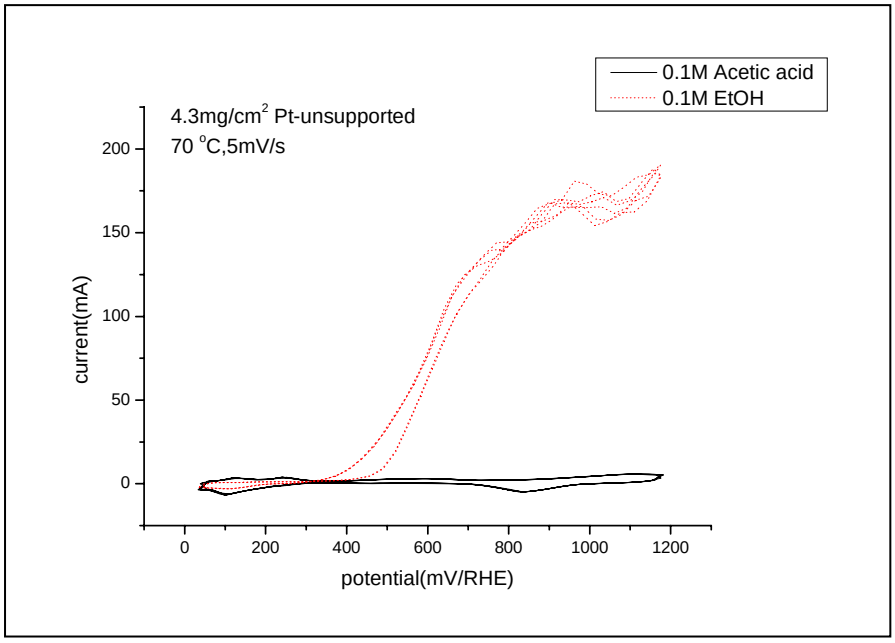

Figure 4.19. CV in 0.1M acetic acid and 0.1M ethanol at 70 °C for unsupported Pt (4.3mg/cm^2).

4.1.2.11 Ethylene glycol electro-oxidation

Figure 4.20 shows the CO_2 current efficiency for 0.1 M EG (Ethylene Glycol) oxidation on carbon supported Platinum catalyst. The CO_2 current efficiency here shows remarkable difference with ethanol in the sense that it is almost independent of the potential and also on an average the CO_2 current efficiency is higher for EG oxidation than ethanol oxidation. The influence of temperature is similar as C-C bond cleavage is temperature-activated process in both cases.

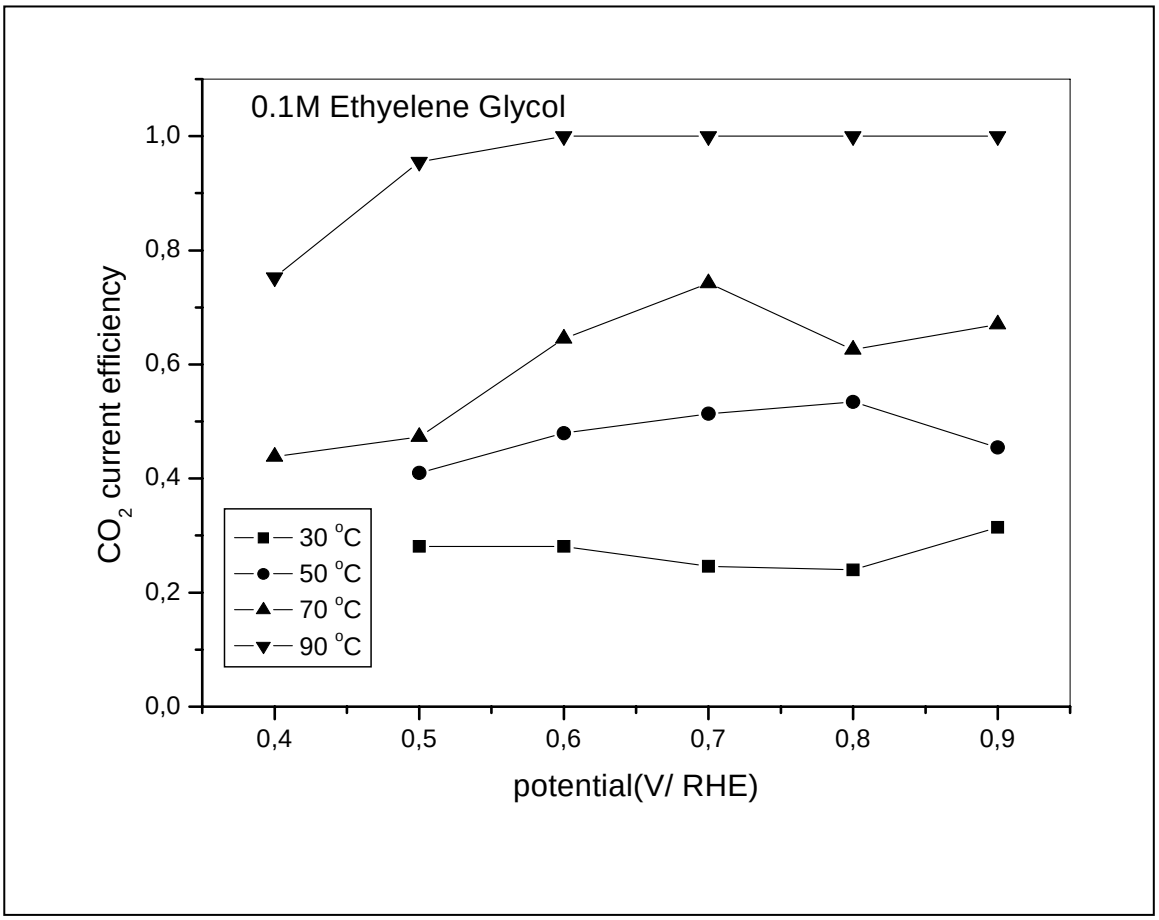

Figure 4.20. This figure shows CO_2 current efficiency vs. potential for different temperatures. 5 mg / cm^2 metal catalyst loading using 40 % Pt / C.

The activation energy for EG oxidation (25kJ/Mol, Figure 4.21) is smaller than EtOH oxidation (31kJ/Mol), as calculated from the faradaic currents at 0.6V RHE. But the activation energy for CO_2 formation (one of the partial reactions) is similar to the case of

ethanol oxidation reaction, which is 53kJ/Mol.This, indicates that there may be some similarities in the mechanism of CO_2 formation, in EtOH and EG oxidation reactions.

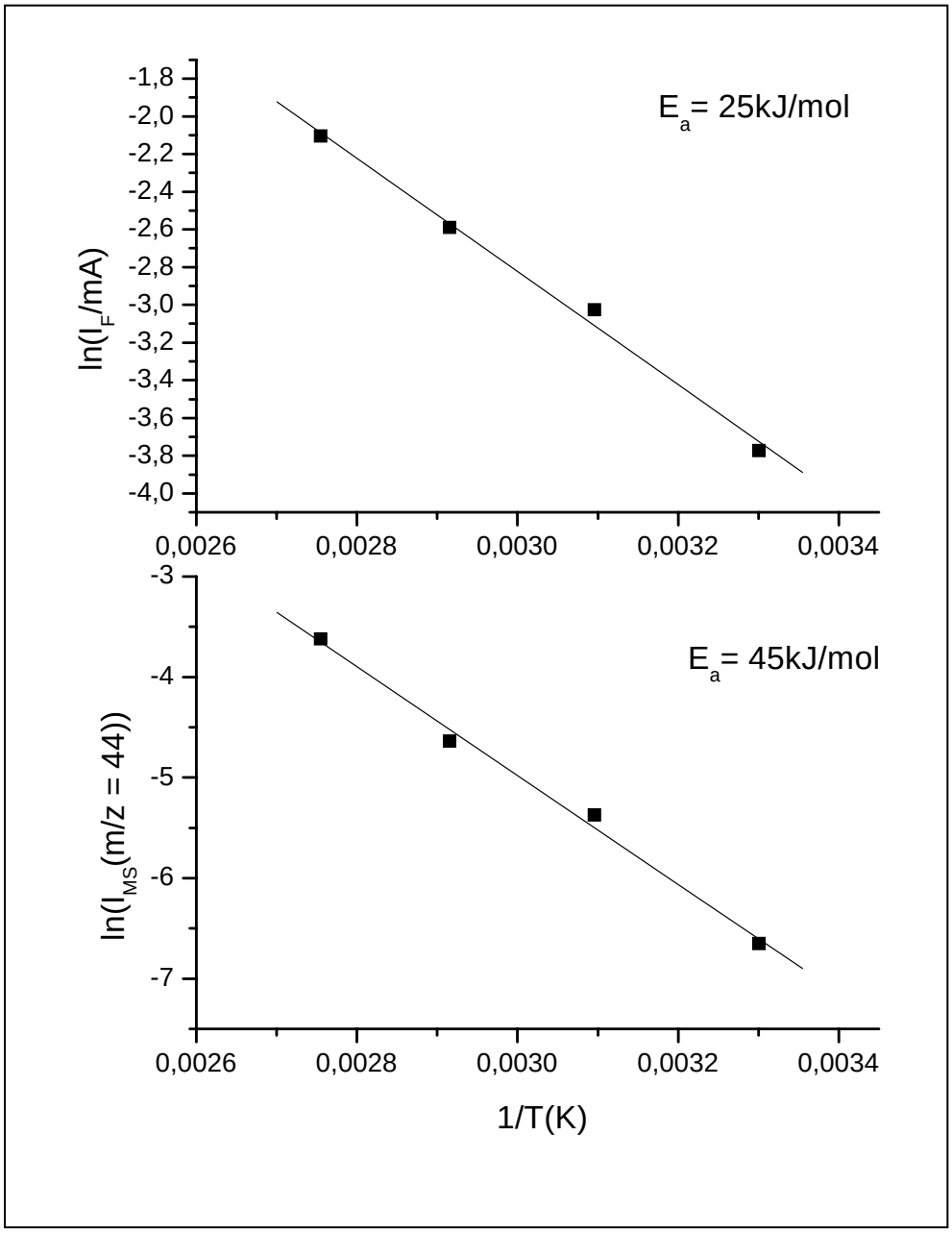

Figure 4.21. This figure shows the Arrhenius plots with 0.1 M EG and at 0.6 V RHE. Catalyst used is 40% Pt/C and loading is 5mg/cm^2.

4.2 DEMS on ethanol oxidation in alkaline membrane electrode assembly

4.2.1 Preparation of the MEA and its characterization

4.2.1.1 Membrane electrode assembly

A suitably sized (2.5*2.5 cm²) piece of membrane is cut. The membrane is then hydrated in 1M KOH solution overnight. Unsupported Pt (Alpha Aesar) is used as a cathode and anode catalyst. In order to make a membrane electrode assembly, the ionomer solution is applied on both side of the membrane and catalyst ink is dispersed by a paint brush subsequently. In a semi-dry stage two carbon backing layers (Toray paper from E-Tek, TGPH 060, no wet proofing), are kept on each side. The whole sandwich is then hot pressed at 100 ^{0}C for 5 minutes and at 826N/cm² pressure.

4.2.1.2 DEMS measurement in alkaline medium

Differential electrochemical mass spectrometry can sense only the volatile products or by-products of any electrochemical reaction. That entails that if any molecule is not volatile enough because of its solubility or because of its boiling point, then DEMS can not sense that molecule. CO_2 is quite volatile from boiling point perspective, but is also very soluble in water. In alkaline solution it will react and form carbonates. So if there is KOH in anolyte then DEMS will not see any CO_2 signal. But even in case of less alkaline solutions like 0.5M Na_2CO_3 (pH=11.5), no CO_2 signal was seen perhaps because of very high solubility of CO_2. So for all DEMS measurement, the anolyte was kept free of any extra alkaline additive. Although in presence of alkaline additives like KOH in anolyte stream the membrane ionic resistance is much lower and the ionic contact between the catalyst layer and membrane is better than when it is absent. But for DEMS measurement we depend on the ionic contact between Pt catalyst layer and solid alkaline membrane interface, for an electrochemical reaction to occur.

4.2.2 Electrochemical characterization of membrane electrode assembly

Electrochemical characterization of the MEA was performed after installing the MEA in a fuel cell. With deionized water as anolyte, the cyclic voltammogram obtained is shown in Figure 4.22. The CV is little bit different from what one expects for Pt. The hydrogen features are clearly resolved, although the oxide region is more clearly visible.

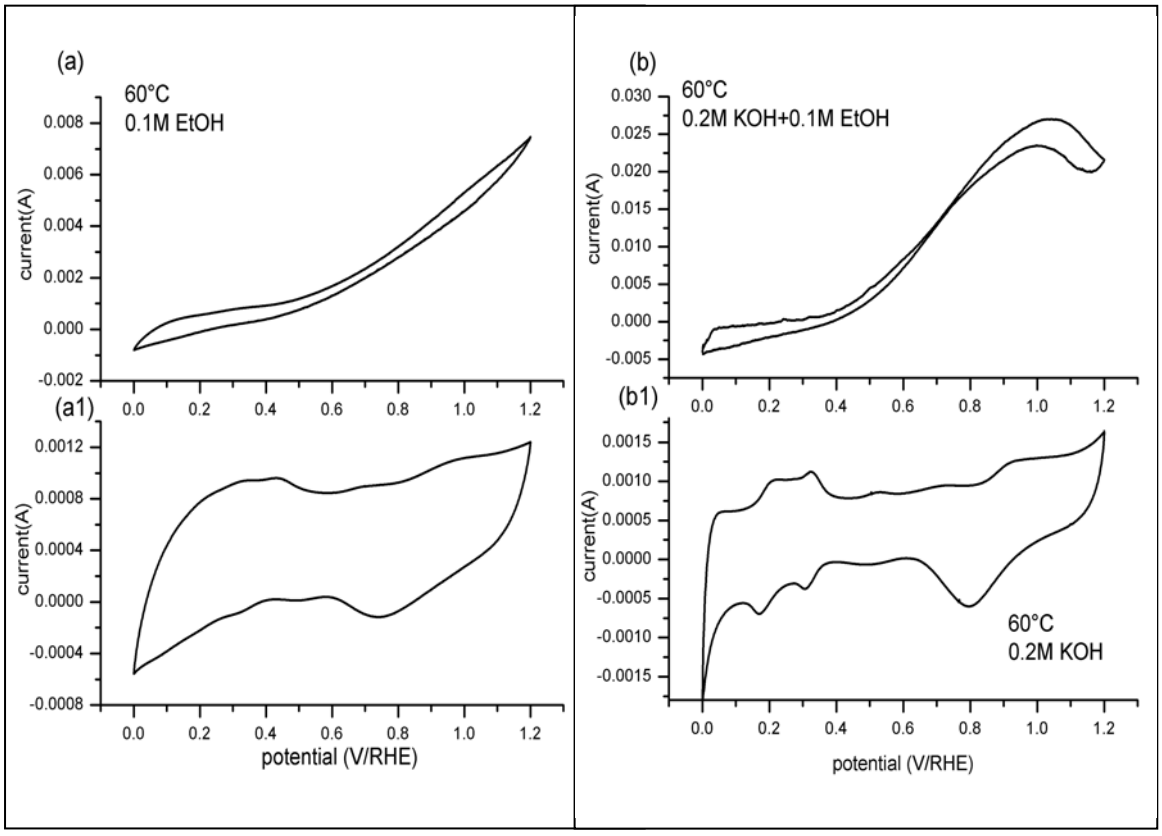

Figure 4.22. CV for the alkaline MEA are shown without KOH (a) with KOH (b) in the anolyte.

The Figure 4.22(a) also shows the polarization curve with 0.1M EtOH as anolyte and 1 bar abs H_2 pressure at cathode which works a counter and reference both. Figure 4.22(b) shows the CV with 0.2M KOH as anolyte. This cyclic voltammogram shows all standard features of Pt. Figure 4.22(b) upper part shows the polarization curve for a half cell with 0.2M KOH + 0.1M EtOH as anolyte and H_2 at cathode. The faradaic current in this case is higher. This might be because of the better ionic contact between the catalyst particles and the membrane and also better ionic conductivity of the membrane itself in presence of KOH. The resistance of the MEA is measured by current -interrupt method. It was found that the resistance of the MEA decreased from 7 Ohm in presence of deionized water to 1 Ohm in presence of KOH.

4.2.3 Electrochemical active area measurement by CO stripping

The electrochemically active area available in the anode catalyst layer of the MEA is determined with the CO stripping technique. CO is adsorbed on to Pt sites at 0 V/DHE, by flowing CO saturated water through the anode. CO is removed from the solution phase by purging anode with argon-bubbled deionized water. Then CO stripping is done. The CO stripping cyclic voltammogram performed at 60°C is shown below. It is noticeable that the CO stripping peak is very broad in comparison to a CO stripping peak in an acidic MEA with Pt anode. Also the onset of CO oxidation in the alkaline MEA, is negative shifted in comparison to an acidic membrane based MEA with Pt electrode. The CO stripping charge is estimated by integrating the area under the CO stripping peak. CO stripping charge is shown on the CO stripping graphs, which is directly proportional to the real electrochemical active area by a conversion factor of 420μC/cm². It has been found earlier that the electrochemical active area available in a catalyst layer is the one of the main determinant of the CCE (CO_2 current efficiency) in case of ethanol oxidation reaction. In this paper we will then compare the CCE of two MEAs, acidic and alkaline with platinum as catalyst, with approximately similar electrochemical active areas.

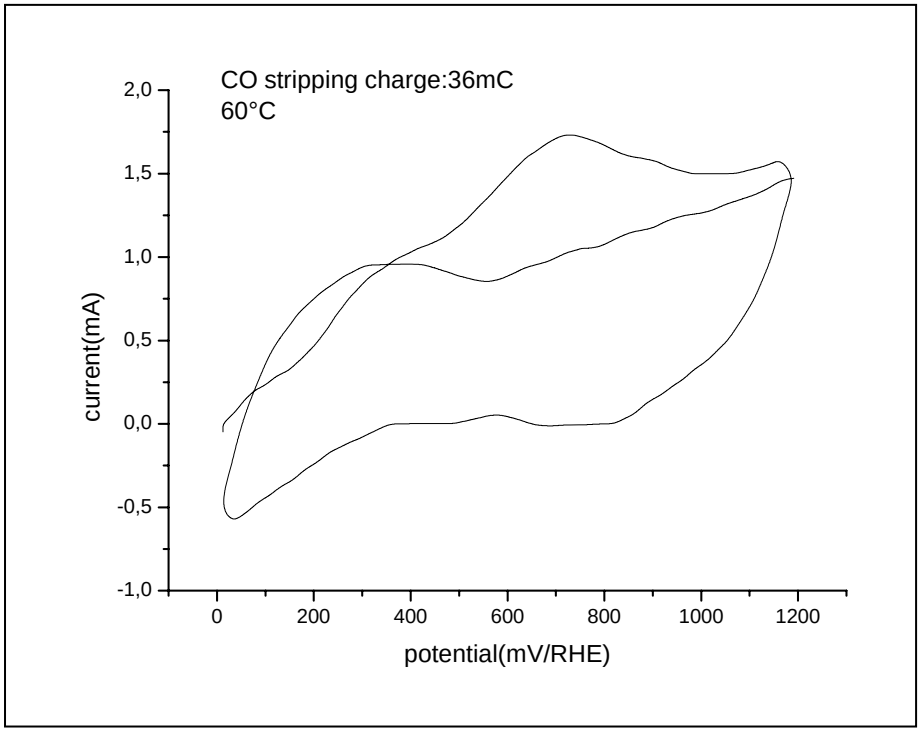

Figure 4.23. CO stripping CV for the alkaline MEA.

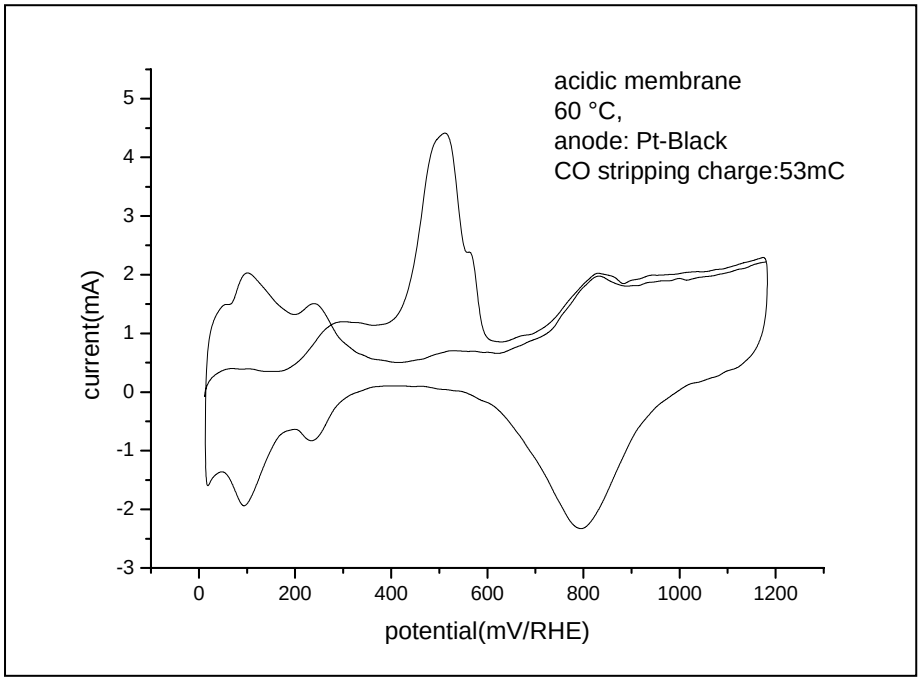

Figure 4.24. CO stripping CV for the acidic MEA.

4.2.4 DEMS measurement with CO bulk oxidation and ethanol oxidation

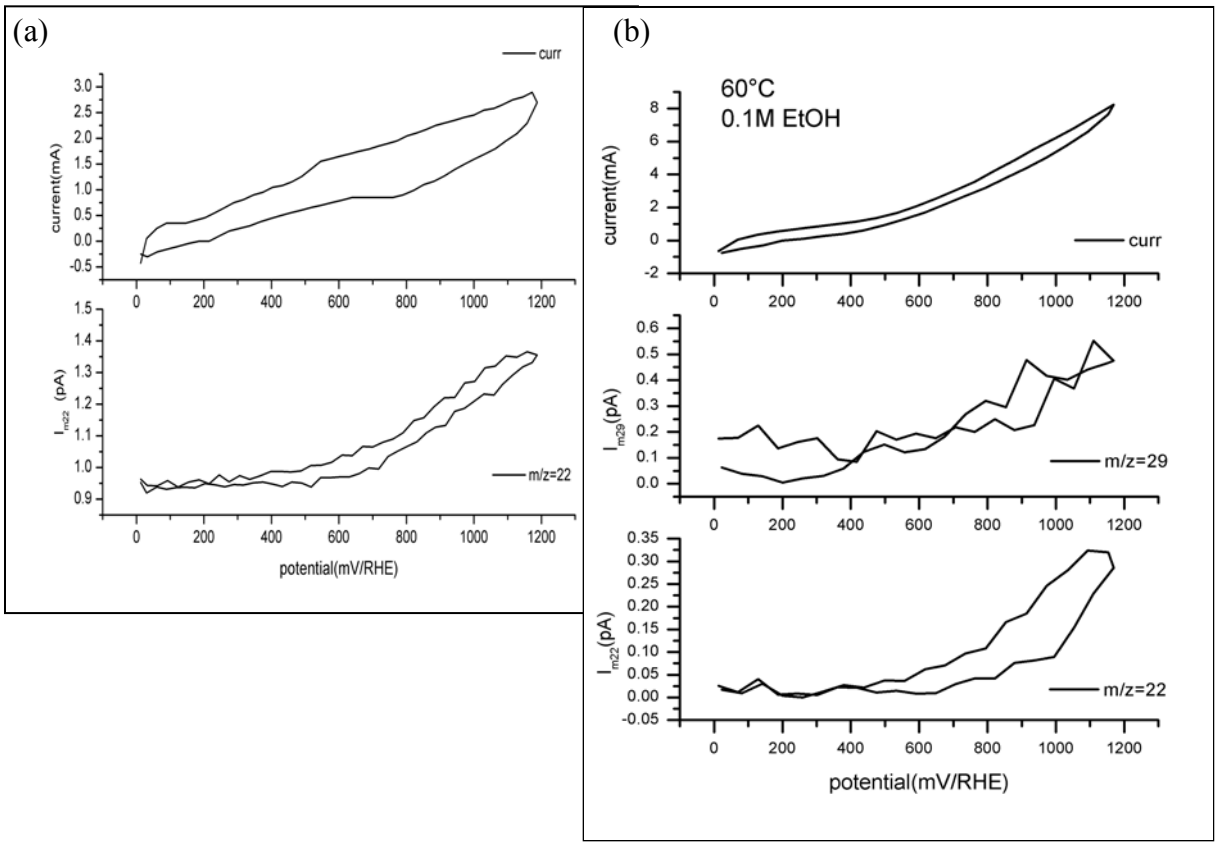

Figure 4.25. (a)CV and MSCV for bulk CO oxidation (b) CV and MSCV for ethanol oxidation for the alkaline MEA.

The Mass spectrometer cyclic voltammograms (MSCV) were measured with the alkaline MEA, with CO saturated water as anolyte, to check for the observablity of CO_2 and m/z = 22 signal. As can be seen in Figure 4.25(a) the m/z =22 is prominently observable. Also the effect of high membrane ionic resistance is visible in the shape of the CV. The Figure 4.25(b) shows the MSCVs with 0.1M EtOH as anolyte. The volatile by-product acetaldehyde was observed at m/z = 29 and the CO_2 was observed at m/z = 22. Both the MSCVs follows the faradaic current, although the signal of m/z = 29 is weak. But quantitative estimation is performed for CO_2 using appropriate calibration process. The calculation of CO_2 current efficiency for ethanol oxidation reaction in alkaline MEA with Pt anode is presented in next section.

4.2.5 CO_2 current efficiency for ethanol oxidation reaction

For CO_2 current efficiency estimation, potentiostatic bulk oxidation was performed at different potentials. Figure 4.26 graph shows potential, current and m/z = 22 signals as a function of time. The active area in the MEA is small, and the ionic resistance of the membrane is very high.

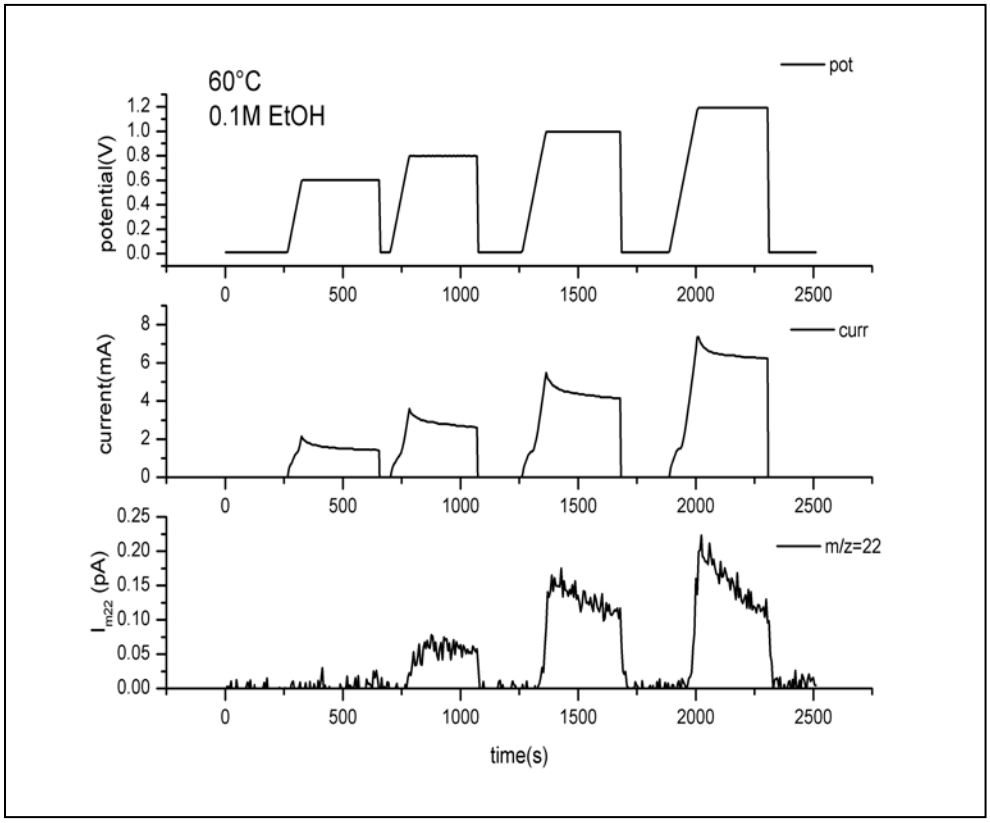

Figure 4.26. Potentiostatic bulk oxidation of ethanol at different potentials. The corresponding m/z = 22 signal is also shown.

That's why the over potentials needed for any appreciable current are high. It is noticeable that the CO_2 signal (m/z = 22) is not visible for 0.6V, since the faradaic current is small (< 2mA), and also because even if CO_2 is formed, it is below the detection limit of our DEMS-setup. After 0.8 V faradaic currents are higher and the CO_2 signal is strong. Figure 4.27 shows CO_2 current efficiency at different potentials for alkaline MEAs with Pt anode and an acidic MEA also with Pt anode. The conditions for both MEAs were same at 60 °C temperature and 0.1M EtOH as anolyte. The electrochemically active area (ECA) in both types of MEAs was estimated with the CO stripping technique. For the alkaline MEA1 Pt anode the ECA was estimated to be 85cm² (CO stripping charge: 36mC and Conversion factor: 420μC/cm²). For the acidic MEA the ECA in anode side was estimated to be 123 cm² (CO stripping charge: 52mC and Conversion factor: 420μC/cm²).

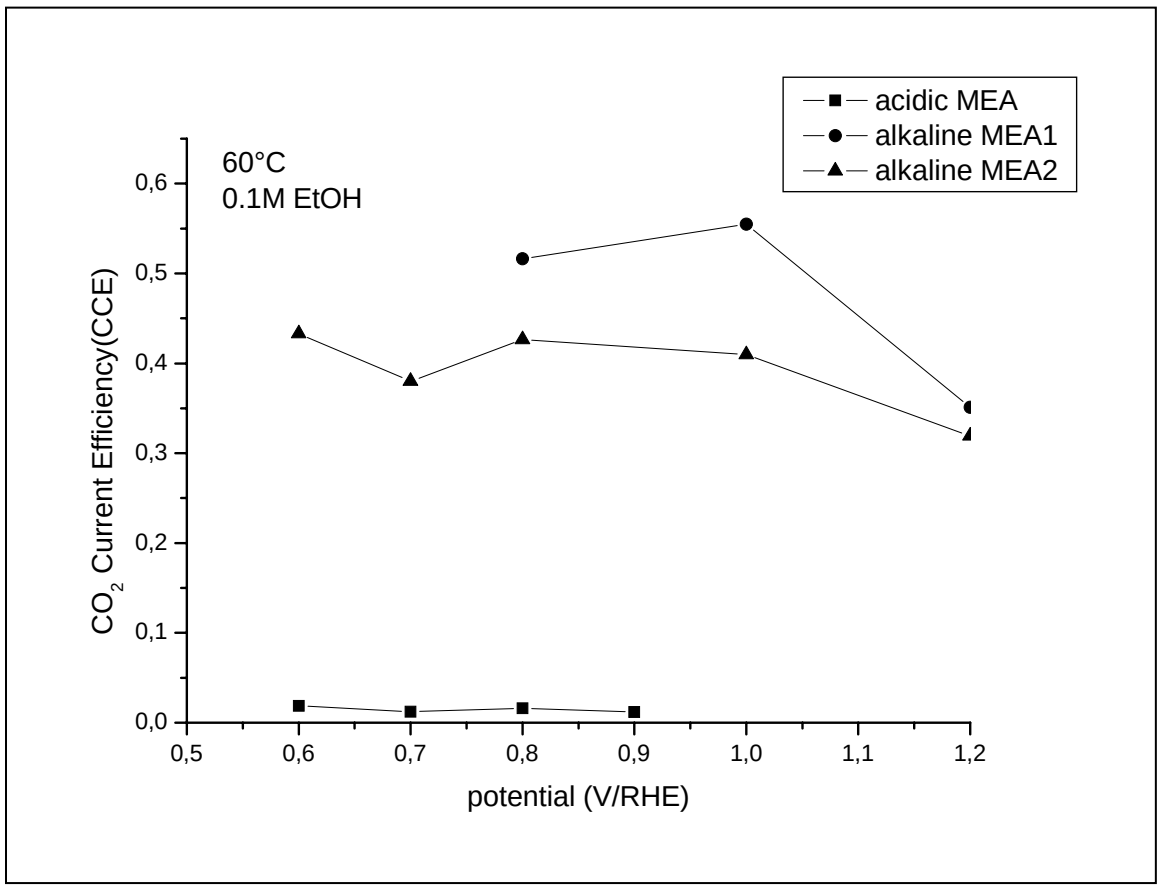

Figure 4.27. Comparison between the acidic and alkaline MEAs with Pt as catalyst, for CO_2 current efficiency at 60°C.

The comparison of these two MEAs with similar ECAs in anode side, from CO_2 current efficiency perspective throws up interesting insights about the mechanism of ethanol

oxidation in alkaline medium membrane. The CCE in case of alkaline MEA is very high. For example at 0.8V, alkaline MEA Pt anode shows a CCE of around 55%, but the acidic MEA Pt anode shows only around 2%. This might be a qualitative indication that the C-C bond scission rates in alkaline media are significantly higher than the acid media. Our unoptimized alkaline MEA has low ECA and higher ionic resistance. Because of this the potential range in which we could see the noticeable amount of CO_2 is high potential range. Although higher ECA and lower ion resistance is easily achievable with the addition of KOH in anolyte as is done in alkaline fuel cells. All solid alkaline fuel cells with alkaline polymer electrolyte membranes and no aqueous alkaline electrolyte has also been demonstrated[97]. In our case also no aqueous alkaline electrolyte was used. The electrochemical reaction takes place at the interface between Pt catalyst and solid alkaline electrolyte. So one can possibly extend the insights obtained into ethanol oxidation reaction in case of all solid alkaline MEA to alkaline MEAs with aqueous KOH at anode side also, as the pH and related conditions in both cases would be similar. Figure 4.27 also shows the CCE data for a second alkaline MEA, shown as alkaline MEA2. The ECA value for this MEA is not available.

5. Discussion

5.1 Performance of DMFC anode catalyst layer with increasing thickness

In chapter 3.1 we discussed the effect of catalyst layer thickness on the performance of DMFC anode in a half-cell. The linear increase in current with increasing catalyst loading, at a particular polarization potential, is highly desirable to achieve high current densities and thus higher power densities in DMFCs. But after a certain threshold catalyst layer thickness, the current densities show saturation behavior with increasing catalyst layer thickness. The current density does not increase any further with increasing catalyst loading. To better understand this phenomena, we measured electrochemical active area in the catalyst layer with different catalyst layer thicknesses or catalyst loadings. The electrochemical active area is measured using standard CO stripping technique. The electrochemically active area was found to increase linearly with increasing catalyst loading or increasing catalyst layer thickness. This means that even for very thick layers (200μm), none of the catalyst particle becomes inactive. Electrochemical area was also measured with methanol adsorption at non-

oxidizing potentials. The methanol adsorption and consequent dehydrogenation steps also lead to a final stably absorbed CO like species. The electrochemically active area measured with methanol adsorption also showed linear increase with increasing catalyst loading. This indicates that in thick layers all catalyst is available for methanol adsorption and also that methanol can reach into the whole catalyst layer. These results are easily understandable if one takes into account how ohmic resistance across the catalyst layer affects the determination of electrochemically active area using CO stripping technique or methanol adsorbate stripping. The catalyst layer has certain protonic and electronic conductivity. But the protonic and electronic resistance of the catalyst layer does not affect at all the amount of CO stripping charge which flows from one time oxidation of CO monolayer. The calculation of CO stripping charge is completely independent of any resistance. But when there is continuous oxidation of methanol then currents are high and so are overpotential losses in catalyst layer caused by the ohmic resistance. These losses are proportional to currents flowing in the catalyst layer. It was found that in low current regime the currents at any potential increase linearly with increasing catalyst layer thickness or catalyst loading. This linear behavior can be clearly seen at lower potential or lower temperature where the currents are small. But in high current regime the "saturation effect" is observed. The catalyst layers, which are pressed at 8-10 MPa pressure, which is also our MEA hot pressing pressure, shows an electrical conductivity of around 0.25S/cm. This is not very good electrical conductivity, but still much better in comparison to the typical proton conductivity of the catalyst layers which is normally around 5-15mS/cm, depending on volume fraction of electrolyte phase in catalyst layer. Since the currents in electron conducting phase and electrolyte phase are same, for first approximate calculations one can neglect the ohmic losses in the electronic phase as it has at least order of magnitude high conductivity. Thus neglecting the mass transport losses and ohmic losses in electron conducting phase of the catalyst layer, a simple model of the anode catalyst layer was proposed, which takes into account only the ohmic losses in proton conducting phase of the catalyst layer. Simple calculation for current at particular potential as a function of catalyst layer thickness was made. The calculated curve clearly shows a saturation behavior at higher catalyst layer thickness. Thus it is clear that the low proton conductivity in the catalyst layers is one of the main factors responsible for poor performance of thicker catalyst layers. Similar results were also reported in literature for cathode catalyst layer of a H_2/air fuel cell MEA[106]. In the proposed model since the effect of mass transport and ohmic losses in electron conducting phase were neglected, it would give an upper limit for current densities as a function of catalyst layer thickness. When one considers the influence of the mass transport

and ohmic losses in electron conducting phase also, the predicted performance will be even lower. But the qualitative matching of the experimental and simulated data supports the argument that the assumption of neglecting mass transport and ohmic losses in electron conducting phase were reasonably correct. The errors in the model might come because of assumed values of the proton conductivity of catalyst layer, which is taken from literature. Finally in our experimental conditions proton conductivity of the thick catalyst layers seems to be the major factor responsible for saturation behavior. By increasing the nafion vol% in the catalyst layer, proton conductivity achievable may not be enough. An option could be, to use liquid acid electrolyte.

5.2 DMFC anode catalyst with varying carbon support porosity

In this study we introduced an approach to investigate the influence of specific surface area of carbon supports on the performance of the DMFC anode catalysts by keeping PtRu dispersion constant. Differences in the intrinsic catalytic activities of two DMFC anode catalysts incorporated in MEAs with significantly different thicknesses of the catalyst layer may be overshadowed by the influence of mass transport. Therefore, in order to make a meaningful comparison between different catalysts, we kept the anode catalyst layer thickness nearly constant by fixing the amount of catalyst powder (metal + carbon) per cm^2 of the electrode geometrical area constant. We utilize novel catalysts for an anode of a DMFC: PtRu nanoparticles supported on Sibunit carbons. Specific surface areas of carbon materials are varied systematically in a wide range from 6 m^2g^{-1} to 415 m^2g^{-1}. Low surface area carbon supported catalysts show superior mass specific activities, exceeding that of Vulcan-XC72 supported 20%PtRu catalyst by nearly a factor of 3. To understand these results, the metal catalyst utilization factor was estimated for catalyst incorporated into a MEA. The metal catalyst utilization factor is defined as the ratio of exposed metal area in powder form measured by CO gas phase chemisorption to the electrochemical active area (ECA) measured by CO stripping technique after incorporating the catalyst into a catalyst layer of a MEA. The metal catalyst utilization in a MEA for low surface area sibunit carbons supported catalyst is close to factor of two higher than Vulcan supported catalyst. The trend of decreasing metal catalyst utilization with an increasing support surface area can be explained on the basis of an increased incompatibility between the morphological structure of carbon support and Nafion® micelles. In CO chemisorption all the metal sites, which are exposed to the surface

of nanoparticles and adsorb CO, are counted, since CO gas can reach every nanoparticle regardless its location (unless its surface is blocked by the pore walls or carbonaceous deposits [123]. However, this is not the case in an electrochemical CO stripping experiment from a PtRu/C catalyst incorporated in a MEA. The latter provides information only on the amount of PtRu sites, which are in contact with the Nafion® ionomer and thus can participate in the electrochemical process. As the surface area of carbon supports increases, more small pores with d <20 nm are formed. It has been reported in literature [53, 59], Nafion® ionomer has rather large (>40nm) micelles, which do not penetrate in carbon pores of smaller diameter. The results of this work strongly suggest that an increase of the contribution of pores with d<20 nm results in a considerable decrease of the metal utilization factor, thus providing a qualitative proof for the data reported by Uchida et al. [59]. Thus, low surface area carbon materials, featuring relatively small contribution of pores below 20 nm, favor high catalyst utilization in MEAs of fuel cells with polymer electrolyte. Specific activity is also found to be higher for low surface area sibunit carbon supported catalyst. A probable reason for this behavior may be better reactant and product transportation in porous structure of low surface area carbons, as the average pore diameter in low surface area carbons is higher.

The same series of catalyst was also investigated for oxygen reduction reaction. The activity of these catalysts for oxygen reduction reaction was measured also in MEAs with high loading Pt electrode as reference and counter electrode. Partially humidified hydrogen and oxygen were used as anode and cathode feeds. Stable U-I curves were achieved in room temperature conditions. Again the low surface area sibunit carbon supported catalysts were found to be more active. The mass activity for ORR in case of low surface area carbon supported catalysts is higher by a factor of around 6, than a Vulcan supported catalyst. The sibunit series of catalyst was also investigated in an electrochemical cell, to gain more insight into the functioning of these catalysts. In the electrochemical cell with aqueous acid as electrolyte, the carbon support surface area dependence on activity of the catalyst is not present until 290m^2/g S_{BET}. All catalysts with carbon support surface area up to 290m^2/g showed similar activity. The catalyst with highest surface area carbon support (sib619P) was found to be least active. In an electrochemical cell experiments the catalyst loading and catalyst layer thickness is very small and the aqueous electrolyte can reach all pores. So the catalyst utilization is almost 100% for all catalysts. This might explain independence of activity on S_{BET} up to 290m^2/g in electrochemical cell experiments. Finally higher mass

activity of low surface area carbon supported catalyst for methanol oxidation and oxygen reduction can thus be attributed to (i) high PtRu surface utilization, and (ii) facilitated diffusion in macropores. This work is only a step on the way to design an optimized support for PEMFCs and DMFCs. However, it shows immense potentialities of support optimization in the improvement of low temperature fuel cell electrocatalysts. More work is needed in order to find out the (i) optimum pore structure and (ii) texture of carbon supports and to explore how surface area influences long term stability of fuel cell catalysts.

It is also important to note that the catalysts investigated in this study had a metal percentage of 10 and 20%. It was necessary to choose such low loading to maintain optimum particle size and also to maintain the particle size nearly constant for different catalysts, to exclude the particle size effects in mass activity while evaluating the impact of carbon support porosity on the activity of catalyst. Because of low metal percentage in these catalysts, their usage in practical DMFCs is less likely. Generally DMFCs requires higher metal loading on anode side for achieving practical current densities. For such loadings the catalyst layer thickness would be much higher for these low metal percentage catalyst as they have bigger fraction of low density carbon. At higher catalyst layer thickness, the positive effect of higher intrinsic activity of these catalysts will be completely overshadowed by the strongly negative effects associated with thicker catalyst layer. Catalyst layer thickness effects have been discussed in more details in section 3.1.

But these catalysts might be applicable for H_2/air PEMFCs, as the typical metal loading in PEMFCs is also very low. The catalyst loading and catalyst layer thickness in PEMFC is small and thus bad effects of catalyst layer thickness will be very weak in PEMFC anode or cathode. Thus one can utilize the effect of higher intrinsic activity in PEMFC case.

5.3 Ethanol electrooxidation studied by DEMS

5.3.1 DEMS on acidic media MEAs

Ethanol oxidation was studied systematically using platinum based catalysts in membrane electrode assembly form. The electrolyte media in these MEAs is acidic. The final product of ethanol oxidation process, carbon dioxide, was monitored and quantified as a function of different parameters like potential, temperature, concentration, catalyst loading or layer

thickness and flow rate of the anolyte. CO_2 current efficiency for ethanol oxidation reaction using Pt/C catalyst was found to increase with increasing temperature of operation. CO_2 current efficiency depends strongly on the concentration of EtOH, decreasing with the increase of the latter. At higher ethanol concentration CO_2 becomes a minority product with acetaldehyde taking the lead. The acetaldehyde yield decreases with decrease in concentration and increase in temperature. Acetaldehyde is a stable intermediate, which is quite active for further oxidation if it can readsorb. But with increase in ethanol concentration, desorbed acetaldehyde molecules will find it more difficult to find a Pt site for readsorption and thus oxidizing further. Catalyst loading and thus catalyst layer thickness strongly affects the completeness of EtOH oxidation reaction. With increasing catalyst loading, CO_2 current efficiency increases. In this respect the fuel cell behaves a chemical reactor, where the final product distribution of a particular reaction is determined by the available active area and residence time of the reactant.

The increasing catalyst layer thickness will result in increasing residence time of the reactant. Also the increasing catalyst loading gives linearly increasing electrochemically active area. These two factors namely active area and residence time are thus responsible for the increase in CO_2 current efficiency with increasing catalyst loading. The residence time of the reactant in a fuel cell anode compartment can also be varied by changing the anolyte flow rates. Expectedly the CO_2 current efficiency was found to decrease with increasing anolyte flow rate as the residence time of reactants in the catalyst layer goes down with increasing flow rate. CO_2 current efficiency decreases with increasing potential >0.6V for ethanol oxidation. But it is almost independent of potential in case of EG oxidation. Activation energy for overall ethanol oxidation reaction is 31kJ/Mol, and it is 25 kJ/Mol for EG oxidation. The activation energy for CO_2 formation by EtOH and EG oxidation is nearly same, which indicates similarities in the mechanism of CO_2 formation in both cases. Three catalysts namely Pt/C, PtSn(7:3)/C and PtRu(1:1)/C were compared for CO_2 current efficiency under similar conditions. In these experiments Pt/C and PtSn/C were found to have higher CO_2 current efficiency but the case for PtRu/C catalyst was completely different. The PtRu/C catalyst showed very low CO_2 current efficiency. Although the faradaic currents and onset potential for PtRu/C catalyst were comparable to PtSn/C, but CO_2 current efficiency was very low in comparison. This might be explained by the fact that high amount of Ru in PtRu/C catalyst, lowers C-C bond scission rate and promotes partial oxidation of ethanol to acetic acid, by supplying oxygenated species which Ru is known to adsorb at much lower potentials. Of the

intermediates products acetaldehyde and acetic acid, acetaldehyde was found to quite active for further oxidation, but acetic acid seems to be a final product, as it is hard to oxidize any further.

5.3.2 Ethanol oxidation mechanism in fuel cell conditions

The CO_2 current efficiency for ethanol oxidation reaction is influenced by many factors related to fuel cell operation. The main intermediate/byproducts of ethanol oxidation reaction are acetaldehyde and acetic acid. To understand if acetaldehyde and acetic acid can be oxidized further, separate experiments were performed with acetaldehyde and acetic acid as the anolyte. Acetaldehyde oxidizes readily with very high CCE. But acetic acid is found to be quite resistant to oxidation on Pt and PtSn based catalysts. So acetic acid seems to be the final product. Taking into account these results, we can present the ethanol oxidation reaction mechanism in fuel cell conditions, as shown in Figure 5.1. The CCE values indicated in Figure 5.1 are for an anode metal catalyst loading of 8mg/cm^2 using 40%Pt/C and 90°C and 0.1M ethanol concentration. Starting from ethanol, there are two pathways towards the formation of CO_2. First is by direct dissociative adsorption of ethanol and then further oxidation of these adsorbed species. Second is by formation of acetaldehyde and then dissociative adsorption of acetaldehyde, and then further oxidation of the adsorbed species thus formed. These two pathways together contribute to 75% of CO_2 current efficiency. Remaining faradaic current results either from two electron transfer process of partial oxidation of ethanol to acetaldehyde, or from four electron transfer process of partial oxidation of ethanol to acetic acid via acetaldehyde. Some fraction of acetaldehyde flows out as a dissolved stable intermediate. Since acetic acid is difficult to oxidize any further, it flows out as a final product. Figure 5.1 also shows the CCE for acetaldehyde as the starting molecule. In the fuel cell conditions acetaldehyde oxidation reaction results in 86% CO_2 current efficiency. Rest of the faradaic current, results from acetic acid formation. The obtained results about CO_2 current efficiency for ethanol oxidation variation with parameters like potential of oxidation, temperature and concentration, will help in the characterization of the ethanol (or other fuels with C-C bond) oxidation catalysts under real fuel cell conditions.

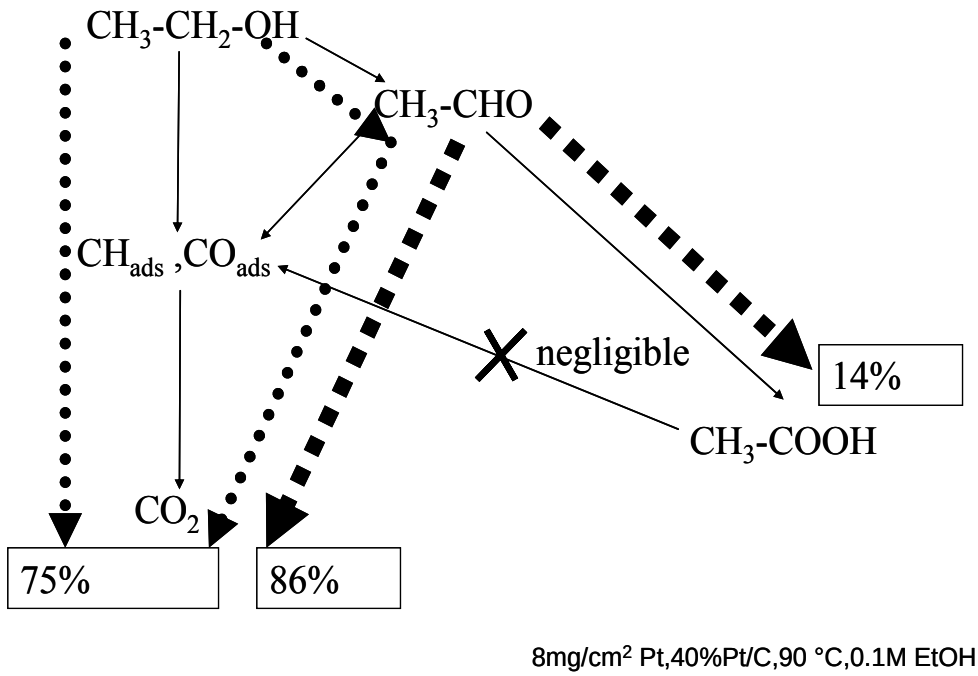

Figure 5.1. Ethanol oxidation reaction mechanism scheme in fuel cell conditions.

5.3.3 Ethanol electrooxidation studied by DEMS in alkaline media MEAs

The DEMS measurements performed with the all solid alkaline MEA indicates that the in case of alkaline media ethanol undergoes significantly more complete electro oxidation to CO_2 than in case of acidic MEA with same Pt anode. The CO_2 current efficiency can be compared for acidic and alkaline MEA with similar electrochemical active area on the anode side. It is important to compare keeping similar ECA, as CO_2 current efficiency for ethanol oxidation reaction increases with increasing electrochemically active area available in the catalyst layer. This has been found earlier in experiment with acidic MEAs. The CCE estimated in case of alkaline MEA with Pt anode is around 55% at 0.8V/DHE, 60°C and 0.1M EtOH. But in same conditions acidic MEA shows only 3% CCE. This indicates that the C-C bond scission rates are much higher in alkaline media. But how exactly the mechanism of ethanol oxidation in alkaline media is, is not clearly known. The fact that CO_2 will form carbonates in presence of aqueous alkaline electrolyte make it difficult to study ethanol oxidation in FTIR or model DEMS systems. The polymer alkaline electrolyte as used in this study for making alkaline MEAs, provides an important opportunity to observe CO_2 produced during ethanol oxidation reaction using DEMS system.

5.3.2 Importance of DEMS

The extent of completeness of ethanol oxidation or CO_2 current efficiency under real fuel cell conditions can be very different from the results obtained in model DEMS. This fact emphasizes the importance of fuel cell DEMS measurements. Catalysts like Pt-Sn[89-93] has been reported to be better for ethanol oxidation than pure Pt based catalysts. Comparative fuel cell DEMS measurements with such a catalyst will help in understanding the basic reason for their better activity for ethanol oxidation. The Fuel cell DEMS measurement can determine if the higher activity of such catalysts is because of more effective C-C bond breaking (and thus complete oxidation) or just faster partial oxidation rates, which one can not understand from faradic current measurement alone. As has been reported earlier PtRu(1:1) catalyst exhibits good activity for ethanol oxidation reaction almost similar to PtSn catalyst. But when analyzed through DEMS it was found that PtRu catalysts shows very little CO_2 current efficiency and almost all the faradaic current stems from the partial oxidation reactions to acetaldehyde or acetic acid. These findings further emphasize the importance of DEMS technique in characterization of electrocatalysts.

5.3.3 Electro catalysis vs. heterogeneous catalysis debate

Oxidation of alcohols to carbon dioxide and protons takes place at anode in case of electro catalytic oxidation. Another approach is to thermally reform the alcohols to CO_2 and H_2 through an endothermic reaction and then use the produced H_2 for fuel cell. For example Methanol is known to reform at a temperature of 200-300°C and similarly ethanol is known to reform at 500-600°C. Now it is possible that reformation process also takes place at temperatures in 100 °C range but with an extremely slow rate. This would imply existence of another heterogeneous non-electrochemical pathway for alcohol oxidation other than the standard electrochemical pathway. But to be able to prove the existence of this pathway one will have to observe production of CO_2 and H_2 without application of any electrochemical potential. This is bit difficult to see with the DEMS as the signals without application of any potential are considered as the background signals and only differential mass signals generated by application of potential are possible to measure and quantify. But with techniques like gas-chromatography, it would be possible to analyze and quantify all gases formed in a heterogeneous pathway. In case of DEMS technique whenever any organic fuel enters the MS chamber, the CO_2 background always shifts up. This shift might be because of CO_2 formed by heterogeneous oxidation of alcohol with traces of oxygen on Pt catalyst or due to some reaction taking place in MS chamber with traces of oxygen there. This effect makes it

difficult to quantify absolute amount of CO_2 and thus whatever amount of CO_2 is being formed by heterogeneous pathway is not observable by DEMS. Although many groups have studied methanol and ethanol oxidation using gas chromatography but observed only stable intermediates like formaldehyde, methyl formate, formic acid in case of methanol oxidation and acetaldehyde, ethane, methane, acetic acid, ethyl acetate etc in case of ethanol oxidation. The products of heterogeneous reformation reaction of alcohols in electrochemical conditions e.g. CO_2 and H_2 have not been observed, at least up to their present detection limits. This might indicate that heterogeneous reformation reaction of alcohols in electrochemical conditions takes place at very slow reaction rates which makes it almost undetectable.

5.3.4 Overall judgment on direct alcohol fuel cells

Direct alcohol fuel cells provide the opportunity to use liquid alcohols instead of hydrogen as fuels. The use of liquid fuels entails high energy density storage and convenient handling. Also direct oxidation of fuels implies that the high temperature thermal fuel reformers are not required, resulting in simplification of the fuel cell system. Despite these important advantages direct alcohol fuel cells are also not without problems. The direct electrochemical oxidation of alcohols requires noble metal catalysts in relatively high amounts. Further more the low activity of these noble metal catalysts results in overpotential losses which lowers the overall energy conversion efficiency. In last two decades a lot of research has been conducted for finding catalysts for methanol oxidation reaction and PtRu alloys has been found to be the standard catalysts for methanol oxidation. Methanol being smallest alcohol without any C-C bond is readily oxidizable with reasonable reaction rates but next higher alcohol; ethanol is much harder to oxidize and even harder to oxidize completely to CO_2. The catalysts known until now for ethanol oxidation reaction exhibits relatively low reaction rates and also incomplete oxidation of ethanol. Thus better catalysts are needed for direct alcohol fuel cells. But nevertheless in present status one can optimize the operating conditions of the fuel cells to achieve faster and complete oxidation of alcohols. For example as has been discussed earlier the completeness of oxidation depends on the temperature, concentration and catalyst layer thickness. High temperature, lower concentration and higher catalyst layer thickness resulted in faster and more complete oxidation of ethanol. Thus in present stage these findings can be used in improving the operation of the direct alcohol fuels cells.

6. Summary

In section 3.2 are described the results of the investigation of the effect of the carbon support surface area on the activity of the carbon supported catalysts for methanol oxidation reaction. The activity of the catalysts was measured in real fuel cell conditions by incorporating the catalysts into a MEA (membrane electrode assembly) and also in model electrochemical cell. To isolate the effect of carbon support surface area on the methanol oxidation activity, other parameters like thickness of the catalyst layer, particle size which can otherwise affect the measured activity strongly, were kept nearly same for all the samples. In MEA form, the catalysts with lower carbon support surface area were found to be more active than standard Vulcan supported catalysts nearly by a factor of 3. The metal utilization factor for low surface area carbon supported catalyst was found to be much higher than higher surface area carbon supported catalysts. Higher metal utilization for low surface area carbon supported catalysts was attributed to the fact that low surface area carbon supports have larger pores. This makes it easier for the nafion micelles, which can not go into pores below 40nm size, to penetrate into the carbon pores and make electrolyte contact with the metal catalyst particle residing there. But for the higher surface area carbon support, with much smaller average pore size, the situation is different. The specific activity of the low surface area carbon supported catalysts was also found to be higher than high surface area carbon supported catalyst. This effect can be attributed to faster mass transport in bigger pores of the low surface area carbons. Thus higher metal utilization factor and faster mass transport through bigger pores in case of low surface area carbon supported catalyst are the factors responsible for their high activity for methanol oxidation.

All the catalysts used in this study were with low metal % e.g. 10% and 20% metal supported on sibunit carbons. In practical applications the catalyst loading required for any reasonable current density are generally high. But the high catalyst loading using low metal % catalysts would result in thick catalyst layers. As the thickness of the catalyst layer increases many other effects comes into play. So as discussed in section 3.1, the effect of the thickness of the catalyst layer on the current density or performance of the catalyst layer was investigated. MEAs with different catalyst layer thickness or catalyst loading were prepared and methanol oxidation current was measured. The current density increases linearly until certain catalyst loading or catalyst layer thickness, and then after that saturation effect shows up. Although in low current range the current density still increase linearly with increasing catalyst loading,

but in higher current range saturation effect is clearly visible. Saturation effect means that increase in catalyst loading does not bring any further increase in current density. To understand this saturation effect, the active area was measured for catalyst layers with increasing thickness so as to find out if catalyst still remains active or not, when catalyst layer thickness reaches around 200microns. CO stripping technique was used for measuring active area. It was found that the active area increases linearly with increasing catalyst layer thickness. Active area was also measured using methanol adsorption, which also gave similar results as CO stripping. For gaining further understanding of the saturation effect, a simple catalyst layer model is proposed. This model neglects the effect of mass transport and also the ohmic losses in electron conducting media in the catalyst layer. Model only takes into account the effect of proton conductivity of the catalyst layer on its performance for methanol oxidation. The proton conductivity values were taken from literature. Model calculation also shows a saturation behavior which matches quite well with the experimental data. Model also shows linear increase in current density with increasing catalyst loading in low current range. This simple model shows that proton conductivity might be the most important factor responsible for the saturation behavior.

In section 4.1 are discussed the results of the investigation performed for understanding ethanol oxidation reaction mechanism in fuel cell conditions using Fuel Cell DEMS technique. The desired final product of ethanol oxidation reaction, carbon dioxide CO_2, was observed and CO_2 current efficiency (CCE) was calculated for different set of parameters involved. Various parameters involved are potential of oxidation, temperature, concentration, and catalyst layer thickness or catalyst loading, electrochemical active area available in the catalyst layer, anolyte flow rate and intrinsic nature of the catalyst. The CO_2 current efficiency increases with increasing temperature and decreases with increasing concentration. But the catalyst layer thickness and thus also the electrochemical active area influence the CCE in very prominent way. CCE increases with increasing catalyst loading from about 10% for 0.2mg/cm^2 to about 80% for 8mg/cm^2 catalyst loading at 90°C and 0.1M Ethanol and 40%Pt/C catalyst. The dependence of the CCE on the catalyst layer thickness and electrochemical active area indicates that fuel cell anode behaves like a chemical reactor where residence time of the reactants and active area decides the final product distribution. The residence time of the reactant can also be varied by varying the anolyte flow rate. CCE was found to decrease with increasing flow rate. The intrinsic nature of the catalyst has an important influence in complete oxidation of ethanol. Accordingly PtSn(7:3) and Pt based

catalyst showed much higher CCE the PtRu(1:1) catalyst. The byproduct of ethanol oxidation reaction acetaldehyde and acetic acid were also investigated for direct oxidation. Acetaldehyde was found to very active for further oxidation with a very high CCE. But acetic acid was found to be very resistant for further oxidation with PtSn and Pt catalysts.

All the above mentioned results were obtained using acidic media membranes. Alkaline media offers kinetic advantages for ethanol oxidation reaction. But availability and chemical stability of alkaline media membranes were unresolved issues until few years ago. Newly available polymer alkaline media membranes made it possible to make MEAs with them and investigate ethanol oxidation. In section 4.2 are discussed some results about CCE measurement with alkaline media MEA and unsupported Pt as catalyst. In this preliminary work the CCE were compared for acidic and alkaline MEAs with similar active area in the anode electrocatalyst layer. These results show a much higher CCE for alkaline media MEAs in comparison to acidic MEAs under same conditions. There is no data available in literature for CCE in model DEMS systems with alkaline media as CO_2 is simply not observable when one uses liquid alkaline electrolyte. CO_2 reacts to form soluble carbonates or bicarbonates. Our result of comparatively high CCE in alkaline media MEAs indicates different mechanism of ethanol oxidation in alkaline media.

7. List of used symbols and abbreviations

PEMFC Polymer electrolyte membrane fuel cell

DMFC Direct methanol fuel cell

CV Cyclic voltammogram

MSCV Mass signal cyclic voltammogram

U^0_a Anode potential

U^0_c Cathode potential

ΔU^0_{cell} Cell voltage

MEA Membrane electrode assembly

i_{sp}/A m^{-2} Specific activity

i_{mass}/A g^{-1} Mass activity

XRD X-Ray diffraction

TEM Tunneling electron microscope

GNF Graphitic nanofibers

BET Brunauer- Emmett-Teller

BJH Barrett-Joyner-Halenda

V_{mi} Micropore volume

CV Cyclic voltammogram

I-U Current voltage curves

S_{BET} Surface area determined by BET method

RHE Reversible hydrogen electrode

TSA Total surface area

EASA Electrochemical active surface area

α Catalyst utilization factor

MOR Methanol oxidation reaction

ORR Oxygen reduction reaction

DHE Dynamic hydrogen electrode

SSA Specific surface area

CL Catalyst layer

GDL Gas diffusion layer

FC-DEMS Fuel cell differential electrochemical mass spectroscopy

K_F^* Calibration factor

CCE CO_2 current efficiency

EOR Ethanol oxidation reaction

EGOR	Ethylene Glycol oxidation reaction
ECA	Electrochemical active area
EtOH	Ethanol
MeOH	Methanol
EG	Ethylene Glycol

8. Appendix A1

C++ program used for simulating the anode catalyst layer

```
#include <stdlib.h>
#include <stdio.h>
#include <string.h>
#include <math.h>

float   pot,pot1,pot2,protonres,a;
int     numberoflayers,i,j,n,l,k,p;
float   overpot[19],Icurr[19],Acurr[19];
FILE    *File1;
FILE    *File2;

void cal_current()
{  pot1 = overpot[i];
   Icurr[i]=((-330.99655)+(3.95498*pot1)-(0.01691*pot1*pot1)+(2.9868E-
5*pot1*pot1*pot1)-(1.71678E-8*pot1*pot1*pot1*pot1));
}

void cal_curr()
{ pot1 = overpot[j+1];
  Icurr[j+1]=((-330.99655)+(3.95498*pot1)-(0.01691*pot1*pot1)+(2.9868E-
5*pot1*pot1*pot1)-(1.71678E-8*pot1*pot1*pot1*pot1));
}

void cal_Acurr()
{k=0;
while(i>=k){
          a=0;
          l=k;
        while(i>=l){a=a+Icurr[l];
                        l++;
                }
          Acurr[k]=a;
          k++;
        }
}

void iterate()
{   n=0;
```

```
while(n<5){
 j=0;
while(i>j){
        overpot[j+1]=overpot[j]-Acurr[j]*protonres;         /*modify overpotential*/
        cal_curr();
        printf("\nIcurr=%f\t%f\t%f\t%f\t",Icurr[j+1],Icurr[j],Acurr[j],overpot[j+1]);
        cal_Acurr();                                    /*Acurr[j] updated */
        j++;
       }
        cal_Acurr();                                    /*Acurr[j] updated*/
        n++;
         }
}

void main ()
{
       printf("Please enter the potential at the GDL and CL interface(in mVs):");
       scanf("%f",&pot);
       printf("\nPlease enter the protonic resistance of one layer(in ohms):");
       scanf("%f",&protonres);
       printf("\nPlease enter the number of layers:");
       scanf("%d",&numberoflayers);

       Acurr[0]=0;
          overpot[0]=pot;
       printf("pot0=%f\n",overpot[0]);
       i=0;
            while(i<numberoflayers)
                  {
          cal_current();
          /*printf("\nIcurr=%f\t",Icurr[i]);*/
          cal_Acurr();

          if(i>=1){iterate();
                 }

          cal_Acurr();

             overpot[i+1]=overpot[i]-Acurr[i]*protonres;
          printf("i=%d\toverpot=%f\n",i,overpot[i]);

         /*  File1 = fopen ("curr.txt","a");
          fprintf (File1, "%d\t%f\t%f\n", 10*i,Icurr[0],Acurr[0]);
          fclose(File1);

          File2 = fopen ("pot.txt","a");
          fprintf (File2, "%d\t%f\n", 10*i,overpot[i]);
          fclose(File2);*/

          i++;
                  }
```

```
File1 = fopen ("curr.txt","a");
p=0;
while(p<numberoflayers){
        fprintf (File1, "\n%d\t%f\t%f\t%f\n", 10*p,Icurr[p],Acurr[p],overpot[p]);
        p++;      }

fclose(File1);}
```

9. References

[1] W. Vielstich, A. Lamm,H. A. Gasteiger, eds., Handbook of Fuel Cells, Vol. 1, John Wiley & Sons, 2002.

[2] L. Carrette, K.A. Friedrich,U. Stimming, CHEMPHYSCHEM 1 (2000) 162-193.

[3] M.P. Hogarth,G. A. Hards, Platinum Metal Rev. 40 (1996) 150.

[4] T. R. Ralph,M. P. Hogarth, Platinum Metal Rev. 46 (2002) 3.

[5] G. Hoogers, CRC Press LLC, Boca Raton, 2002.

[6] M. P. Hogarth,G. A. Hards, Platinum Metal Rev. 40 (1996) 150.

[7] J. Kerres, W. Zhang, L. Jörissen,V. Gogel, J. New Mater. Electrochem. Syst., 5 (2002) 97.

[8] N. Alonso-Vante and H. Tributsch, Nature 323 (1986) 431.

[9] R. W. Reeve, P. A. Christensen, A. Hamnett, S. A. Haydock,S. C. Roy, J. Electrochem. Soc. 145 (1998) 3463.

[10] R. Parsons,T. VanderNoot, J. Electroanal. Chem. 257 (1988) 9.

[11] T. Iwasita,F. C. Nart, J. Electroanal. Chem. 317 (1991) 291.

[12] P. A. Christensen, A. Hamnett, J. Munk,G. L. Troughton, J. Electroanal. Chem. 370 (1994) 251.

[13] M. Breiter, Electrochim. Acta 12 (1967) 1213.

[14] V.S. Bagotzki, Y.B. Vassileiv,O.A. Kazova, J. Electroanal. Chem. 81 (1977) 229.

[15] T. Iwasita, Electrochim. Acta 47 (2002) 3663-3674.

[16] B. Bittins-Cattaneo, E. Cataneo, P. Königshoven,W. Vielstich, Marcel Dekker, 1991.

[17] T.O. Pavela, Ann. Acad. Sci. Fenn. Ser. K A2 1 (1954)

[18] M.J. Schlachter, Reinhold, New York, 1963.

[19] M. Breiter, Disc. Faraday Soc. 45 (1968) 79.

[20] Y. Ota, M. Nakagawa,Takahashi, J. Electroanal. Chem. 179 179.

[21] O. Wolter,J. Heitbaum, J. Electrochem. Soc. 132 (1985) 1635.

[22] H. Wang, T. Löffler,H. Baltruschat, J. Appl. Electrochem. 31 (2001) 759.

[23] C. Korzeniewski,C. Childers, J. Phys. Chem. B (1998) 489.

[24] A.J. Bard,L. R. Faulkner, Electrochemical Methods, John Wiley & Sons, New York, 1980.

[25] W. Vielstich S. Wasmus ed., Differential Electrochemical Mass Spectrometry: 20 Years of Developement, Electroanalytical Chemistry, 2001.

[26] O. Wolter, C. Giordano, J. Heitbaum,W. Vielstich, in Proceeding Symposium on Electrocatalysis,The electrochemical Soc.,, pennington, 1982, p. 235.

[27] H. Baltruschat, ed., Differential Electrochemical mass spectrometry as a tool for interfacial studies, Interfacial Electrochemistry, Marcel Dekker, New York, 1999.

[28] L. Grambow,S. Bruckenstein, Electrochim. Acta 22 (1977) 377.

[29] R.R. Gadde S.Bruckenstein J. Am. Chem. Soc., 93 (1971) 793.

[30] P.A. Christensen, A. Hamnett,G.L. Troughton, J. Electroanal. Chem. 362 (1993) 207.

[31] T. Frelink, W. Visscher,J.A.R. van Veen, J. Electroanal. Chem. 382 (1995) 65.

[32] M.P. Hogarth, P.A. Christensen,A. Hamnett, in Proceedings of the first international symposium on new materials for fuel cell systems,, Montreal, July 9–13, 1995.

[33] M. Watanabe, M. Uchida,S. Motoo, J. Electroanal. Chem. 229 (1987) 395.

[34] J.B. Goodenough, A. Hamnett, B.J. Kennedy, R. Manoharan,S.A. Weeks, Electrochim. Acta 35 (1990) 199.

[35] R. Pattabiraman, in Proceedings of the first international symposium on new materials for fuel cell systems, Montreal, 1996, p. 362.

[36] J. Lang A. Freund, Th. Lehmann, K.A. Starz,, Catalysis Today 27 (1996) 279.

[37] T.J. Schmidt, M. Noeske, H.A. Gasteiger, R.J. Behm, P. Britz,H. Bönnemann, J. Electrochem. Soc. 145 (1998) 925.

[38] B.D. McNicol,R.T. Short, J. Electroanal. Chem. 81 (1977) 249.

[39] M. Uchida, Y. Aoyama, N. Tanabe, N. Yanagihara, N. Eda,A. Ohta, J. Electrochem. Soc. 142 (1995) 2572.

[40] T. Kodera A. Aramata, M. Masuda,, J. Appl. Electrochem. 18 (1988) 577.

[41] S.C. Roy, P.A. Christensen, A. Hamnett, K.M. Thomas,V. Trapp, J. Electrochem. Soc. 143 (1996) 3073.

[42] A. J. Appleby, J. Power Sources 37 (1992) 223.

[43] A. Hamnett, Catal. Today 38 (1997) 445.

[44] S. Wasmus and A. Kuver, J. Electroanal. Chem., 461 (1999) 14.

[45] B. D. McNicol, D. A. J. Rand,K. R. Williams, J. Power Sources 83 (1999) 15.

[46] X. Ren, T. E. Springer,S. Gottesfeld, J. Electrochem. Soc. 147 (2000) 92.

[47] B. D. McNicol, P. A. Attwood,R. T. Short, J. Chem. Soc., Faraday Trans. 77 (1981) 2017.

[48] Y. Takasu, T. Iwazaki, W. Sugimoto,Y. Murakami, Electrochem. Commun. 2 (2000) 671.

[49] E. R. Savinova, M. Eikerling, O. V. Cherstiouk,U. Stimming, Abstracts of Papers of the American Chemical Society 225 (2003) U666-U666.

[50] F. Maillard, M. Eikerling, O. V. Cherstiouk, S. Schreier, E. Savinova,U. Stimming, Faraday Discussions 125 (2004) 357-377.

[51] F. Maillard, S. Schreier, M. Hanzlik, E. R. Savinova, S. Weinkauf,U. Stimming, Physical Chemistry Chemical Physics 7 (2005) 385-393.

[52] Y. Takasu, H. Itaya, T. Iwazaki, R. Miyoshi, T. Ohnuma, W. Sugimoto,Y. Murakami, Chem. Commun. (2001) 341-342.

[53] A. S. Arico, P. Creti, P. L. Antonucci, J. Cho, H. Kim,V. Antoncci, Electrochim. Acta 43 (1998) 3719.

[54] M. Uchida, Y. Fukuoka, Y. Sugawara, N. Eda,A. Ohta, J. Electrochem. Soc., 143 (1996) 245.

[55] A. Hamnett, Catal. Today 38 (1997) 445.

[56] H.A. Gasteiger, N. Markovic, P.N. Ross,E.J. Cairns, J. Electrochem. Soc. 141 (1994) 1795.

[57] Liu L., Pu G., Viswanathan R., Fan Q.B., Liu R.X.,Smotkin E.S., Electrochim. Acta 43 (1998) 3657-3663.

[58] S. Wasmus,A. Kuver, J. Electroanal. Chem. 461 (1999) 14-31.

[59] M. Uchida, Fukuoka Y., Sugawara Y., Ohara H.,A. Ohta, J. Electrochem. Soc. 145 (1998) 3708.

[60] C. A. Bessel, K. Laubernds, N. M. Rodriguez,R. T. K. Baker, J. Phys. Chem. B 105 (2001) 1115-1118.

[61] Steigerwalt E.S., Deluga G.A., Cliffel D.E.,Lukehart C.M., J. Phys Chem B 105 (2001) 8097-8101.

[62] D.L. Boxall, G.A. Deluga, E.A. Kenik, W.D. King,C.M. Lukehart, Chem Mater 13 (2001) 891-900.

[63] Eve S. Steigerwalt, Gregg A. Deluga,C. M. Lukehart, J. Phys. Chem. B 106 (2002) 760-766.

[64] Cheng Wang, Mahesh Waje, Xin Wang, Jason M. Tang, Robert C. Haddon,Yushan

Yan, Nano Lett. 4 (2004) 345-348.

[65] Zhibin He, Jinhua Chen, Dengyou Liu, Hao Tang, Wei Deng,Yafei Kuang, Materials Chemistry and Physics 85 (2004) 396–401.

[66] Changhai Liang Wenzhen Li , Jieshan Qiu , Weijiang Zhou , Hongmei Han , Zhaobin Wei , Gongquan Sun , Qin Xin, Carbon 40 (2002) 787– 803.

[67] Guangli Che, Brinda B. Lakshmi, Charles R. Martin,Ellen R. Fisher, Langmuir 15 (1999) 750-758.

[68] Taeghwan Hyeon, Sangjin Han, Yung-Eun Sung, Kyung-Won Park,Young-Woon Kim, Angew. Chem. Int. Ed. 42 (2003) 4352 –4356.

[69] Kyung-Won Park, Yung-Eun Sung, Sangjin Han, Youngkwang Yun,Taeghwan Hyeon, J. Phys. Chem. B 108 (2004) 939-944.

[70] Geun Seok Chai, Suk Bon Yoon, Jong-Sung Yu, Jong-Ho Choi,Yung-Eun Sung, J. Phys. Chem. B 108 (2004) 7074-7079.

[71] Sang Hoon Joo, Seong Jae Choi, Ilwhan Oh, Juhyoun Kwak, Zheng Liu, Osamu Terasaki,Ryong Ryoo, Nature 412 (2001) 169-172.

[72] Y. Takasu, T. Kawaguchi, W. Sugimoto,Y. Murakami, Electrochim. Acta 48 (2003) 3861.

[73] Yu. I. Yermakov, V. F. Surovikin, G. V. Plaksin, V. A. Semikolenov, V. A. Likholobov, A. L. Chuvilin,S. V. Bogdanov, React. Kinet. Catal. Lett. 33 (1987) 435.

[74] J. B. Donnet, R. Ch. Bansal,M. J. Wang, Carbon Blacks, Marcel Dekker, New York, 1993.

[75] K.A. Friedrich, K.P. Geyzers, A.J. Dickinson,U. Stimming, J. Electroanal. Chem. 524-525 (2002) 261.

[76] Samuel Guerin, Brian E. Hayden, Christopher E. Lee, Claire Mormiche, John R. Owen,Andrea E. Russell, J. Comb. Chem. 6 (2004) 149-158.

[77] A.A. Kulikovsky, Electrochemistry Communications 5 (2003) 530–538.

[78] V. Gogel, T. Frey, Zhu Yongsheng, K.A. Friedrich, L. Jörissen,J. Garche, J. Power Sources 127 (2004) 172–180.

[79] A. Havranek,K. Wippermann, J. Electroana. Chem. 567 (2004) 305–315.

[80] H. Hitmi, E. M. Belgsir, J. M. Leger, C. Lamy,R. O. Lezna, Electrochim. Acta 39 (1994) 407.

[81] N. Fujiwara, K.A. Friedrich,U. Stimming, J. Electroanal. Chem. 472 (1999) 120–125.

[82] L.W. H. Leung, S.C. Chang,M. J. Weaver, J. Electroanal. Chem. 266 (1989) 317.

[83] D. J. Tarnowski,C. Korzeniewski, J. Phys. Chem. B 101 (1997) 253.

[84] J. Wang, S. Wasmus,R. F. Savinell, J. Electrochem. Soc. 142 (1995) 4218.

[85] A. S. Arico, P. Creti, P. L. Antonucci, J.; Kim Cho,V. Antonucci, Electrochim. Acta 43 (1998) 3719.

[86] G.A. Camara,T. Iwasita, J. Electroanal. Chem. 578 (2005) 315–321.

[87] Wang H, Jusys Z,Behm RJ, J. Phy. Chem. B 108 (2004) 19413-19424.

[88] H. Wang, Z. Jusys,R. J. Behm, J. Power Sources 154 (2006) 351-359.

[89] C. Lamy, E.M. Belgsir,J.M. Léger, J. Appl. Electrochem. 31 (2001) 799.

[90] C. Lamy, A. Lima, V. Le Rhun, F. Delime, C. Coutanceau,J.-M. Léger, J. Power Sources 105 (2002) 283.

[91] C. Lamy, S. Rousseau, E.M. Belgsir, C. Coutanceau,J.-M. Leger, Electrochim. Acta 49 (2004) 3901–3908.

[92] F. Vigier, C. Coutanceau, F. Hahn, E. M. Belgsir,C. Lamy, J. Electroanal. Chem. 563 (2004) 81-89.

[93] F. Vigier, C. Coutanceau, A. Perrard, E. M. Belgsir,C. Lamy, J. Appl. Electrochem. 34 (2004) 439-446.

[94] S. Rousseau, C. Coutanceau, C. Lamy,J. M. Leger, J. Power Sources 158 (2006) 18-24.

[95] C. Coutanceau, L. Demarconnay, C. Lamy,J. M. Leger, Journal of Power Sources 156 (2006) 14-19.

[96] J. R. Varcoe,R. C. T. Slade, Fuel Cells 5 (2005) 187-200.

[97] J. R. Varcoe, R. C. T. Slade,E. L. H. Yee, Chemical Communications (2006) 1428-1429.

[98] J. R. Varcoe,R. C. T. Slade, Electrochemistry Communications 8 (2006) 839-843.

[99] Z. Jusys, J. Kaiser,R.J. Behm, Electrochim. Acta 47 (2002) 3693.

[100] L. Liu, G. Pu, R. Viswanathan, Q.B. Fan, R.X. Liu,E.S. Smotkin, Electrochim. Acta 43 (1998) 3657-3663.

[101] T. Seiler, E.R. Savinova, K.A. Friedrich,U. Stimming, Electrochim. Acta 49 (2004) 3927-3936.

[102] S. F. Baxter, V. S. Battaglia,R. E. White, J. Electrochem. Soc. 146 (1999) 437.

[103] R. H. Perry,D. Green, eds., Perry's Chemical Engineers' Handbook, McGraw-Hill Inc., New York, 1984.

[104] J. Divisek, R. Jung,I. C. Vinke, J. Appl. Electrochem. 29 (1999) 165-170.

[105] J. Divisek, R. Wilkenhöner,Y. Volfkovich, J. Appl. Electrochem. 29 (1999) 153-163.

[106] C. Boyer, S. Gamburzev, O. Velev, S. Srinivasan,A.J. Appleby, Electrochim. Acta 43

(1998) 3703.

[107] Dana Pantea , Hans Darmstadt , Serge Kaliaguine , Lydia Summchen ,Christian Roy, Carbon 39 (2001) 1147–1158.

[108] M.T. Reetz,M.G. Koch, J. Amer. Chem. Soc. 121 (1999) 7933-7934.

[109] A.P. Karnaukhov, V.B. Fenelonov,V.Yu. Gavrilov, Pure Appl. Chem. 61 (1989) 1913.

[110] E.P. Barrett, L.G. Joyner,P.P. Halenda, J. Amer. Chem. Soc. 73 (1951) 373.

[111] A.L.Vishnevskii, V.V.Molchanov, T.A.Kriger,L.M.Plyasova, in Intern. Conf. On Powder Diffraction and Crystal Chemistry St. Petersburg, 1994, p. 206.

[112] Guerrero-Ruiz A., Badenes P.,Rodríguez-Ramos I., Appl. Catal.:A. Gen. 173 (1998) 313-321.

[113] F. Rodríguez-Reinoso, I. Rodríguez-Ramos, C. Moreno-Castilla, A. Guerrero-Ruiz,J. D. López-González, J. Catal. 99 (1986) 171-183.

[114] J. W. Long, R. M. Stroud, K.E. Swider-Lyons,D. R. Rolison, J. Phys. Chem. B 104 (2000) 9772.

[115] D. R. Rolison, P. L. Hagans, K. E. Swider,J. W. Long, Langmuir 15 (1999) 774.

[116] I.G. Batyev,A.N. Karavanov, Surface (Russ. ed.) 12 (1992) 83-87.

[117] J.F. Long, R.M. Stroud, K.E. Swider-Lyons,D.R. Rolison, J. Phys. Chem. B 104 (2000) 9772-9776.

[118] E. Antolini, L. Giorgi, A. Pozio,E. Passalacqua, J. Power Sources 77 (1999) 136.

[119] G. Sasikumar, J. W. Ihm,H. Ryu, J. Power Sources 132 (2004) 11–17.

[120] A.S. Arico, A.K. Shukla, K.M. El-Khatib, P. Creti,V. Antonucci, Journal of Applied Electrochemistry 29 (1999) 671-676.

[121] Huyen N. Dinh, Xiaoming Ren, Fernando H. Garzon, Piotr Zelenay,Shimshon Gottesfeld, J. Electroanal. Chem. 491 (2000) 222–233.

[122] Z. Jusys, Schmidt T.J., Dubau L., Lasch K., Jorissen L., Garche J.,Behm R.J., J. Power Sources 105 (2002) 297-304.

[123] P.A. Simonov,V. A. Likholobov, in Catalyis and Electrocatalysis at Nanoparticle surfaces (E. R. Savinova A. Wiechowski, C. G. Vayenas, ed.), Marcel Dekker, New York, 2003, p. 409.

[124] K.A. Friedrich, K.P. Geyzers, A.J. Dickinson,U. Stimming, J. Electroanal. Chem. 524–525 (2002) 261–272.

[125] Remo Ianniello, Volkmar M. Schmidt, Jose´ Luis Rodrý´guez,Elena Pastor, J. Electroanal. Chem. 471 (1999) 167–179.

[126] J. T. Wang, S. Wasmus,R. F. Savinell, J. Electrochem. Soc. 142 (1995) 4218-4224.

[127] S. Wasmus, J. T. Wang,R. F. Savinell, J. Electrochem. Soc. 142 (1995) 3825-3833.

[128] H. Wang, T. Loffler,H. Baltruschat, J. Appl. Electrochem. 31 (2001) 759-765.

[129] R.B. deLima, V. Paganin, T. Iwasita,W. Vielstich, Electrochim. Acta 49 (2003) 85–91.

Publications

Part of this research work has been published:

1. V. Rao, P.A. Simonov, E.R. Savinova, G.V. Plaksin, S.V. Cherepanova, G.N. Kryukova, U. Stimming, "The influence of carbon support porosity on the activity of PtRu/Sibunit anode catalysts for methanol oxidation" *J. Power Sources* 145 (2005) 178.
2. V. Rao, C. Cremers, U. Stimming "Electro oxidation of ethanol at gas diffusion electrodes: a DEMS study" *Journal of The Electrochemical Society,* 154 **(**2007) 11.
3. V. Rao, Hariyanto, C. Cremers, U. Stimming "DEMS on ethanol oxidation in alkaline membrane electrode assembly" *Fuel cells,* 5 (2007) 417.
4. V. Rao, W. Seliger, C. Cremers, U. Stimming, "Potential distribution across the anode catalyst layer of a DMFC". To be submitted.

Acknowledgement

I would like to specially thank Professor Dr. Ulrich Stimming for providing the opportunity to perform this research work and for supervision of this thesis. Likewise I would like to thank Dr. Carsten Cremers and Dr. Elena Savinova for their encouraging discussions during the experiments. Last but not the least I would like to thank my colleagues at E19, Physik Department, T.U. München, who supported me in all possible ways in carrying out my research work at E19.